Studies on Some Image Processing and Deep Learning Algorithms for Computer-Aided Diagnosis System in Detection, Characterization, and Subtype Classification of Lung Cancer

Thesis Submitted by

Amitava Halder

Doctor of Philosophy (Engineering)

Electrical Engineering Department,
Faculty Council of Engineering & Technology
Jadavpur University
Kolkata, India
2023

JADAVPUR UNIVERSITY
KOLKATA-700032, INDIA

INDEX NO. 103/17/E

1. Title of the thesis:

Studies on Some Image Processing and Deep Learning Algorithms for Computer-Aided Diagnosis System in Detection, Characterization, and Subtype Classification of Lung Cancer

2. Name, Designation and Institution of the Supervisor:

Dr. Debangshu Dey
Associate Professor
Department of Electrical Engineering
Jadavpur University
Kolkata 700032, India

3. List of Publications:

i. Journals:

- **Amitava Halder**, Debangshu Dey and Anup Kumar Sadhu, "Lung Nodule Detection from Feature Engineering to Deep Learning in Thoracic CT Images: a Comprehensive Review," in ***Journal of Digital Imaging, Springer,*** **(Impact Factor: 5.40)**, vol. 33, no. 3, pp. 655-677, Jan. 2020, doi: 10.1007/s10278-020-00320-6.

- **Amitava Halder**, Saptarshi Chatterjee, Debangshu Dey, Surajit Kole and Sugata Munshi, "An Adaptive Morphology Based Segmentation Technique for Lung Nodule Detection in Thoracic CT Image," in ***Computer Methods and Programs in Biomedicine, Elsevier,*** **(Impact Factor: 6.10)**, vol. 197, 105720, Aug. 2020, doi:10.1016/j.cmpb.2020. 105720.

- **Amitava Halder**, Saptarshi Chatterjee and Debangshu Dey, "Adaptive Morphology Aided 2-Pathway Convolutional Neural Network for Lung Nodule Classification," in ***Biomedical Signal Processing and Control, Elsevier,*** **(Impact Factor: 5.10)**, vol. 72, 103347, Nov. 2021, doi: 10.1016/j.bspc.2021.103347.

- **Amitava Halder** and Debangshu Dey, "Atrous Convolution Aided Integrated Framework for Lung Nodule Segmentation and Classification," in ***Biomedical Signal Processing and Control, Elsevier,*** **(Impact Factor: 5.10)**, vol. 82, 104527, Dec. 2022, doi: 10.1016/j.bspc.2022.104527.

- **Amitava Halder** and Debangshu Dey,"MorphAttnnet: An Attention -based Morphology Framework for Lung Cancer Subtype Classification," in ***Biomedical Signal Processing and Control, Elsevier,*** **(Impact Factor: 5.10)**, vol. 86, 105149, June 2023, doi: 10.1016/j.bspc.2023.105149.

ii. **<u>Book Chapter:</u>** Nil.

4. List of Patents: Nil.

5. List of Presentations in International Conferences:

- **Amitava Halder**, Saptarshi Chatterjee and Debangshu Dey, “Superpixel and Density Based Region Segmentation Algorithm for Lung Nodule Detection”, in ***Proc. of 2020 IEEE Calcutta Conference (CALCON),*** Kolkata, 2020, pp. 511-515, doi: 10.1109/CALCON49167.2020.9106569.

- **Amitava Halder**, Saptarshi Chatterjee and Debangshu Dey, “Morphological Filter Aided GMM Technique for Lung Nodule Detection”, in ***Proc. of 2020 IEEE Applied Signal Processing Conference (ASPCON),*** Kolkata, 2020, pp. 198-202, doi: 10.1109/ASPCON49795.2020.9276715.

Statement of Originality

I, **Amitava Halder**, registered on 21/02/2017 do hereby declare that this thesis entitled "***Studies on Some Image Processing and Deep Learning Algorithms for Computer-Aided Diagnosis System in Detection, Characterization, and Subtype Classification of Lung Cancer*** " contains literature survey and original research work done by the undersigned candidate as part of Doctoral studies.

All information in this thesis have been obtained and presented in accordance with existing academic rules and ethical conduct. I declare that, as required by these rules and conduct, I have fully cited and referred all materials and results that are not original to this work.

I also declare that I have checked this thesis as per the "Policy on Anti Plagiarism, Jadavpur University, 2019", and the level of similarity as checked by iThenticate software is ...4... %.

Signature of Candidate: Amitava Halder.

Date: 20.07.2023.

Certified by Supervisor:
(Signature with date and seal)

20.07.2023

Dr. Debangshu Dey
Associate Professor
Electrical Engineering Department
Jadavpur University
Kolkata-700 032

Certificate from the Supervisor

This is to certify that the thesis entitled "***Studies on Some Image Processing and Deep Learning Algorithms for Computer-Aided Diagnosis System in Detection, Characterization, and Subtype Classification of Lung Cancer***" submitted by Sri **Amitava Halder**, who got his name registered on 21/02/2017 for the award of Ph.D. (Engg.) degree of Jadavpur University is absolutely based upon his own work under the supervision of Dr. Debangshu Dey and that neither his thesis nor any part of the thesis has been submitted for any degree/diploma or any other academic award anywhere before.

20.07.2023

(Dr. Debangshu Dey)

Signature of the Supervisor
and date with Official Seal

Dr. Debangshu Dey
Associate Professor
Electrical Engineering Department
Jadavpur University
Kolkata-700 032

Acknowledgement

The author would like to express his gratitude and sincere appreciation to everyone who has given of their time and encouraged me throughout the course of my Ph.D. tenure. Throughout this time, I am appreciative of their precious suggestions, invaluable constructive criticism, and cordial counsel. They provided me with honest and enlightening opinions on a variety of topics pertaining to my doctoral research, for which I genuinely thank them. The author would like to express sincere gratitude to his supervisor *Dr. Debangshu Dey*, Associate Professor, Electrical Engineering Department, Jadavpur University, for his unwavering support of Ph.D. research and study. The author feels fortunate to have had such a mentor who gave him the freedom to pursue his interests while still providing guidance when his steps faltered. His advice has been helpful throughout the entire research and writing process for this dissertation. The author is also appreciative of him for morally supporting him while he was in trouble.

The author wishes to convey his profound gratitude to Prof. Sugata Munshi at the Electrical Engineering Department of Jadavpur University for his invaluable counsel and continued assistance in conducting the research.

The author gives credit to Dr. Abhijit Lahiri, Principal of MCKV Institute of Engineering, Howrah, India, for inspiring him to continue his research. His unwavering support in both his personal and academic life is priceless.

The author is grateful to the present and former Heads of the Electrical Engineering Department at Jadavpur University for providing adequate research facilities in the department. The author also thanks the faculty and staff members of the department of electrical engineering for their unwavering support and encouragement.

The author thanks Mr. Surojit Kole, consultant radiologist, Theism Ultrasound Centre, Dum Dum, Kolkata, India, for his insightful comments and important contribution to this research work. The author would always be grateful to him for giving sufficient time from his busy schedule and contributing his medical knowledge to the research project.

This research project would not have been possible to finish without the constant assistance from fellow researchers of the Measurements and Instrumentation Laboratory, Department of Electrical Engineering. In this regard, author would like to thank his laboratory members Dr. Biswarup Ganguly, Ms. Sayanti Chaudhuri, Dr. Pritam Paral, Dr. Saptarshi Chatterjee, Ms. Antara Ghosh, Mr. Saibal Ghosh, Mr. Anadi Biswas, Ms. Rashmi Rekha Sahoo, and Ms. Pubali De for their continuous emotional support to overcome the hardships during Ph.D. journey.

The author would like to specifically thank his wife, Mrs. Tumpa Halder Bagui, for all of her love and support throughout this Ph.D. journey. The author also expresses his sincere gratitude to his wife for giving him the drive and good attitude he needed to advance to this point in his doctoral studies.

The author concludes by expressing his gratitude to his parents for their sacrifice, love, belief, and unwavering support and encouragement during the entire journey. This work would not have been possible without his parents' tireless efforts, encouragement, and blessings.

Amitava Halder
Measurements & Instrumentation Laboratory
Department of Electrical Engineering
Jadavpur University
Kolkata, India
July 2023

“Arise, awake, and stop not till the goal is reached”

Swami Vivekananda

Dedicated to …

My Parents
My Wife Tumpa
&
My Son Ankit

List of Symbols

Symbol	**Description**
AS_{Im}	Automatically segmented image
b_k	Bias value at k^{th} layer of ANN
bg^k	Mean gray level value of the background object at k^{th} step
D_{Adpt_w}	Adaptive dilation operation using learnable weight matrix
D_w	Dilation operation using learnable weight matrix
E_{Adpt_w}	Adaptive erosion operation using learnable weight matrix
$E_{i,n}$	The n^{th} component of i^{th} feature vector
E_w	Erosion operation using learnable weight matrix
F	Feature Map
fg^k	Mean gray level value of the foreground object at k^{th} step
f_i	Feature map obtained from i^{th} layer of network
FN	False Negative
FP	False Positive
$f(x, y)$	Output image pixel
g_f	Output obtained by applying global average pooling operation on the input feature map
GT_{Im}	Ground truth image
I_{bgimg}	Background estimated image
I_{bgrad}	Binary gradient image
I_{brdr}	Border image
I_{brimg}	Background reduced image
I_{btop_hat}	Black top-hat image
I_{fill}	Region filled image
I_{grad}	Gradient image
I_l	Label image
I_{lung}	Lung segmented image

I_{lungm}	Lung mask
I_m	Grayscale lung CT image
I_{marker}	Marker image
I_{mask}	Mask image
I_o	Opening image
I_{pre}	Pre-processed image
I_{recst}	Reconstructed image
I_{seg}	Segmented image
I_{simg}	Subtrahend image
I_{wt}	White top-hat image
L_{bce}	Binary cross entropy loss function
L_{loss}	Loss function
L_m	Layer obtained by concatenation operation
O_{Adpt_w}	Adaptive opening operation using learnable weight matrix
O_{GAP_i}	Scalar output of GAP operation for i^{th} feature map
O_{GMP_i}	Scalar output of GMP operation for i^{th} feature map
$p(x, y)$	Input image pixel
S	Structuring element
S^*	Transposed structuring element
S_f	Learned scale factor for the f_{th} channel
S_L	Layers of CNN
$softmax(.)$	Softmax activation function
T^k	Threshold value obtained at step k
TN	True Negative
TP	True Positive
$\boldsymbol{W}$	Learned weight matrices
$\boldsymbol{W}_1$	Learned weight matrices for 1st hidden layer
$\boldsymbol{W}_2$	Learned weight matrices for 2nd (output) layer
W_ε	Trainable weight matrix for erosion operation

W_{Adpt_ε}	Trainable adaptive weight matrix for erosion operation
W_{δ}	Trainable weight matrix for dilation operation
W_{Adpt_δ}	Trainable adaptive weight matrix for dilation operation
W_{qr}	Weight connected from neuron *q* of *(k*-1*)*-th layer to neuron *r* of *k*-th layer of ANN
X	Input feature map
$\underset{x}{\rightarrow}$	Flattened vector form of feature map
Y_f	Output of the attention block
Z	Output feature map
z_i	Output of i^{th} neuron in the output layer of the NN
α	Learning rate
ε_S	Grayscale Erosion Operation
δ_s	Grayscale Dilation Operation
α_s	Grayscale Opening Operation
β_s	Grayscale Closing Operation
ε_{Adpt}	Grayscale Adaptive Erosion Operation
δ_{Adpt}	Grayscale Adaptive Dilation Operation
α_{Adpt}	Grayscale Adaptive Opening Operation
β_{Adpt}	Grayscale Adaptive Closing Operation
γ_{Adpt}	Grayscale Adaptive Bottom-Hat Operation
$\xi(Q)$	Image intensity value for a point Q
η	Learning rate of the network
σ_x	Standard deviation in x direction
σ_y	Standard deviation in y direction
G_σ	Gaussian Kernel
$G(x, y)$	Two-dimensional Gabor function
∇	First order derivative
∇T	Permitted threshold difference
$\wedge$	Momentum value of the network

r_w	Filter bandwidth radius
$\lambda_1(Q)$	First eigen value for point *Q*
$\lambda_2(Q)$	Second eigen value for point *Q*
$\boldsymbol{e}_1(Q)$	First eigen vector for point *Q*
$\boldsymbol{e}_2(Q)$	Second eigen vector for point *Q*
$a(Q)$	Semi-major axis *a* of the ellipse w.r.to point *Q*
$b(Q)$	Semi-minor axis *b* of the ellipse w.r.to point *Q*
$\psi(Q)$	Orientation of the ellipse w.r.to point *Q*

List of Abbreviations

Abbreviation	Description
2-D	Two-dimensional
3-D	Three-dimensional
2PMorphCNN	2-Pathway Morphology-based Convolutional Neural Network
ABHT	Adaptive Bottom-Hat
Acc	Accuracy
ACS	American Cancer Society
Adam	Adaptive Moment Estimation
ADC	Adenocarcinoma
AEs	Auto-Encoders
AESEs	Adaptive Elliptical Structuring Elements
AGAN	Aggregation-U-net GAN
AHSN	Angular Histogram of Surface Normal
AI	Artificial Intelligence
AMST	Adaptive Morphology-Based Segmentation Technique
AND	Logical ‘AND’ Operation
ANN	Artificial Neural Network
ASE	Adaptive Structuring Element
ASEs	Adaptive Structuring Elements
ASPP	Atrous Spatial Pyramid Pooling
ATCNN	Atrous Convolution-based Convolutional Neural Network
AUC	Area Under the ROC Curve
BCE	Binary Cross Entropy
BF	Boundary F1
BP	Backpropagation
BPNN	Back Propagation Neural Network
CAD	Computer Aided Detection and Diagnosis

CADe	Computer-Aided Detection
CADx	Computer-Aided Diagnosis
CE	Cross-Entropy
CF-CNN	Central Focused Convolutional Neural Network
CLBP	Completed Local Binary Patterns
CMR	Cardiac Magnetic Resonance
CNEF	Cylindrical Nodule- Enhancement Filter
CNN	Convolutional Neural Network
CNNs	Convolutional Neural Networks
CRF	Conditional Random Field
CT	Computed Tomography
DA	Detection Accuracy
DICOM	Digital Imaging and Communication in Medicine
DL	Deep Learning
DNG	Divergence of Normalized Gradient
DPNs	Dual Path Networks
DSC	Dice Similarity Coefficient
DTCNN	Deep Transfer Convolutional Neural Network
ELM	Extreme Learning Machine
FC	Fully Connected
FCM	Fuzzy c-means
FCN	Fully Convolutional Network
FOV	Field Of View
FN	False Negative
FP	False Positive
FPs	False Positives
FV	Fisher Vector
GA	Genetic Algorithm
GAN	Generative Adversarial Network
GAP	Global Average Pooling

GATM	Genetic Algorithm Template Matching
GBM	Gradient Boosting Machine
GF	Gabor Filter
GGMM	Gamma-Gaussian Mixture Model
GGO	Ground Glass Opacity
GGOs	Ground Glass Opacities
GLCM	Gray-Level Co-Occurrence Matrix
GLOBOCAN	Global Cancer Observatory
GMM	Gaussian Mixture Model
GMP	Global Maximum Pooling
GNG	Growing Neural Gas
GPUs	Graphics Processing Units
GT	Ground Truth
HRCT	High Resolution Computed Tomography
IARC	International Agency for Research on Cancer
ILD	Interstitial Lung Disease
IT2MFs	Interval Type-2 Membership Functions
JI	Jaccard Index
KBC	knowledge-Based Collaborative
LCLC	Large Cell Lung Carcinoma
LDCT	Low-Dose Computed Tomography
LIDC-IDRI	Lung Image Database Consortium-Image Database Resource Initiative
LoG	Laplacian-of-Gaussian
LUNA16	LUng Nodule Analysis 2016
LV	Left Ventricle
MC-CNN	Multi-Crop Convolutional Neural Network
MDCT	Multi-Detector Computed Tomography
ML	Machine Learning
MLA	Multi-Level Learning Architecture

MorphAttnNet	Morphology-based Attention Network
MSM	Mass–Spring Model
NLST	National Lung Screening Trial
NN	Neural Network
NSCLC	Non Small Cell Lung Cancer
OALO	Oppositional based 'Ant Lion Optimization'
OR	Logical ‘OR’ Operation
PBC	Patch-Based Classifier
PCA	Principal Component Analysis
PSO	Particle Swarm Optimization
QT	Quality Threshold
RBF	Radial Basis Function
ReLU	Rectified Linear Unit
RF	Rotation Forest
ROI	Region of Interest
ROIs	Region of Interests
RReLU	Randomized Leaky Rectified Linear Unit
SA	Segmentation Accuracy
SAEs	Stacked Auto-Encoders
SCC	Squamous Cell Carcinoma
SCLC	Small Cell Lung Cancer
SE	Structuring Element
Sen	Sensitivity
SEs	Structuring Elements
SIFT	Scale-Invariant Feature Transform
SLIC	Simple Linear Iterative Clustering
SP	Superpixel
SPDBR	Superpixel and Density Based Region
Spec	Specificity
SPN	Solitary Pulmonary Nodule

SPs	Superpixels
SVM	Support Vector Machine
TN	True Negative
TP	True Positive
TS	Training Dataset
VGG	Visual Geometry Group
VRR	Voxel Removal Rate
WHO	World Health Organization
WSI	Whole Slide Imaging

Abstract

In recent years, there is a huge scope for research in the domain of automatic disease detection, characterization, and classification using image processing and pattern recognition techniques. This is a result of the rise in various diseases around the world. Cancer is a disease that has several manifestations and it is primarily associated with abnormal cell groups. These cancer cells continue to divide and grow to produce tumors. Among all types of cancer, lung cancer is the most life- threatening disease all over the world. Appropriate detection and characterization of lung nodules using High Resolution Computed Tomography (HRCT) images helps in early-stage recognition of lung cancer. However, due to structural similarity and smaller size, manual detection and characterization of lung nodules is a time-consuming and error-prone process. Doctors and radiological specialists must physically inspect, analyze, and make subsequent decisions based only on a visual assessment of each slice to find nodules. This process is subjective and significantly depends on the radiologists' experience. Additionally, it might be challenging for a novice radiologist to distinguish between benign and malignant nodules based solely on visual examination. In recent years, different Computer-Aided Detection and Diagnosis (CAD) systems based on machine learning and deep learning have been developed for accurate, reliable, and early-stage lung cancer diagnosis to solve the aforementioned challenges. Therefore, by considering the present scenario, it is essential to develop an automated/semi-automated system that can act as a second opinion and aid in the quicker and more accurate detection, characterization, and classification of lung cancer by radiologists, pathologists, and medical professionals.

In a nutshell, this thesis aims to design and develop some image processing, machine learning, and deep learning algorithms for automatic detection, characterization, and subtype classification of lung cancer from HRCT and Histopathology images. In this regard, different machine learning and recent most deep learning frameworks have been invented and developed to build more sophisticated integrated CAD systems that can outperform existing state-of-the-art frameworks.

Table of Contents

List of Figures

List of Tables

List of Algorithms

Chapter 1

Introduction

1.1 Background

Cancer is a disease that has several manifestations and it is primarily associated to abnormal cell groups. These cancer cells continue to divide and grow to produce tumors. Among all types of cancer, lung cancer is most life-threatening disease all over the world. According to the World Health Organization (WHO) [1], lung cancer is the leading cause of death worldwide. In 2008, 1.37 million deaths caused by lung cancer occurred throughout the world [2]. Available data shows that the lung cancer is the largest among new cancer diagnoses worldwide (1,350,000 new cases and 12.4% of total new cancer cases) and it is the largest cause of death from cancer globally (1,180,000 deaths and 17.6% of total cancer deaths) [3]. It is the most common cancer in men worldwide (1.1 million cases, 16.5% of the total). Among females, it was the fourth (516 000 cases, 8.5% of all cancers) most commonly diagnosed cancer and the second (427000 deaths, 12.8% of the total) leading cause of cancer death [4]. Last five years (2019-2023) estimated new lung cancer cases and total estimated lung cancer deaths found in the United States [5] have been portrayed in Figure 1.1 (a) and (b) respectively.

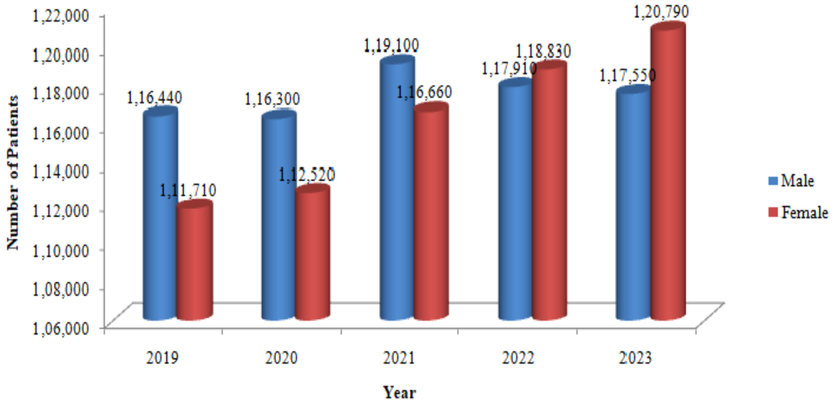

(a)

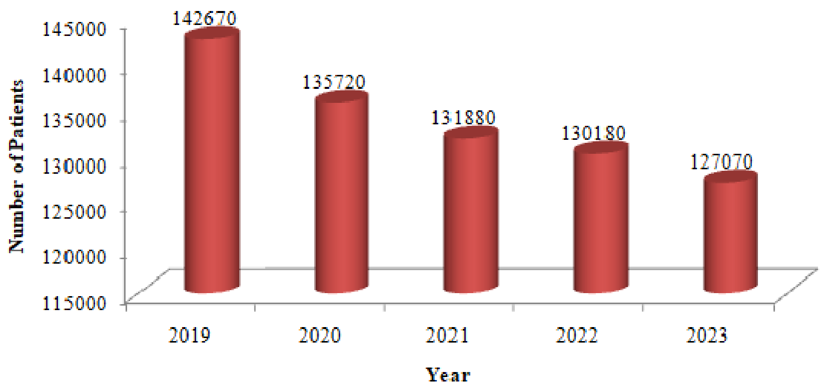

(b)

Figure 1.1: Last five years (2019-2023) lung cancer statistics in US: (a) nos. of estimated new cases, (b) total nos. of estimated deaths. Source: American Cancer Society (ACS) [5].

A report by National Cancer Centre Singapore [6] have shown that 1.2 million people were diagnosed with cancer and 7700 people died of cancer on average in the year 2015 and 158080 cases were expected by the end of 2016. In Brazil, an average of 28220 cases found in 2016 with 17330 males and 10890 females [7].

1.1.1 Automatic Disease Detection and Classification Systems

With today's growing requirements in disease diagnosis, doctors and medical teams are constantly looking for better and accurate solutions for proper treatment. Therefore, to meet the current demands, a disease detection system should be design and develop with state-of-the-art technologies. In recent years, Computer-Aided Detection and Diagnosis (CAD)-based systems are developing to assist the doctors for early disease detection. Different Artificial Intelligence (AI) and Machine Learning (ML) based techniques are in use for accurate design of the CAD-based systems. The input to the CAD frameworks is different medical images. The images are used to analyse by system for the presence of a particular disease and to categorize it into different subclasses. Thus the CAD systems take a series of medical images containing the Region of Interests (ROIs) and outputting the predicted class label accurately. The decision output by the system is then used by the radiologists, pathologist, and doctors to make their final decision. Therefore, disease detection system plays a vital role for early recognition of diseases and acts as a second opinion for the medical team. Presently, different diseases such as heart, lung, diabetes, liver disease etc. have been identified with the help of CAD system. The processing modules of the CAD framework are designed and developed using different machine learning and recent most Deep Learning (DL) algorithms. Lung cancer is one of the most life-threatening cancers mostly indicated by the presence of nodules in the lung. Doctors and radiological experts use High-Resolution Computed Tomography (HRCT) images for nodule detection and further decision making from visual inspection.

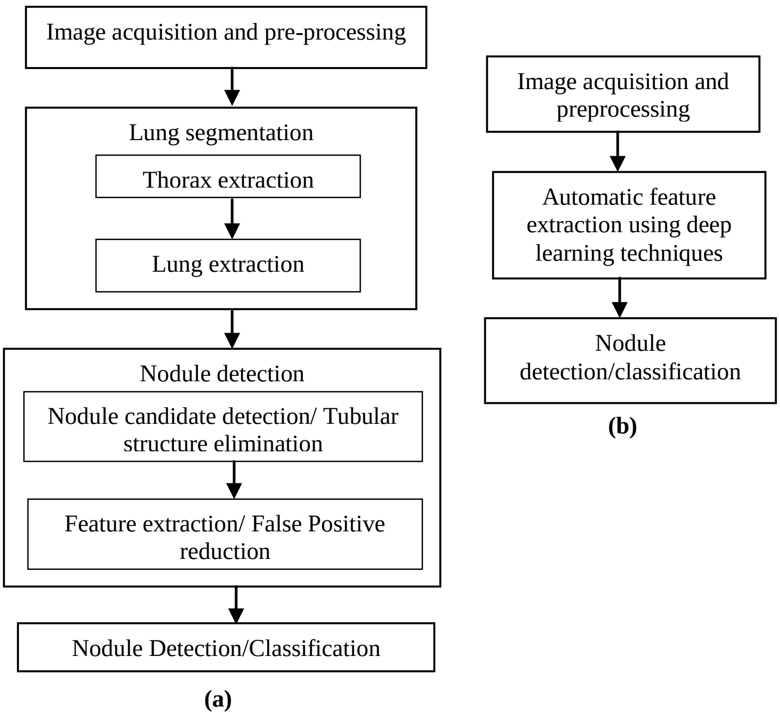

Figure 1.2: Nodule detection framework using (a) machine learning, and (b) deep learning approach.

Manual detection of lung nodules is a time-consuming and error-prone process. Radiologists must examine and analyze each slice for accurate nodule characterization and it is also subjective and heavily relies on the experience of the radiologists. It is also sometimes difficult for the inexperienced radiologist to characterize a nodule as benign and malignant from a visual inspection only. Therefore, to overcome the above-mentioned difficulties Computer-aided detection (CADe) and Computer-aided diagnosis (CADx)-based systems have been continually developing using machine learning and deep learning techniques. The developed CAD-based systems by the researchers assist radiologists, pathologists, and doctors to detect, characterizing, and classifying lung cancer with greater confidence in a lesser amount of time. Thus CAD-based frameworks can serve as a second opinion and have significant impact on the precise, consistent, and early-stage diagnosis of lung cancer. Different automated nodule detection and characterization schemes using machine learning and deep learning techniques have been introduced so far in the existing literature. Figure 1.2 (a) and (b) shows the typical block diagrams of the nodule detection framework using machine learning and deep learning approaches.

1.1.2 Lung Cancer

Lung cancer is characterized by uncontrolled growth of lung cell tissues and become most frequently diagnosed cancer all over the world. Histopathologically, Lung cancer can be divided into two broad categories, viz., 1) Small cell lung cancer (SCLC) and 2) Non–small cell lung cancer (NSCLC). SCLC accounts for 10% to 15% of lung cancer cases and highly malignant, whereas 80% to 85% lung cancers belong to the Non–small cell lung cancer (NSCLC) category [5]. The adenocarcinoma (ADC), squamous cell carcinoma (SCC), and large cell lung carcinoma (LCLC) are the subtypes exist for NSCLC.

1.1.3 Lung Nodule and Lung Mass Definition

A pulmonary nodule refers to the lung tissue abnormality mostly found in lung cancer patients. In 1984, a glossary of terms published by Fleischner Society [8] for thoracic radiology. The society has defined lung nodule as "*any pulmonary or pleural lesion represented in a radiograph by a sharply defined, discrete, nearly circular opacity 2–30 mm in diameter*". Twelve years later, the society defined lung nodule as "*round opacity, at least moderately well marginated and no greater than 3 cm in maximum* *diameter*". The solitary pulmonary nodule (SPN) is defined as a radiographic opacity with a diameter of up to 30 mm and at least two-thirds of its margins surrounded by lung parenchyma. On the other hand, if the diameter is greater than 30mm, it is called Lung Mass. Lung masses are generally cancerous.

1.1.4 Structural Properties of Lung Nodule

According to the location the solitary pulmonary nodules can be categorized as a)Well-circumscribed: The nodule is located centrally in the lung without significant connections to vasculature, b)Vascularized: The nodule is located centrally in the lung, but has significant vascularisation (connections to neighbouring vessels), c) Juxtapleural: A significant proportion of the nodule periphery is connected to the pleural surface and d)Pleural tail: The nodule is near the pleural surface, connected by a thin structure called *"pleural tail"* [9]. A complete guideline for small pulmonary nodule management including its growth information is provided by the work of MacMahon *et al*. [10]. Recent guidelines and management of pulmonary nodules are described in [11]. A deep and extensive study of patients with previous cancer history was presented by the work of Rena *et al*. [12] for SPN characterization. The morphological appearances such as border, shape and location characteristics of a lung nodule in Computed Tomography (CT) image are described in [13-14]. Figure1.3 shows four types of SPNs. The information about Ground Glass Opacity (GGO) nodule is available in [15]. Different types of Ground Glass Opacities (GGOs) are shown in Figure1.4.

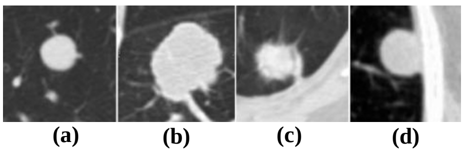

Figure 1.3: Typical SPNs for different type (a) Well-circumscribed nodule, (b) Juxta-vascular nodule, (c) Nodule with a pleural tail, (d) Juxta-pleural nodule Dhara *et al*. [16].

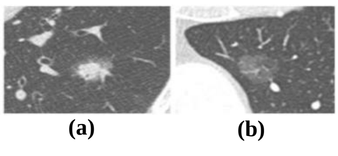

Figure 1.4: Examples of (a) Sub-solid, and (b) Pure ground-glass nodules Lederlin *et al*. [17].

1.2 An Overview of HRCT and Histopathology Images for Lung Cancer Diagnosis

High Resolution Computed tomography is a non-invasive imaging procedure that uses x-ray to create detailed cross-sectional images or slices of different areas inside the body. CT technology has been introduced in 1973. The basic parts of a CT scanner comprises of 1) moving X-ray tube and detectors, 2) a patient table for conduction of scan and 3) a computer with a viewing console. The x-ray tube focuses a precise beam of energy on a section of the body. A digital computer then analyse the x-ray readings taken at thousands of different points and transform them into CT slices. Due to the widespread availability of multi-detector computed tomography (MDCT), the new generation CT scanners can acquire near-isotropic data in a single breath-hold. HRCT scanner uses different technical parameters, configuration, and protocol e.g., Radiation exposure factors (mAs, kVp), Collimation, Window settings, Display section thickness and image reconstruction interval, Axial or helical acquisition mode, Optimal HRCT Protocol etc. Unlike chest x-ray which taking 1 or 2 pictures; CT devices produce series of x-rays that are combined to form a single scan. Today’s modern CT scanner take continuous pictures in a helical (or spiral) fashion rather than taking a series of pictures and able to construct more detail view of pathology under observation. Figure 1.5 shows a typical CT machine used for diagnosis purpose.

Figure 1.5: Modern CT scanner located at the Lochotín University Hospital in Pilsen, Czech Republic [18].

Medical imaging techniques to examine the presence of lung tumor include chest x-ray and HRCT scans. Among them HRCT scan is preferred and highly recommended for lung nodule detection. As per a report of the National Lung Screening Trial (NLST) [19], a 20% reduction in lung cancer mortality is possible with low-dose computed tomography (LDCT) image as compared to chest X-ray. Therefore, CT scan has become the standard routine imaging tool for non-invasive lung cancer detection. It is used to analyse the internal structure, shape, and size of the lung nodule and determine whether it is solid, part solid or GGO nodule. After detection of lung nodule in HRCT scan, if it shows malignancy characteristics e.g., large size, rough surface etc., then doctors may recommend for a biopsy. The process involves removing a small amount of tissue from the nodule. Then the tissue samples are analysed under a microscope for histological analysis of tumor tissue. The Whole-slide Imaging (WSI) technique is used for this purpose.WSI scanner is used to produce the digital photomicrograph of the lung nodule. The images produced by the WSI scanner is called histopathological image. The histopathological images are colour image and are used for early diagnosis of lung cancer, analyzing tissue growth patterns, and cell morphology for better treatment planning Figure 1.6 (a), (b), and (c) show the typical marked HRCT image for lung nodule and histopathological images of Adenocarcinoma (ADC) and Squamous Cell Carcinoma (SCC) respectively.

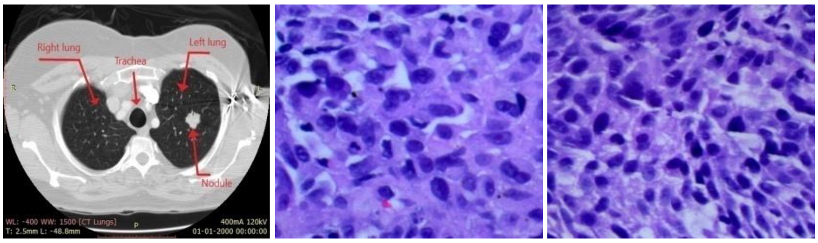

(a) **(b)** **(c)**

Figure 1.6: HRCT and Histopathological images of lung nodule: (a) original lung HRCT image marked by the radiologist (red arrow). Source: LIDC-IDRI [20], (b) Adenocarcinoma, and (c) Squamous Cell Carcinoma Source: LC25000 [21].

1.3 Computer-Aided Lung Cancer Detection and Characterization System

The main objective of the thesis is to design and develop automated computer aided lung nodule detection and characterization system using recent most ML and DL approaches. Reviews of the pulmonary detection techniques are not new but as the computational techniques change from time to time; a thorough review is necessary to understand the technology shipment towards automated nodule detection systems. Different review works with objectives to find out the technological changes exist in literature [16, 22-24]. However, owing to the developments of new techniques, it has been noticed that a recently deep learning-based approach has introduced for nodule detection. Therefore, to cope up with the technological changes, in this chapter, a detailed survey work has been conducted by focusing on the *"nodule detection"* and *"nodule characterization"* process from CT images [25].

1.3.1 Lung Cancer: A Feature Engineering Approach

In this section different existing works using machine learning have been described in details. These traditional ML-based frameworks consist of four main steps, 1) Pre-processing 2) Lung Segmentation 3) Nodule detection and finally 4) Classification. Different approaches have been found in literature for lung nodule detection process that has been described below precisely.

- Threshold-based methods:

This approach is the simplest one among different image segmentation approaches. Image histogram is used to partition the image. Each peak of the histogram represents a particular region and the intensity value between two peaks called the *"threshold"* is selected to separate desired classes. Next, the segmentation process is done by grouping all pixel intensities w.r.to. threshold value. Sousa *et al*.[26] segmented internal structures of the lung by choosing appropriate threshold values. After that, tubular structures were eliminated by applying the 3-D skeletonization algorithm. In their work, researchers have observed that tubular structure, e.g., vessel shows a low variation of the average depth w.r.to medial axis. On the other hand, nodules show an abrupt increase of values from the nodule border. Therefore, by choosing appropriate threshold value with skeletonized segmentation algorithm nodules have been separated from vessels. Messay *et al*. [27] used intensity threshold and morphological processing techniques for nodule candidate detection. Choi and Choi [28] have identified initial nodule candidates by using thresholding and shape information (Area). Aresta *et al*. [29] developed a nodule detection framework using Otsu's threshold method. Different solid, sub-solid, non-solid and juxta-pleural nodules have been detected by their proposed system. Solid nodules were searched slice-wise inside a fixed-width sliding window with stride 1. Next, the Otsu threshold method has been applied inside each window for candidate generation. Finally all windows were combined using logical OR operation. The sub-solid and non-solid nodule candidates were detected using a Laplacian-of-Gaussian (LoG) filter combined with Otsu's method. Mehre *et al*. [30] combined intensity threshold with Structuring Elements (SEs) for candidate nodule detection. Morphological opening operation was performed by using six different intensity values combined with radii of SEs, viz., (-400, 2), (-500, 2), (-600, 2), (-400, 3), (-500, 3), (-600, 3) for nodule detection. It is observed that the detection sensitivity varies from 82.66% with an average 3FPs/scan/case [27] to 94.1% at 5.54 FPs/scan [31] by using threshold-based approach. The juxta-pleural nodule candidates were also detected with a sensitivity of 57.4% at 4FPs/scan by using this approach [29].The thresholding approach is entirely based on pixel intensity of an image. It highly depends on the histogram peaks of an image. Finding an appropriate threshold is a challenging task; as pixel intensity is more sensitive to noise and intensity inhomogeneities. Apart from these, spatial characteristics of an image is not taken into account by this approach and not good for images with wide plane valleys and unclear histogram peaks.

- Region-based methods:

This approach partitions an image into different regions by satisfying some homogeneity criteria. Gray level pixel values are used as homogeneity criteria. Region-based segmentation includes different techniques, viz., Region Merging, Region Splitting and Split and Merge. *"Split and Merge"* is a hybrid approach, taking the advantages of both methods. In this approach, pixels are grouped by satisfying some similarity criterion. The selection of the similarity criterion plays an important role in accurate segmentation. Suárez-Cuenca *et al*. [32] developed a 3-D (Three-dimensional) region-growing algorithm for accurate nodule segmentation. Initially, the nodule candidates were detected by a selective enhancement filter and thresholding approach. The researchers have detected 71.8% of nodules at 0.8 false positives per case, 75.5% at 1.6 FPs/case, and 80% at 3.4 FPs/case respectively. The region-based algorithm gives poor results as compared to a threshold-based nodule detection approach. The primary disadvantage of Region-based approach is that it requires careful manual interaction for seed point initialization as well as proper seed planning for the regions that need further processing. Although the Split and merge technique does not require a seed point. Apart from that, different extracted regions may contain holes or even disconnected. These algorithms are also sensitive to noise.

- Clustering-based methods:

This method based on the division of pixels into homogeneous clusters. This is an unsupervised approach to image segmentation method. It finds the natural grouping of pixels by executing certain criterion function. Different clustering algorithms, e.g., K-means or ISODATA algorithm, fuzzy c-means (FCM) and the expectation-maximization (EM) algorithm have been applied extensively for medical image segmentation. Filho *et al*. [33] proposed a CADe system based on the Quality Threshold (QT) algorithm and the Diversity Index. The QT algorithm was used for nodule candidate detection. Javaid *et al*. [34] have used the K-means algorithm for nodule detection. Initially, the number of classes has been chosen as three (3). Next, the class with the highest mean intensity value was chosen as the nodule cluster. Juxtavascular nodules are attached to the blood vessels. Therefore, the separation of blood vessels from the Juxtavascular nodule is a crucial task. The researchers have categorized these attachments (connection) as 2-D and 3-D type. If vessels were connected to a nodule in a single slice, it was called *"2-D connection"*. On the other hand, a *"3-D connection"* was defined as the branches and nodules that appear to be separated objects on a single slice but were attached in any previous or some next slice. Researchers have used a shape specific morphological opening operation to break the 2-D connection. A Structuring Element *"Line"* with parameters length and angle has been used by their study. Removal of 3-D connected branches has been done by comparing the areas of 3-D connected regions on each slice. Finally, all nodule candidates were grouped into six classes by using the proposed equations, viz., *"Nodule Thickness"* and *"% of wall connectivity"*. Nithila and Kumar [35] have presented a new technique that incorporates Particle Swarm Optimization (PSO) algorithm with Back Propagation Neural Network (BPNN). Nodules were initially detected by using FCM clustering. The data points have been clustered into three different intensity levels; low, medium and high. Spherical objects have been identified using roundness rule, and tubular structures were removed using elongation rule. Farahani *et al*. [36] developed a type-II fuzzy algorithm for the quality improvement of raw CT images. Then modified spatial kernelized fuzzy c-means (MSFCM) clustering algorithm has been used for internal structure segmentation. After that, morphological opening, closing and filling operations have been used for nodule candidate detection. Netto *et al*. [37] developed a CADe system based on Growing Neural Gas (GNG) clustering algorithm. Initially, candidate nodules were detected using GNG algorithm. Next, nodule candidates were further regrouped using 3-D region growing algorithm for volume reduction. Hosseini *et al*. [38] proposed an automatic system that can learn and tune Gaussian interval type-2 membership functions (IT2MFs). Finally, the system has been applied for lung nodule detection. It has been observed that the detection sensitivity varies from 85.91% with 1.82FPs/exam [33] to 93.2% [36] by using the clustering-based methods. An accuracy of 98% (for solid nodule), 99.5% (for part-solid nodule) and 97.2% (for non-solid nodule) respectively has been achieved by the work of Nithila and Kumar [35]. Farahani *et al*. [36] also have achieved an accuracy of 96.5% by using this approach. As compared to the previous threshold and region-based detection approaches, the detection accuracy of clustering approach is higher with lower false positives. Most of the clustering algorithms require initial parameters. This approach does not consider spatial modelling and can be sensitive to noise and intensity inhomogeneities. The lack of information and uncertainty in data can be dealt with the FCM algorithm by using a membership function. Fuzzy If-Than rules could be utilized to do approximate inference. However, choosing or designing an appropriate membership function is not a trivial task and calculations involved in fuzzy approaches could be intensive. Apart from the above mentioned techniques, different approaches based on Partial differential equation [39-40], Model [41-42], Atlas [43], Template Matching [44-46], and Filtering [47-49] do exist in literature. Few nodule detection processes using feature engineering approach with reported best performance have been given in Table 1.1.

Table 1.1: Different Nodule Detection System using Feature Engineering approach in Lung CT Images

Sl. No.	First author with reference number	Nodule Detection Process	Performance
1.	Sousa *et al*.[26]	3-D skeletonization algorithm	Sensitivity = 84.84%, specificity = 96.15%, and accuracy = 95.21%
2.	Messay *et al*.[27]	Combined intensity thresholding and morphological processing	Sensitivity= 82.66%, with an average of 3 FPs per CT scan/case
3.	Mehre *et al*.[30]	Combinations of thresholds and structuring elements	Sensitivity = 92.91% with 3 FP/scan
4.	Suárez-Cuenca et al. [32]	3-D region-growing algorithm	71.8%of nodules detected at 0.8 false positives per case, 75.5% at 1.6 FPs/case, and 80% at 3.4 FPs/case, respectively
5.	Filho *et al*.[33]	Quality threshold (QT) algorithm	Accuracy = 97.55%, sensitivity = 85.91%, specificity = 97.70%, with a false positive rate of 1.82 per exam and 0.008 per slice and area under the free-response operating characteristic is of 0.8062
6.	Javaid *et al*.[34]	K-means algorithm	Accuracy = 96.22%, sensitivity = 91.65% with 3.19 FPs per case, and sensitivity =83.33% for small size nodule
7.	Netto *et al*.[37]	Growing neural gas (GNG) clustering algorithm	The methodology ensures that nodules of reasonable size be found with sensitivity = 86%, specificity = 91%,

			and a mean accuracy of 91%
8.	Gonga *et al*.[44]	3-D dot filtering combined with dynamic self-adaptive template matching algorithm	Sensitivity = 90.24% with 4.54 FPs/scan in LIDC dataset, sensitivity = 84.1% with 5.59FPs/scan in ANODE09 dataset
9.	Choi and Choi [47]	Multi-scale dot enhancement filter with angular histogram of surface normal (AHSN) feature	Accuracy = 97.4%, overall sensitivity = 97.5% with 6.76 FPs/scan, and specificity = 97.7%
10.	Jaffar *et al*.[48]	Multi-scale filter based on the eigen values of Hessian matrices	Accuracy = 98.7% and sensitivity = 97.5%

1.3.2 Lung Cancer: A Deep Learning Approach

Deep learning algorithms have become a valuable tool in the field of medical imaging, used for lesion detection, characterization, and analysis. This methodology consists of designing layer wise network architecture by keeping in mind the goal of higher classification accuracy. The learning methods have classified as supervised and unsupervised, in the view of machine learning paradigm. Auto-encoders (AEs), stacked auto-encoders (SAEs) are examples of unsupervised network models because the labelled training data is absent and only the input image has given to the network. On the other hand, Convolutional Neural Networks (CNNs) are the example of supervised network model [50]. Among existing models, Convolutional Neural Network (CNN) is the most popular one owing to its simplicity and higher classification accuracy. Therefore, in this study, different CNN based models have been described below:

- 2-D Convolution-based CNN:

In this approach, a basic 2-D convolution operation has been used to find local features from the entire image. This is mostly used CNN architecture for its simplicity and computational efficiency. Most of the images are two-dimensional and contain intensity values in the form of a matrix. Several 2-D filters/features are automatically learned from the training dataset by this network. Setio *et al*. [51] have used multiple streams of 2-D ConvNets. Initially, three candidate detector algorithms specially designed for solid, subsolid, and large nodules have combined for nodule candidate detection. Then for each candidate, a set of 2-D patches of size 64×64 pixels have been extracted from differently oriented planes. The researchers have used nine views for this purpose. Then multiple 2-D ConvNets were used for feature extraction. Finally, the outputs of different networks have been merged by applying three fusion techniques, viz., Committee-Fusion, Late-Fusion, and Mixed-Fusion. The authors have reported that Late-Fusion technique gives better detection performance in comparison with Committee-Fusion and Mixed-Fusion technique. Ciompi *et al*. [52] have used a 2-D CNN architecture named as "OverFeat" for peri-fissural nodule detection. The architecture used six convolutional layers, with filter size ranges from 7×7 to 3×3. Next, three view images (axial, coronal and sagittal) were fed to the "OverFeat" architecture for nodule feature extraction. Finally, researchers have used a two-stage classifier for peri-fissural nodule detection. Shen *et al*. [53] have designed a Multi-crop Convolutional Neural Network (MC-CNN) by introducing a "multi-crop" pooling strategy for automatic lung nodule characterization. Researchers have used a single network that was capable of producing multi-scale features, instead of using multiple CNN. They proposed a multi-crop based pooling operation strategy. The final multi-crop feature has been computed by concatenating previous layer features. The work has used Randomized Leaky Rectified Linear Unit (RReLU) as an activation function and the SGD learning algorithm that minimize the cross-entropy loss. The proposed architecture was also able to perform semantic label prediction by computing two attributes, viz., nodule subtlety and margin and can estimate nodule diameter with considerable results.

- 3-D Convolution-based CNN:

In this network, the basic convolution operation has been applied in three directions (x,y,z) at the same time. The convolutional filters used are 3-D, and have applied over the input 3-D data for automatic feature extraction. These networks are more expensive in terms of computation efficiency than 2-D based network. Convolution operations based on 3-D need more calculations and more memory because 3-D matrix is required to store the extracted features in computer memory. The main advantage of 3-D CNN is that it produces multi-view features with the help of 3-D filters. Dou *et al*.[54]have proposed a 3-D CNN based architecture for lung nodule detection. Researchers have used three 3-D CNNs to encode spatial information and representative features using hierarchical architecture. For the first architecture, a receptive field of size 20×20×6 has been used, for second architecture, the size was 30×30×10 and for third architecture, it was 40×40×26. Finally, the CNNs have fused to act as a feature extractor for nodule detection. The proposed architecture has been validated by participating in LUng Nodule Analysis 2016 (LUNA16) challenge and has achieved a sensitivity of 94.4%, for nodule detection.

- 2-D-3-D Convolution-based CNN:

The 2-D and 3-D convolution operations can be combined and used to design a hybrid network; we named it as 2-D-3-D CNNs. The network is capable of capturing both 2-D and 3-D features from the lung nodule image. In general, the 3-D patch branch is capable of learning multi-view features from multiple CT slices whereas the 2-D patch branch learns multi-scale features. Wang *et al*. [55] have proposed a central focused convolutional neural network (CF-CNN) learning model by emphasizing nodule segmentation. The architecture consists of two paths, viz., 3-D CNN based path and a 2-D CNN based path. This architecture is a good example of patch-based nodule segmentation approach. Variations in the lesion have been captured using both 2-D and 3-D features from the dataset. The voxels close to center of the image patch were more relevant to the target voxel than the voxels close to edges. Owing to this reason, the researchers have proposed a centrally focused pooling operation. This type of pooling operation reserves location information which was not captured in conventional max pooling operation. In central pooling operation, the pooling kernel size varies according to the pooling position and non-uniformly distributed on an input image. On the other hand, in traditional max-pooling operation the pooling kernels are of the same size and uniformly distributed. A parametric rectified linear unit (PReLU) has been used as activation function for more effective and promising results than the conventional Rectified Linear Unit (ReLU). Researchers have achieved a Dice score of 82.15% in LIDC dataset.

- Fusion-based CNN:

In this network, hand-craft based features can be combined with the CNN based extracted features to form the final feature vector. We have named the network, using this approach, as fused based CNN. Yuan *et al*. [56] have categorized five types of lung nodule, viz., Well-circumscribed, Juxta-pleural, Juxta-vascular, Pleural-tail, and GGO using CNN. Researchers have used a multi-view multi-scale CNN pre-trained with VGG network. Different statistical features were extracted from the nodule image. Next, Scale-invariant Feature Transform (SIFT) was computed and encoded in the form of Fisher Vector (FV). The Gaussian Mixture Model (GMM) has been used to compute the Fisher geometrical features. Finally, all the handcrafted features were fused with CNN extracted features by using Multiple Kernel Learning (MKL). Researchers have achieved an overall accuracy of 93.1%. Xie *et al*. [57] have fused hand-crafted textural and shape-based features with automated deep features (Fuse-TSD) by using deep convolution neural network for nodule characterization. The fused features were Gray-level co-occurrence matrix (GLCM) texture (T), Fourier shape descriptor (S) and deep learning-based features (D).The authors fused the extracted features in the decision level (decision fusion) which was the output of a fully connected layer. The same features were also fused on the feature extractor level (feature fusion), i.e., before feeding to the classifier. Authors have reported that fusion at decision level was given better performance than at the feature level. Therefore, Fuse-TSD can be used as a higher-level decision fusion based classifier over both manual and automated segmentation process.

- Pre-trained CNN:

"Transfer learning" is one most important concept in deep learning. In this scenario, the CNN is trained on a large and different dataset. The final weights of the CNN were fined tuned and then used for object detection or classification. This is very helpful as the availability of the medical imaging data is limited, so a network trained with different datasets and modality can be used for the task of deep feature extraction. Paul *et al*.[58] proposed a new CNN architecture for lung nodule characterization. Researchers have used a pre-trained VGG network trained with the Imagenet dataset. Three networks, viz., vgg-f, vgg-m and vgg-s have been used for this purpose. Here, the f, m and s stand for fast, medium, and slow and refer to training time. Vgg-s has been chosen as final pre-trained architecture, as it gives higher classification accuracy. Next, 4096 deep features have been extracted by using vgg-s. Next, three CNN architectures have been trained independently by using the cancerous dataset from NLST. Next, *"Architecture-3"*, a cascaded CNN, has been chosen for its higher classification accuracy and 1024 deep features were extracted. Finally, nodules were characterized by using all the deep features extracted by using *"Architecture-3"*, fused with 219 radiomics (Hand-Crafted/Feature Engineering) features for higher classification

accuracy. Researchers have reported an accuracy of 76.79% using pre-trained CNN. Table 1.2 shows different CNN-based works with reported best performances that have been used for nodule detection and characterization.

Table 1.2: Different nodule detection and characterization system using CNN-based deep learning approach in lung CT images

Sl. No.	**First author with reference number**	**Method**	**Purpose**	**Performance**
1.	Setio *et al*. [51]	Multiple streams of 2-D ConvNets (multi-view architecture)	Nodule Detection	Sensitivity= 85.4% with 1 FP/Scan and 90.1% with 4 FPs/Scan
2.	Ciompi *et al*.[52]	2-D convolution based architecture named as "OverFeat"	Peri-fissural nodules(PFNs) detection	Area Under Curve(AUC)= 0.868
3.	Shen *et al*. [53]	Multi-Crop Convolutional Neural Network (MC-CNN)	Nodule Characterization	Accuracy=87.14%, AUC= 0.93, Sensitivity= 77%, Specificity =93%.
4.	Dou *et al*. [54]	Three 3-D CNN applied with fusion technique	Nodule Detection	Sensitivity=94.4%, and Sensitivity=92.2% at 8FPs/scan
5.	Wang *et al*. [55]	Data-driven based machine learning model using central focused convolutional neural network (CF-CNN)	Nodule Segmentation	Dice Score=82.15% (LIDC dataset) and 80.02% (GDGH dataset)

6.	Yuan *et al*. [56]	Pre trained vgg network followed by CNN based features fused with hand craft based features (multi-view multi-scale CNN)	Nodule Categorization	Overall Accuracy=93.1% (LIDC dataset) and 93.9% (ELCAP dataset)
7.	Xie *et al*. [57]	Used CNN at decision level	Nodule Characterization	AUC of 96.65%, 94.45% and 81.24%
8.	Paul *et al*. [58]	Pre trained vgg-s network with merge CNN	Nodule Characterization	Accuracy=76.79%, ROC=0.87

1.4 Motivation of the Thesis

In the above discussion on CAD-based detection and diagnosis system depict that different ML and DL-based frameworks exist in the recent literature survey. To promote and develop CAD based systems, proper image analysis with higher classification accuracy is the utmost requirements. However, the integration of some advanced feature extraction-based tools in the development of CAD-based system is not fully reliable to meet the specific requirement. Therefore, it is pertinent to mention that the lung nodule detection and characterization needs to be carried out to form an expert system that can explore the input HRCT images effectively with higher classification accuracy. In our works, the proposed CAD frameworks have performed well by processing the captured HRCT images through automated feature extraction and classification module using proposed machine and deep learning techniques to come up with promising results.

1.5 Aims and Objectives of the Thesis

The main objective of the thesis is to design and develop some image processing and deep learning algorithms for CAD-based lung nodule detection and characterization systems. The specific objectives are listed as follows:

- Development of machine learning-based CADe system by incorporating morphological operations for lung nodule segmentation and detection.
- Development of a deep learning framework for lung nodule segmentation and characterization using multi-scale features.
- Development of deep learning-based CAD system by incorporating morphological operations for lung nodule characterization.
- Implementation of a deep learning framework for lung cancer subtype classification for an improved computer-aided diagnostic system.

1.6 Existing Research Gaps

It is being observed from the above mentioned survey that a large number of studies have been conducted for lung nodule detection and characterization. Though different state-of-the-art methods obtain impressive results, the following issues are still unaddressed and or can be improved by continuous research activities.

Summarizing all the nodule detection and characterization algorithms, the main problems have been noted as follows:

- The reduction or suppression of vessels like structures in the HRCT images has not been addressed well in the literature so far. Malignant nodules exhibit deformable shape in HRCT images. Therefore, accurate shape and size estimation of malignant nodule is a challenging tasks. Invention of accurate and robust segmentation algorithm is the prerequisite to overcome the mentioned limitations and for the development of state-of-the-art CAD systems. But from literature survey it has been observed that very few works have been able to capture the deformable property of lung nodule for accurate detection and characterization. Therefore, further research is required towards this direction.

- Multi-scale features can play an important role for accurate nodule detection and characterization. It can be seen from the survey that more works should be explored using latest deep learning tools that can capture multi-scale features automatically from the HRCT slices for better development of CAD-based system.
- It has been observed from the survey that although different deep learning based framework have been developed using convolution operation for lung nodule detection and characterization but no deep learning framework has been introduced that can capture nodule structure automatically using image morphology operations. Therefore, new DL framework can be developed by utilizing mathematical morphology operations.
- Deep learning systems can be developed by combining latest attention-based mechanism with image morphology operations. But no DL framework has been developed for lung nodule detection, characterization, and lung cancer subtype classification using this combined approach.

1.7 Original Contributions of the Thesis

This thesis aims to present new innovative solutions for the improvement of computer-aided diagnosis system for lung cancer. The original contributions of each subsection are discussed below:

1.7.1 Lung Nodule Detection using the Concept of Superpixel

Lung nodule detection from HRCT images plays a vital role for early detection of lung cancer. Detection of lung nodules from HRCT slices is a time consuming and difficult tasks for the radiologists. Therefore, CADe based system plays a vital role for accurate nodule detection in lesser amount of time. In this work, a new CADe framework has been developed that can detect lung nodule automatically from HRCT images. Initially iterative threshold algorithm has been used to extract the lung regions from the CT image. After that internal structure of the lung has been segmented by developing a new methodology using the concept of superpixel. The proposed technique can detect and segment lung nodule regions accurately. After that different shape-based features have been used to recognize the lung nodule. Vessels have been removed by using elongation feature. The proposed system has been tested and analysed on publicly available Lung Image Database Consortium-Image Database Resource Initiative (LIDC-IDRI) dataset. It has been observed that owing to the introduction of superpixel-based algorithm, the developed system has identified the actual nodule location accurately and obtained higher detection accuracy on LIDC-IDRI dataset. The major findings are as follows:

- A new nodule detection system has been introduced based on the concept of superpixel.
- A new superpixel-based segmentation algorithm has been developed for accurate nodule segmentation.
- Morphological features have been used by the framework for nodule detection.

1.7.2 Gaussian Mixture Model Based Framework for Lung Nodule Detection

Lung cancer is one of the deadliest human disorders in all over the world. Early stage detection and identification of lung nodules from widely used HRCT images, helps in prevention of the disease. This thesis work is aimed to develop an automated computer-aided lung nodule detection system from HRCT images to provide a reliable second opinion to the radiologists and experts for further treatment. In this work a morphological filter aided Gaussian Mixture Model (GMM) has been introduced for nodule segmentation and candidate detection. The framework segments the internal high density structures, e.g., blood vessels and nodules from the pulmonary parenchyma by employing Gaussian Mixture Model based segmentation technique. After that a new nodule candidate detection methodology has been introduced by employing binary morphological opening operation. Three filter banks with different sized circular structuring element (SE) have been developed and tested for nodule candidate detection and false positive (FP) reduction. The proposed morphology-based image filter is able to detect the candidate nodule locations accurately from the HRCT images with less number of false positives (FPs). Next, in this study, features based on shape and intensity has been used to identify the true nodules. It has been observed that owing to the introduction of morphology-based filter, the proposed framework has generated less number of FPs and obtained higher nodule detection accuracy on LIDC-IDRI dataset. The major outcomes are listed below:

- A new nodule detection framework has been developed using image morphology.
- Gaussian Mixture Model (GMM) has been introduced for finer structure extraction inside the lung regions.
- A new morphology-based filter has been introduced for false positive reduction and accurate nodule detection.
- Different shape and intensity-based features have been used by the system for better nodule detection.

1.7.3 Adaptive Morphology Aided Framework for Lung Nodule Segmentation and Detection

Lung cancer is one of the most life-threatening cancers mostly indicated by the presence of nodules in the lung. Doctors and radiological experts use HRCT images for nodule detection and further decision making from visual inspection. Manual detection of lung nodules is a time-consuming process. Therefore, CADe systems have been developed for accurate nodule detection and segmentation. CADe-based systems assist radiologists to detect lung nodules with greater confidence and a lesser amount of time and have a significant impact on the accurate, uniform, and early-stage diagnosis of lung cancer. Lung nodules are highly deformable in shape. Therefore, to capture the deformability, in this research work, an adaptive morphology-based segmentation technique (AMST) has been introduced by designing an adaptive morphological filter for improved segmentation of the lung nodule region. The adaptive morphological filter detects candidate nodule regions by employing adaptive structuring element (ASE). The ASE can change its orientation and shape by observing data variations and able to capture true nodule structure in HRCT slices. Therefore, the proposed framework improves nodule detection accuracy by reducing false positives (FPs) drastically. Next, the detected candidate nodules are processed for feature extraction. In this study, morphological, texture and intensity-based features have been used with support vector machine (SVM) classifier for lung nodule detection. The performance of the proposed framework has been evaluated by incorporating a 10-fold cross-validation technique on LIDC-IDRI dataset and on a private dataset, collected from a consultant radiologist. It has been observed that the proposed automated computer-aided detection system has outperformed the other state-of-the-art methods for automatic nodule detection from the HRCT image. The major contributions are listed below:

- An improved lung segmentation algorithm is presented employing image morphology-based operations.

- Considering the morphological and deformable properties of the lung nodules, adaptive structuring elements have been introduced for the development of morphological filters.

- Grayscale adaptive morphological filters are developed for the segmentation and detection of large varieties of candidate nodules.

- Different shape, intensity, and texture-based features have been used by the framework for lung nodule detection in HRCT image.

1.7.4 An Integrated Deep Learning System for Lung Nodule Segmentation and Characterization

Lung cancer has been recognized as the most life-threatening cancer all over the world. Appropriate detection of lung nodule using Computed Tomography (CT) images helps in early stage recognition of lung cancer. Different computer-aided algorithms play an important role in the early diagnosis of lung cancer and can increase the five-year survival rate of lung cancer patients. However, due to structural similarity, manually recognizing the malignant nodule from the benign is time-consuming and challenging task. Recently different deep learning based CADx systems have been developed for lung nodule characterization. In this work, an integrated nodule segmentation and characterization framework has been developed using the concept of atrous convolution. The proposed Atrous Convolution-based Convolutional Neural Network (ATCNN) framework can segment and characterize lung nodules by capturing multi-scale features from the HRCT images. Different variants of the ATCNN framework have been analysed for lung nodule characterization. Among them, ATCNN with a two-layer atrous pyramid and residual connections (ATCNN2PR) has demonstrated the highest classification performance indices for nodule characterization in LIDC-IDRI dataset. The proposed automatic trainable end-to-end deep learning system has outperformed other competing frameworks by capturing multi-scale features from High-Resolution Computed Tomography nodule images. The primary findings are written below:

- An integrated deep learning framework has been developed for lung nodule segmentation and characterization.
- A new framework based on atrous convolution has been introduced.
- A novel attention-based mechanism has been incorporated for better nodule segmentation.
- Multi-scale features have been captured to classify lung nodule.
- Residual connections have been introduced for better feature preservation.
- The proposed segmentation framework has been compared with existing state-of-the-art segmentation frameworks.

1.7.5 An Adaptive Morphology Aided Deep Learning Framework for Lung Nodule Characterization

Early-stage detection and identification of malignant pulmonary nodules can allow proper medication and increase the survival rate of lung cancer patients. HRCT image slices are in use for the screening of lung cancer. However, appropriate identification of lung nodules at the early stage of the disease is challenging owing to similar morphological properties of benign and malignant nodules. Introduction of computer vision and advanced image analysis techniques for the development of CADx systems have significantly improved the classification performance and increase the speed the interpreting lung CT images for the identification of lung cancer. Deep learning-based techniques have recently emerged as an efficient tool for the improved characterization of lung nodules. In this research work, a DL based framework has been introduced using the concept of adaptive morphology-based operations combined with Gabor filter (GF) for accurate lung nodule classification. The new framework, 2-Pathway Morphology-based Convolutional Neural Network (2PMorphCNN) with its two trainable paths can capture both textural and morphological features of the lung nodules that results in better classification accuracy. The proposed system has been trained and evaluated on publicly available LIDC-IDRI dataset for nodule

characterization. It has been observed that the reported automatic lung nodule classification framework outperforms other state-of-the-art nodule classification methodologies by capturing and combining textural and morphological features from the HRCT lung nodule image.
The main contributions are as follows:

- An improvised CNN model combined with morphological operations has been developed for lung nodule characterization.

- An adaptive morphology-based weight initialization scheme has been introduced to capture deformable properties of lung nodule.

- A Gabor filter-based weight initialization scheme has been developed to capture textural information from nodule region.

- Morphological and textural features are combined using two trainable parallel paths of the CNN model for improved classification of pulmonary nodules.

1.7.6 An Attention-Based Morphology Aided Deep Learning Framework for Lung Cancer Subtype Classification

Lung cancer is recognized as the most life-threatening cancer among other type of cancers all over the world. Early stage recognition and proper diagnosis can increase the five-year survival rate and also save the patient life. Accurate identification of lung cancer subtype from histopathological images plays an important role and help doctors to take necessary decisions for lung cancer treatment. Therefore, in this work, a new deep learning framework based on image morphology is developed for lung cancer subtype classification. The proposed *Morp*hology-based *Atten*tion *Net*work, (MorphAttnNet) is able to classify benign, adenocarcinoma (ADC), and squamous cell carcinoma (SCC) from histopathology images. The framework is designed based on convolution and morphological operations. Attention-based mechanism is incorporated to select important features from histopathology images. The framework with its morphology-based path combined with attention blocks is able to capture morphological variations of lung cancer subtypes accurately and effectively. Finally, the extracted deep features from convolution and morphological paths are combined and used for lung cancer subtype classification. The performance of the proposed framework is analysed on publicly available LC25000 dataset for lung cancer subtype classification. The proposed system is also compared with existing state-of-the-art systems and achieved considerable performance indices for lung cancer subtype classification. The primary outcomes are as follows:

- A new deep learning framework has been developed using image morphology for lung cancer subtype classification.
- Attention mechanism has been incorporated for accurate lung cancer subtype classification.
- The effect of attention-based morphological operations has been analysed for lung cancer subtype classification.
- The proposed framework has been compared with state-of-the-art frameworks for lung cancer subtype classification.

1.8 Organization of the Thesis

The objective of the thesis is to develop image processing and deep learning algorithms for computer aided diagnosis system. A brief description of each chapter is provided as follows:

In ***Chapter 1***, the knowledge of computer-aided detection and diagnosis system is presented. First, it introduces the concept of automatic disease detection and classification system with its area of applications. Then, different CAD-based machine learning and deep learning frameworks have been described elaborately for lung cancer detection and characterization. Existing research gaps of CAD-based systems are also highlighted in this chapter. Finally, the objectives of the present thesis and its contributions are stated elaborated for lung cancer detection, characterization, and subtype classification.

In ***Chapter2***, an efficient lung nodule detection scheme has been developed using the concept of superpixel. Initially the left and right lungs are segmented using iterative threshold algorithm. Then nodule regions have been separated with the help of a proposed superpixel-based algorithm. In this work, shape features have been used to recognize lung nodules. The proposed system has obtained better performance indices on LIDC-IDRI dataset for lung nodule detection.

In ***Chapter3***, a new nodule detection system has been introduced using the concept of Gaussian Mixture Model and image morphology. Initially the internal structure of lung regions has been segmented using GMM algorithm. After that a proposed morphology-based filter has been applied to remove vessel like structures from the HRCT images. Morphological binary opening operation has been used to extract nodules. Circular like structuring element has been used for this purpose. Different shape-based features viz., circularity, eccentricity, solidity, and extent has been used for nodule detection process. The proposed framework has obtained considerable classification accuracy on LIDC-IDRI dataset.

In ***Chapter 4***, a machine learning-based model has been developed for lung nodule detection. The proposed system incorporates the concept of adaptive morphology for better nodule segmentation and detection. An adaptive morphology-based image filter has been introduced for false positive reduction. The framework is able to segment the lung and nodule regions accurately from HRCT images. Finally the feature extractor module extracts features for nodule detection. It has been observed that owing to the introduction of adaptive morphology-based operations the proposed framework has obtained higher performance indices for nodule segmentation and detection on LIDC-IDRI dataset.

In ***Chapter 5***, an integrated deep learning framework has been modelled for lung nodule segmentation and characterization. The proposed system is able to extract multi-scale features from HRCT images using atrous convolution. The system consists of two modules viz., segmentation and classification. Both the modules of the framework have used atrous convolution operation as its basic building block. In this chapter a new segmentation scheme has been introduced by combining attention mechanism with atrous convolution operation. Experimental results reveal the efficacy of the developed system qualitatively and quantitatively on LIDC-IDRI dataset. It has been observed that owing to the introduction of atrous convolution operation-based blocks the framework has obtained considerable nodule segmentation and classification accuracies as compared to the state-of-the-art frameworks.

In ***Chapter 6***, a new deep learning framework has been introduced for lung nodule characterization. The basic building blocks of the framework have used convolution and image morphology-based operations. Apart from that two new weight initialization algorithms have been proposed for better results of the system. The weight matrices of Path-1 of the framework have used Gabor filter whereas Path-2 has been initialized with the concept of adaptive morphology for lung nodule characterization. The proposed system with its morphological path (Path-2) is able to extract morphology-based features automatically from HRCT images. It has been validated experimentally that the reported automatic lung nodule classification framework outperforms other state-of-the-art nodule classification methodologies by capturing and combining textural and morphological features from the HRCT lung nodule image.

In ***Chapter 7***, a novel deep learning framework has been developed by combining the attention-based mechanism and image morphology operation for lung cancer subtype classification. The system is able to classify lung cancer subtypes viz., benign, adenocarcinoma (ADC), and squamous cell carcinoma (SCC) from histopathology images. The framework with its morphology-based path combined with attention blocks is able to capture morphological variations of lung cancer subtypes accurately and effectively. Finally, the extracted deep features from convolution and morphological paths are combined and used for lung cancer subtype classification. The performance of the proposed framework is analysed on publicly available LC25000 dataset and achieved considerable performance indices for lung cancer subtype classification.

Chapter 8 concludes all the research works presented in this thesis. Moreover, possible future research scopes are highlighted in this chapter. The entire work presented and demonstrated in this thesis is divided into eight different chapters. The major research works are distributed among six chapters (Chapter 2 to Chapter 7). Individual chapters aim to solve the detection, characterization, and classification of lung cancer using machine learning and recent most deep learning techniques for an improved computer-aided diagnostic system.

• Publication:

Amitava Halder, Debangshu Dey and Anup Kumar Sadhu, “Lung Nodule Detection from Feature Engineering to Deep Learning in Thoracic CT Images: a Comprehensive Review,” in *Journal of Digital Imaging, Springer,* (Impact Factor: 5.40), vol. 33, no. 3, pp. 655-677, Jan. 2020, doi: 10.1007/s10278-020-00320-6.

Chapter 2

Lung Nodule Detection using the Concept of Superpixel

2.1 Background and Motivation

Lung Cancer is the world's most life-threatening cancer that causes deaths all over the world. It is identified as the uncontrolled growth of lung cells leading to interference with the function of the respiratory system. These uncontrolled lung cells/pathologies are named Solitary Pulmonary Nodule (SPN) or lung nodule [8]. For a doctor or radiologist, it is very difficult to detect the lung nodule having a complex anatomical structure with bifurcation points in the chest wall from a visual inspection only. Detection of lung nodules at an early stage is important for further treatment and prevention of the disease. Literature suggests an incremental survival rate of up to 65-80% for early detection [59]. The recent development in imaging modalities introduces the HRCT imaging technique for more insight visualization of the nodule region. But a typical CT scanner produces a large volume of slices for investigation, which may cause the radiologist to miss some medium/small size nodule owing to fatigue. To overcome this problem different automated CADe systems are being developed which acts as a second opinion for radiologists and experts. The CADe system is developed to detect nodules from a series of CT slices with a higher degree of accuracy. Inthe literature, different nodule detection techniques are proposed by various researchers. Messay et al. [27], Suiyuan et al. [60] proposed a nodule detection framework based on the thresholding technique. Ozekes et al. [61] have introduced a 3- D template-matching approach for nodule detection. Filtering based approaches, e.g., Hessian filter, Dot enhancement filter have been used extensively in [47, 62]. Cuenca et al. [63] have proposed an iris filter based technique to identify true nodules from false-positive (FP) findings, e.g., blood vessels from CT images. Riccardi et al. [64] presented a 3-D fast radial (FR) transform based filter for nodule detection. Teramoto et al. [65] have introduced a 3-D filter named as cylindrical nodule-enhancement filter (CNEF) that can reduce false positives (FPs) in the pre-processing stage. Filho et al. [33] used a clustering algorithm, viz., Quality Threshold (QT) for accurate nodule segmentation and detection. Feature extraction and classification plays an important role in nodule detection.

Different features based on 2-D and 3-D morphology [66-68], texture [69] and generic feature [48] can be found in the literature for lung nodule detection.

2.2 Research Contributions

In this chapter a new nodule detection system has been introduced based on the concept of superpixel. Initially iterative threshold algorithm has been used to extract the lung region from the HRCT image. Then a new algorithm has been developed to segment the lung nodule regions using the concept of superpixel. In this work different shape-based features have been used to detect lung nodules from the HRCT image. It has been observed that due to the introduction of superpixel-based segmentation technique the proposed nodule detection system has obtained higher performance indices on LIDC-IDRI dataset [20].

2.3 Superpixel-Based Nodule Detection Framework

The proposed CADe system takes CT images as input and extracts different shape-based morphological features from each region of interest (ROI) for the nodule detection task. The proposed framework consists of five main modules:

a) Preprocessing of lung CT images using median filter.
b) Segmentation of lung regions using Iterative Threshold algorithm.
c) Segmentation of internal structures using Superpixel and Density Based Region (SPDBR) segmentation algorithm.
d) Nodule Candidate detection using Hysteresis threshold and Elongation feature.
e) Nodule detection using morphological features and the SVM classifier.

2.3.1 Dataset Details

The research work has been performed on Lung Image Database Consortium and Image Database Resource Initiative (LIDC-IDRI) [20], which is the world's largest database, consists of 1080 scans of 1010 patients. All the images are of size 512×512 and in DICOM (Digital Imaging and Communication in Medicine) format. The resolution of each image is 16-bit. In this work, a set of 40 nodules from 30 patients has been chosen from the LIDC-IDRI dataset.

2.3.2 Lung Segmentation

In this stage, the left and right lungs are extracted from the artifacts such as the mediastinum and thoracic wall for further processing. The iterative threshold algorithm (Algorithm 2.1) has been implemented in this work, as it can select the optimal threshold automatically in an iterative way from the dataset using a predefined difference value. Then two largest regions are extracted as left and right lung, followed by a morphological closing operation to create a final lung mask. Different outputs obtained for lung segmentation are shown in Figure 2.1.

Algorithm 2.1: Iterative Threshold

Input: Grayscale lung CT image I_m.

$$Step-1: Thr = (Min(\mathrm{Im}) + Max(\mathrm{Im}))/2$$
$$Step-2: \Delta T = 0.01$$
$$Step-3: Done = \ false$$
$$Step-4: While \sim Done$$
$$Gt = \mathrm{Im} >= Thr$$
$$T_{next} = (mean(\mathrm{Im}(Gt)) + mean(\mathrm{Im}(\sim Gt)))/2$$
$$Done = abs(Thr - T_{next}) < \Delta T$$
$$Thr = T_{next}$$
$$Step-5: I_{Seg} = Gt$$

Output: Lung Segmented CT image I_{lung}.

Here, $\Delta T \rightarrow$permitted threshold difference and G_t $\rightarrow$Current thresholded image. Next, the segmented image I_{seg} is filled to obtain the I_{fill} image. The lung mask I_{lungm} is obtained by subtracting the segmented image from the filled image using the following expression:

$$I_{lungm} = I_{fill} - I_{seg} \tag{2.1}$$

Next, a binary closing operation is performed on the created lung mask I_{lungm}, which is then multiplied by the original median filtered lung image to obtain the final lung segmented image I_{lung}.

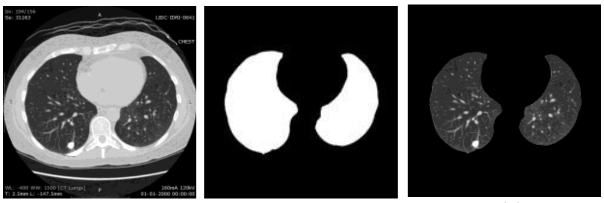

(a) **(b)** **(c)**

Figure 2.1: Lung segmentation: (a) original lung HRCT image, (b) lung mask created by iterative threshold and morphological closing operations, (c) segmented lung regions.

2.3.3 Internal Structure Segmentation using Superpixel

The segmented lung regions are further processed for search space reduction and accurate nodule segmentation. The proposed Superpixel and Density Based Region (SPDBR) segmentation algorithm (Algorithm 2.2) has been introduced for internal structure segmentation. A superpixel (SP) is defined as a group of pixels that maintains some homogeneity criteria. The superpixels (SPs) (Figure 2.2) are formed by Simple Linear Iterative Clustering (SLIC) algorithm [70]. Then the neighboring SPs are merged to form a relatively large homogeneous region using the SPDBR algorithm (Figure 2.3 and Figure 2.4). Euclidean distance function has been used as the distance threshold criterion. It can be observed from Figure 2.5 that the nodule region is better bounded with number of superpixels set to 800, rather than 500 for segmentation process.

Algorithm 2.2: SPDBR

Input: Superpixelized label image (I_l), Number of superpixels (SPs), Distance threshold (ε).

$$
\begin{aligned}
&Step-1: Select\ a\ unvisited\ Superpixel\ SP\\
&Step-2: Explore\ all\ Superpixels\ density\_reachable\\
&\qquad from\ current\ Superpixels\ SP\ by\ following\ minimum\\
&\qquad no.of\ points\ MinPts\ and\ distance\ threshold\ \varepsilon\\
&Step-3: If\ SP\ is\ a\ core\ point,\ form\ a\ cluster\\
&Step-4: If\ SP\ is\ a\ border\ point, choose\ next\ Superpixel\\
&Step-5: Repeat\ Step-1 to\ Step-4 until\ all\ the\ SPs\\
&\qquad have\ been\ processed\ (Visited)
\end{aligned}
$$

Output: Clusters of merged SPs.

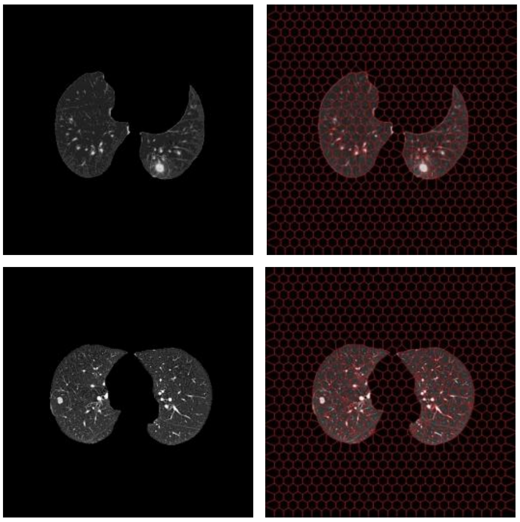

(a) **(b)**

Figure 2.2: Superpixelized image: (a) segmented image, (b) superpixelized image by SLIC algorithm with no. of superpixels (N_{SP}) =800.

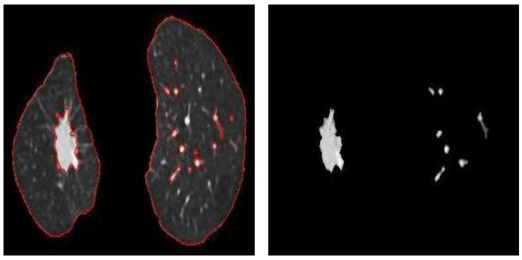

(a) (b)

Figure 2.3: Internal structure segmentation: (a) output image by SPDBR algorithm, (b) thresholded image.

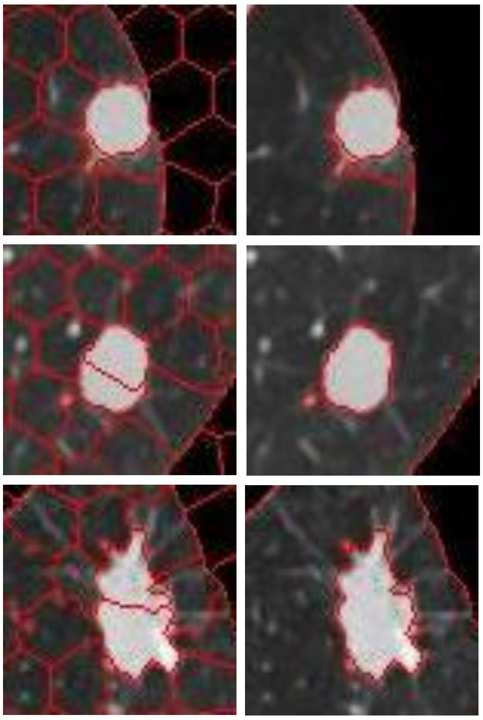

(a) (b)

Figure 2.4: Internal structure merging: (a) superpixelized image, (b) superpixels merged by SPDBR algorithm.

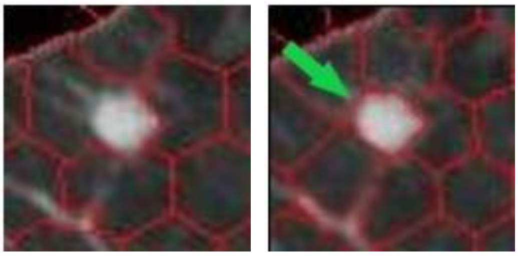

(a) **(b)**

Figure 2.5: Nodule segmentation with: (a) N_{SP} =500, (b) N_{SP} =800.

2.3.4 Nodule Candidate Detection and Feature Extraction

This module has been introduced to detect the regions eligible to fed to the classifier for final decision. The regions are called nodule candidate regions. After segmenting the internal structure a Hysteresis thresholding (Ht) technique has been applied to remove the unwanted low density regions attached with the ROIs. The main advantage of Ht is that it can preserve the narrow low density regions surrounding the candidate nodule, as the pixels will be considered as adjacent to the ROI iff their threshold value between low and high. Next vessels are removed by computing Elongation feature from each thresholded region, where the Elongation is defined as:

$$Elongation = 1 - \frac{Minor\ Axis\,Value}{Major\ Axis\,Value} \tag{2.2}$$

The feature extraction stage is introduced to extract a set of representative morphological features from each of the candidate nodule regions. Quantification of various structural properties of nodules, viz., perimeter, diameter, solidity, eccentricity, aspect ratio, compactness, roundness, circularity, ellipticity, and extent have been used as distinguishing features for further detection of the nodule region.

Perimeter: It is defined as the number of pixels in the boundary of the object.

Diameter: It is defined as the diameter of a circle with the same area as the region, returned as a scalar.

$$D = \sqrt{4 \times Area / \pi} \tag{2.3}$$

Solidity: It measures the density of an object by computing the ratio of area to convex area. The value of solidity is 1 for a solid object. On the other hand, a lower solidity value indicates that the object is irregular.

$$S = \frac{Area}{Convex\,Area} \tag{2.4}$$

Eccentricity: It is defined as the major axis and minor axis length ratio. An elongated object gives a large value of eccentricity. In CT slices elongated regions, e.g., vessels have been removed by using this feature.

$$Eccentricity = \frac{Major\ Axis\ Length}{Minor\ Axis\ Length} \tag{2.5}$$

Aspect Ratio: It is measured as the ratio of the length of the minor axis to the length of the major axis as follows:

$$AR = \frac{Minor\ Axis\ of\ the\ Object}{Major\ Axis\ of\ the\ Object} \tag{2.6}$$

Compactness: Nodules have a compact structure in them. The true nodules show a compactness value near '1'; on the other hand, vessels have much higher values for this feature. It is defined as:

$$C = \frac{Perimeter^2}{4 \times \pi \times Area} \tag{2.7}$$

Roundness: This feature helps to detect round-shaped objects. Lung nodules show higher values for roundness than vessels. It is defined as:

$$R = \frac{4 \times Area}{\pi \times Diameter_{max}^2} \tag{2.8}$$

Circularity: This feature finds the roundness of an object. Thin and elongated objects have less circularity. Whereas a structure that is more or less circular has a circularity value very close to '1'. It is observed that many lung nodules are nearly circular in shape and have a compact structure in them. Therefore, this feature has been considered for nodule detection. The circularity can be computed by using the following equation:

$$Cir = \frac{4 \times \pi \ Area}{Perimeter^2} \tag{2.9}$$

Ellipticity: Lung nodules are not always circular. Nodules may follow the shape of an ellipse. Therefore, in this work**,** this feature has been computed for the detection of nodules that are elliptical in shape. It is measured as:

$$E = \frac{\pi \times Diameter_{max}^2}{2 \times Area} \tag{2.10}$$

Extent: This feature is computed as the ratio of the object area to the area obtained by a bounding box containing the object. A large extent value of an object exhibits that it is circular and less branchy, and on the other hand, a small extent value indicates the object is branchy.

$$Ext = \frac{Area\ of\ Object}{Area\ of\ the\ Bounding\ Box} \tag{2.11}$$

After feature extraction stage, the lung nodules have been classified using SVM classifier [71]. SVM finds the optimal hyperplane that separates all data points of one class from those of the other class. The distance between the hyperplane and the nearest training data points of any class, should be as large as possible for best separation results.

2.4 Results and Discussion

In the pre-processing stage, a 3×3 median filter has been used to eliminate the noise and artifacts. An iterative threshold algorithm with a termination criterion ($\Delta T = 0.01$) is introduced for the extraction of lung regions from the HRCT images. The SLIC algorithm has been implemented with experimentally determined input parameters, the number of superpixels (N=800) and the weighting factor of 20 for superpixel generation and segmentation. It is observed from Figure 2.5 that a small nodule segmented well at N=800 than at N=500. The nodule region bounded well in Figure 2.5 (b); marked by a green arrow. The smallest size of the superpixel is chosen as 1. The adjacent superpixels have been merged based on their pixel density. Next, candidate nodules are generated by combining the Hysteresis threshold with the elongation feature value of 0.55. After that, a 10-dimensional feature vector has been computed from each candidate region and fed to the SVM classifier for nodule detection. The proposed CADe system has been evaluated and tested on LIDC-IDRI dataset by using an SVM classifier with Radial Basis Function (RBF) kernel. The classification performance has been measured by computing the Sensitivity, Specificity and Accuracy with the help of TP (True Positive), TN (True Negative), FP (False Positive) and FN (False Negative) samples. The proposed system has been applied over 30 patients contain 40 nodules and obtain the following results shown in Table 2.1 and Table 2.2. The dataset is partitioned into train and test set in the following ratio *DataSet_1*=50:50, *DataSet_2*=60:40, *DataSet_3*=70:30 and *DataSet_4*= 80:20 respectively. Then the mean sensitivity, specificity, and accuracy are calculated from each subset. After that overall sensitivity, specificity and accuracy of the system is calculated by using the following formulae.

$$Average\,Sensitivity = \frac{1}{n}\sum_{i=1}^{n} mean\_sensitivity(i) \tag{2.12}$$

$$Average\,Specificity = \frac{1}{n}\sum_{i=1}^{n} mean\_specificity(i) \tag{2.13}$$

$$Average\,Accuracy = \frac{1}{n}\sum_{i=1}^{n} mean\_accuracy(i) \tag{2.14}$$

Here, n is the number of partitioned datasets used by the system.

Table 2.1: Sensitivity and Specificity obtained by the framework

#Dataset	**Dataset Training :Test Ratio**	**Mean Sensitivity (%)**	**Mean Specificity (%)**
DataSet_1	50:50	80.72	78.55
DataSet_2	60:40	81.77	87.08
DataSet_3	70:30	80.22	91.70
DataSet_4	80:20	88.75	89.16

Table 2.2: Accuracy obtained by the framework

#Dataset	Dataset Training :Test Ratio	Mean Accuracy (%)
DataSet_1	50:50	80.94
DataSet_2	60:40	84.23
DataSet_3	70:30	85.60
DataSet_4	80:20	88.23

The average sensitivity, specificity, and accuracy of the proposed system obtained from Table 2.1 and Table 2.2 are 82.86%, 86.62%, and 84.75% respectively. Below a 2×2 confusion matrix has been plotted for *DataSet_4* (Figure 2.6), which shows that 8 nodules (TP) and 8 vessels and bifurcation points (TN) have been identified correctly with no false positives and only 1 false negative. The sensitivity of the proposed system has been compared with existing nodule detection systems as shown in Table 2.3.

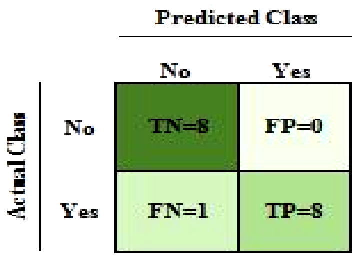

Figure 2.6: A Confusion matrix for *Dataset_4*.

Table 2.3: Performance comparisons of Proposed CADe system with existing systems based on sensitivity on the LIDC-IDRI dataset

CADe System	Sensitivity (%)
Riccardi *et al.* [64]	71%
Teramoto *et al.* [65]	80%
Torres *et al.*[72]	81.6%
Proposed method	**82.86%**

2.5 Summary

The reported work has focused on the detection of lung nodules from HRCT images based on a superpixel density-based region segmentation algorithm, followed by the extraction of different morphological features. An SVM classifier has been trained using the shape-based features for nodule detection. The work has been applied to the LIDC-IDRI dataset and achieved a classification accuracy of 84.75%. However, the proposed system is not tested on other features, e.g., texture, statistical and intensity-based features. Therefore, a thorough investigation is required to improve the classification accuracy of the system by introducing new features combined with existing features. Morphological image processing plays an important role in object detection and segmentation. In the future, CAD systems will be developed by incorporating the concepts of morphological image processing.

• Publication:

Amitava Halder, Saptarshi Chatterjee and Debangshu Dey, “Superpixel and Density Based Region Segmentation Algorithm for Lung Nodule Detection”, in *Proc. of 2020 IEEE Calcutta Conference (CALCON)*, Kolkata, 2020, pp. 511-515, doi: 10.1109/CALCON49167.2020.9106569.

Chapter 3

Gaussian Mixture Model-Based Framework for Lung Nodule Detection

3.1 Background and Motivation

Lung nodule detection is an important stage for early diagnosis of lung cancer and proper treatment planning. According to the data provided by the American Cancer Society (ACS) [5] a total of 2000 patients died in 2018 and a total of 2500 patients have been estimated for the year 2020. In this context, to deal with such a large number of patient data, the CAD system may provide a suitable solution through improved performance for nodule detection in a smaller duration of time. The state-of-the-art CAD-based systems are divided into two categories, viz., CADe and CADx systems that are used for nodule detection and characterization respectively. Different CADe systems have been introduced so far to identify the accurate location of lung nodules from a set of CT slices. Literature suggests various automatic nodule detection techniques employing advanced image processing tools. Image thresholding [27-73], region growing [74], clustering [37], [75-76], and template matching [77] are a few commonly found methods that have been used for nodule candidate detection. Armato *et al*. [73] used a multiple gray-level thresholding technique for candidate nodule detection. Messay *et al*. [27] have developed a CADe system based on an intensity thresholding approach for nodule detection. Dehmeshki *et al*. [74] introduced a 3-D region-growing algorithm combined with a fuzzy connectivity map for accurate nodule segmentation and detection. Ge *et al*. [75] have detected candidate nodule regions using an adaptive weighted k-means clustering algorithm. A Fuzzy Probabilistic C Mean (FPCM) based approach is used for lung structure segmentation and candidate generation by Gomathi *et al*. [76]. A Growing Neural Gas (GNG) clustering technique has been reported by Netto *et al*. [37] for lung nodule detection. Lee *et al*. [77] proposed a Genetic Algorithm Template Matching (GATM) based technique for nodule detection. The templates were designed by considering the Gaussian distribution pattern of lung nodules. Apart from that 3-D image processing techniques have been used successfully for nodule detection. Ozekes *et al*. [61] have proposed a 3-D template for nodular-like structure detection. Different 3-D features and their extraction techniques from lung CT images have been studied extensively in [78]. Recently, deep learning techniques have been introduced and applied successfully in the field of medical imaging owing to their self-learning capability [79]. Convolutional Neural Network (CNN) based deep learning models are the most popular ones and have given promising results. A complete survey based on different handcraft and recent CNN-based deep learning approaches with their pros and cons can be found in [25] for nodule detection.

3.2 Research Contributions

In this chapter, a new nodule detection system has been developed using the concept of GMM and morphological filter. Initially, the GMM model has been used to segment the internal structure of the lung region. Then a new morphological filter has been introduced using the opening operation. The proposed filter acts as a false positive reducer and can detect candidate nodules effectively from the HRCT image. Then different intensity and shape-based features have been used by this study for true nodule detection. It has been observed that owing to the introduction of a GMM-based segmentation technique combined with the morphological operation the system can detect lung nodules with higher sensitivity, specificity, and accuracy in HRCT images.

3.3 Nodule Detection Framework using Image Morphology and Gaussian Mixture Model

The proposed CADe system consists of five main modules for nodule detection, viz., 1) Pre-processing 2) Lung segmentation 3) Internal region segmentation 4) Nodule candidate detection 5) Feature extraction and nodule detection. Figure 3.1 shows the block diagram of the system. Different modules of the system have been described in detail in the next subsequent subsections.

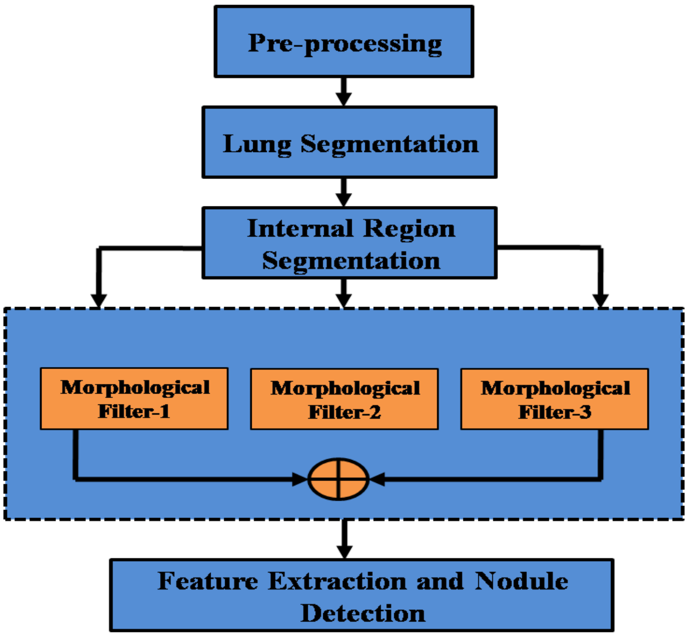

Figure 3.1: Block diagram representation of the proposed system.

3.3.1 Dataset Details

The research work has been performed on Lung Image Database Consortium and Image Database Resource Initiative (LIDC-IDRI) [20], which is the world's largest database, and consists of 1080 scans of 1010 patients. All the images are of size 512×512 and in DICOM (Digital Imaging and Communication in Medicine) format. The resolution of each image is 16-bit. In this work, a set of 40 nodules from 30 patients has been chosen from the LIDC-IDRI dataset.

3.3.2 Image Pre-processing

The objective of this module is to improve image quality by suppressing noise from the lung images. Impulse noise is commonly found in CT scans. A median filter exhibits excellent performance for impulse noise removal. Apart from that median filter can preserve image edges. Therefore, a median filter has been employed to enhance the input CT image and at the same time remove unwanted noise pixels from the CT slices.

3.3.3 Segmentation of Lung Region

In this stage, the left and right lungs have been extracted by removing tissues outside the lung parenchyma using an iterative threshold algorithm. The threshold value T^0 has been initialized by considering the average of the minimum and maximum intensity of the entire slice. This threshold value is refined iteratively to realize the effective lung region by eliminating other irrelevant objects of various intensities from the CT images. Let T^k is the threshold value obtained at step k and fg^k and bg^k are the corresponding mean gray level value of the foreground and background objects. Then the threshold value for the next iteration can be obtained as:

$$T^{k+1} = \frac{fg^k + bg^k}{2} \tag{3.1}$$

This iterative procedure has been continued until convergence i.e. $T^{k+1}=T^k$. Figure 3.2 shows the resultant lung segmentation image obtained using the iterative threshold algorithm.

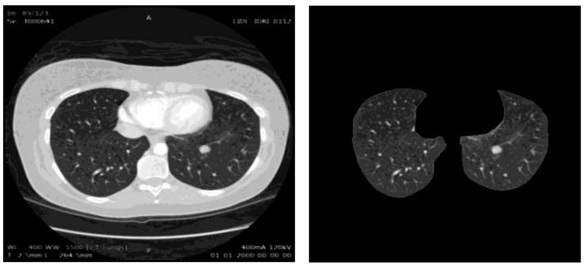

(a) **(b)**

Figure 3.2: Lung region segmentation: (a) Median filtered image (b) Lung segmented image.

3.3.4 Segmentation of Internal Lung Region

The lung region contains various objects of varying intensity and structural properties. Therefore, segmentation of different objects leads to nodule detection with a higher degree of accuracy. In this stage, internal high-density structures, e.g., blood vessels and nodules are segmented and isolated from the pulmonary parenchyma by employing Gaussian Mixture Model-based segmentation technique. A GMM model for each point x_p can be described as:

$$f\left(x_p\right) = \sum_{j=1}^{q} p_j \, Norm\left(x_p \mid \mu_j, \delta_j\right) \tag{3.2}$$

where, p_j is the probability of a pixel belonging to a class C_j , $j=1,2,3,\ldots q$, and $Norm\left(x_p \mid \mu_j, \delta_j\right)$ is the normal distribution with mean μ_j and variance δ_j. Therefore, a GMM can be described by considering three parameters, viz.,p_j, μ_j, and δ_j as $\psi = \left(p_1 \ldots p_q, \mu_1 \ldots \mu_q, \delta_1^2 \ldots \delta_q^2\right)$. Figure 3.3 shows internal lung regions, segmented using the GMM segmentation technique.

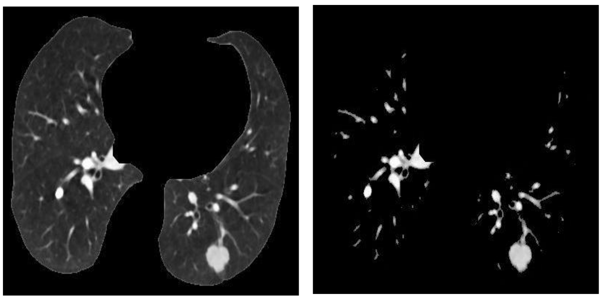

(a) **(b)**

Figure 3.3: Internal region segmentation: (a) lung image, (b) segmented image by GMM.

3.3.5 Nodule Candidate Detection

This stage finds the desired regions that are eligible to feed to a classifier for a decision. In this work, different false positives (FPs), e.g., vessels and bifurcation points have been removed from the scan with the help of morphological opening operation. In morphological image processing an opening operation is defined as the difference between a dilated image and an eroded image. In this study, three filters have been designed with Circular structuring element (SE) with different radii. The segmented image obtained by GMM is then processed with three morphological filters as shown in the block diagram (Figure 3.1). Finally, the filter images are fused to produce the candidate-detected image. The resultant image obtained by the proposed morphology filter is portrayed in Figure 3.4.

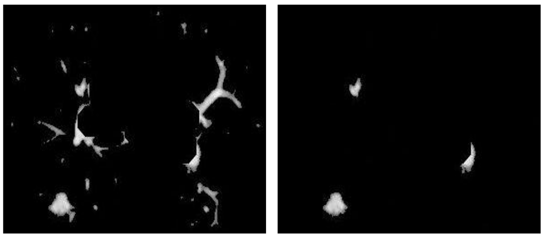

(a) **(b)**

Figure 3.4: Filter output: (a) region segmented image, (b) nodule candidate detected image.

3.3.6 Feature Extraction and Nodule Detection

In this stage, different relevant features have been computed from identified candidate nodule regions obtained in the previous stage for making a final decision on whether the candidate is nodule or non-nodule. Morphology and intensity-based features have been considered in this work. Four morphology features, viz., circularity, eccentricity, solidity, extent, and two intensity-based features, viz., maximum intensity and mean intensity have been studied for nodule detection. SVM classifier [71] with nonlinear Radial Basis Function (RBF) has been selected for true nodule detection.

3.4 Results and Discussion

The proposed framework has been tested on the LIDC-IDRI dataset. All the images are in DICOM format having dimensions of 512×512. A total of 60 nodules have been selected from 50 different patients for detection purposes. Initially, the lung CT images are filtered with the help of a 3×3 median filter for noise reduction. Then the left and right lungs are segmented by iterative threshold algorithm. Table 3.1 shows the lung segmentation result obtained by the system. An average Dice similarity coefficient of 0.9681 and Jaccard index (JI) of 0.9548 has been achieved by employing iterative threshold algorithm. After lung segmentation, internal regions are further segmented with the help of the GMM clustering algorithm. A total of 30 mixture components have been considered in this work for internal structure segmentation. The mean of mixture components has been used as the threshold value for internal brighter region segmentation. The segmented regions are then processed with a morphological opening filter for nodule candidate detection. Three filter-banks, viz., Filter_Bank-1 (FB_1), Filter_Bank-2 (FB_2), and Filter_Bank-3 (FB_3) with different size Structuring Elements (SEs) have been considered for candidate detection. Table 3.2 shows the different radii of SEs that have been considered for different filter bank designs. Circular shape SE has been used for this purpose.

Table 3.1: Lung segmentation result

Dataset	**Average Dice Score**	**Average Jaccard Index**
LIDC-IDRI	0.9681	0.9548

Table 3.2: Different filter banks with structuring elements

Filter Bank	**Selected SEs Radius**
FB_1	3,5,7
FB_2	5,7,9
FB_3	7,9,11

These filter banks are then processed on GMM-segmented images for candidate nodule detection. Table 3.3 shows the number of FPs obtained from the individual filter. It has been observed from Table 3.3 that FB_1 produces a maximum number of false positives. On the other hand, FB_2 produces a comparatively less number of FPs, and FB_3 produces a minimum number of FPs. Figure 3.5 shows nodule candidate detection output obtained by three different filter banks. In Figure 3.5 it is seen that FB_1 can detect true nodules (indicated by the red arrow) with more false positives whereas FB_2 detects true nodules with only two FPs. But FB_3 has missed the true nodule completely owing to the selection of large-sized SEs for filter design. Although FB_3 outputs substantially less number of FPs but it erases most of the true nodules. Therefore, in this study FB_2 has been considered for candidate nodule detection that can preserve true nodules with less number of false positives. The detected candidate regions obtained by FB_2 are then processed by the classifier for true nodule detection.

Table 3.3: False Positives produced by different filter banks

Filter Bank	Number of Slices	False Positives
FB_1	55	671
FB_2	55	134
FB_3	55	52

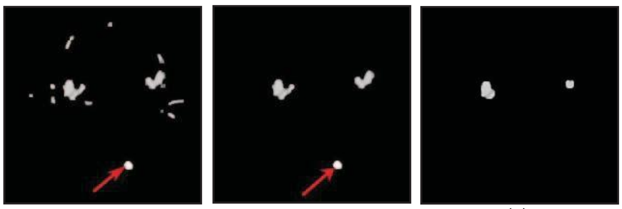

(a) **(b)** **(c)**

Figure 3.5: Different Filter_Bank output image on LIDC-IDRI dataset: (a) true nodule detected by FB_1, (b) true nodule detected by FB_2, (c) true nodule missed by FB_3.

In this work, the SVM-RBF classifier has been used for nodule identification. The performance of the proposed framework has been analyzed with the help of Sensitivity, Specificity, and Accuracy in publicly available LIDC-IDRI dataset. The expressions for different performance indices have been written in terms of True Positive (TP), False Positive (FP), True Negative (TN), and False Negative (FN) as follows:

$$Sensitivity = \frac{TP}{TP + FN} \tag{3.3}$$

True positive (TP) is the ROIs i.e. nodules correctly identified by the system. Whereas the False Negative (FN) value is the actual nodules missed out by the system. Specificity is also defined as the ratio, the same as Sensitivity but instead of using TP, a True negative (TN) value is used.

$$Specificity = \frac{TN}{TN + FP} \tag{3.4}$$

A True negative region is a non-nodule region correctly identified as non-nodules and a false positive (FP) is the non-nodule region that is incorrectly identified as nodules. Finally, the accuracy of the system is defined as follows:

$$Accuracy = \frac{TP + TN}{TP + FP + TN + FN} \tag{3.5}$$

The proposed framework has used SVM-RBF classifier for nodule detection and validated using k- fold cross-validation technique. The k value of 3, 5, and 10 has been chosen to demonstrate the system performance. Figure 3.6 shows the sensitivity, specificity, and accuracy of the proposed system for different k values. It has been observed from Figure 3.6 that the CADe system has obtained a maximum sensitivity, specificity, and accuracy of 89.77%, 86.92%, and 88.24% for a k value of 10. Therefore, in this work, a 10-fold cross-validation technique has been used by the proposed work for classifier training and testing. Results of the proposed methodology are tabulated in Table 3.4 and Table 3.5 respectively.

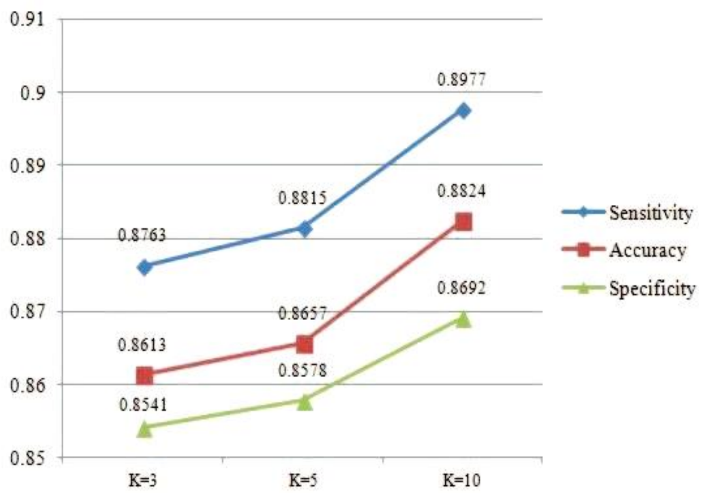

Figure 3.6: Performance of the CADe system for different values of k: (a) 3-fold cross-validation, (b) 5-fold cross-validation, (c) 10-fold cross-validation.

Table 3.4: Sensitivity specificity and accuracy of the CADe system

Dataset	Sensitivity (%)	Specificity (%)	Accuracy (%)
LIDC-IDRI	89.77	86.92	88.24

Table 3.5: Performance comparison of the CADe system with existing frameworks on LIDC-IDRI dataset

CADe Framework	Sensitivity (%)
Alilou *et al*. [80]	80
Lu *et al*. [81]	85.2
Wang *et al*. [82]	88
Proposed method	**89.77**

3.5 Summary

In this work, an automated CADe framework has been developed for nodule detection. GMM is used for different internal structures and nodule segmentation. A morphology filter based on morphological opening operation has been developed for vessel removal and nodule candidate detection. Different intensity and shape-based features have been used in this study for nodule detection. The reported framework has been tested and evaluated on the LIDC-IDRI dataset. A 10-fold cross-validation technique with the SVM classifier has been used by the system for accurate, unbiased training and testing. The system has achieved a sensitivity of 89.77%, a specificity of 86.92%, and an accuracy of 88.24% for nodule detection. Recently deep learning approaches are being used for nodule detection and classification. Therefore, in the future, works based on deep learning will be conducted for nodule detection and classification tasks.

- **Publication:**

Amitava Halder, Saptarshi Chatterjee and Debangshu Dey, "Morphological Filter Aided GMM Technique for Lung Nodule Detection", in *Proc. of 2020 IEEE Applied Signal Processing Conference (ASPCON),* Kolkata, 2020, pp. 198-202, doi: 10.1109/ASPCON49795.2020.9276715.

Chapter 4

Adaptive Morphology Aided Framework for Lung Nodule Segmentation and Detection

4.1 Background and Motivation

Lung cancer is one of the leading causes of death and fastest-growing cancer all over the world. According to a report [83] from WHO, lung cancer is the most frequently diagnosed cancer (11.6% of all cases) and is considered a major health problem all over the world. Lung cancer caused the highest death of 18.4% of the total cancer deaths worldwide as reported in [84]. In developing and developed countries it has been observed that lung cancer rank first in incidence for men [85]. ACS [5] in the United States compiles the most recent data on cancer incidence, mortality, and survival. In 2019, new lung cancer cases were 228150, and death from lung cancer 142670 was projected to occur in the United States as reported by ACS. The society also reported an estimate of 2,28820 new lung cancer cases and 1,35720 lung cancer deaths for the year 2020 in the United States. According to Radiologists/Experts, the primary reason behind this is the abnormal and uncontrolled growth of cells in lung tissue often called Pulmonary Nodule/Lung Nodule. The five-year survival rate of this disease is less than 18% and over half of the people die within one year of diagnosis owing to its poor prognosis [86]. Therefore, early detection of lung nodules and proper treatment planning can improve the 5-year survival rate significantly [87]. HRCT images are widely used image modality owing to enhance image resolution and non-invasiveness that is suitable for nodule detection, characterization [88], and diagnosis of other diseases, e.g., interstitial lung disease (ILD) [89]. A typical CT scanner produces a huge volume of CT slices that must be examined consciously for the manual detection of lung nodules by the radiologist. The task is time-consuming and the small, low-density nodules may be missed even by experienced radiologists owing to fatigue. Therefore, to mitigate this problem, Computer-aided detection and diagnosis systems using advanced image analysis techniques have been developed to help radiologists. The CAD systems can detect and classify nodules automatically from a series of CT slices and can a) improve the accuracy in diagnosis b) reduce exam evaluation time and c) assist in the early detection of cancer. Therefore, many researchers have proposed different state-of-the-art frameworks for accurate nodule detection, segmentation, and classification. Recent survey works towards nodule detection and classification are available in [16, 22-25]. A standard nodule detection framework consists of the following stages: (i) pre-processing (ii) lung segmentation (iii) nodule candidate detection and (iv) false-positive reduction. In the pre-processing stage, the Median filter [90-91], Gaussian filter [92-93], and Wiener filters[94] have been used by different authors for the removal of noise and to improve acquired image quality. After the pre-processing stage, the segmentation module is employed to extract the lung volume and remove all artefacts external to the lung regions. Lung segmentation is the essential step towards accurate nodule detection and characterization, as it removes irrelevant regions from the image and keeps the region of interest (ROI) for further processing. Lung segmentation based on thresholding [34, 47] and region growing [95-96] is the most commonly found method used by researchers. After lung segmentation, nodule candidate detection is the most important stage in the nodule detection framework. This stage identifies regions that are eligible to feed to the classifier. Different automated nodule candidate detection schemes have been introduced so far in the existing literature. Filter-based [47-48, 97], clustering-based [34], template-matching [98], model-based [99], wavelet [100], and fractal-based [101-102] approaches are a few of them. Choi *et al*. [47] used a multi-scale dot enhancement filter for candidate nodule detection. The proposed system has achieved a sensitivity of 97.5% with 6.76 FPs per scan. Jaffar *et al*. [48] employed a Hessian matrix applied in multi-scales for nodule candidate identification and achieved a sensitivity of 97.5% with 98.7% detection accuracy. Tan *et al*. [97] developed a CADe framework based on the divergence of normalized gradient (DNG) and selective enhancement filter. The work obtained a sensitivity of 87.5% with 4FPs/scan. Javaid *et al*. [34] applied the k-means clustering algorithm for potential nodule candidate detection. Overall sensitivity and accuracy of 91.65% and 96.22% with 3.19 FPs per case have been achieved by the researchers. El-Baz *et al*. [98] proposed a novel nodule detection framework based on template matching that follows the Gaussian distribution. A genetic algorithm (GA) has been used to identify the nodule candidate locations. The fitness of GA has been defined as a similarity score calculated from the normalized cross-correlation of the nodule image and template image. Researchers achieved a positive predictive value (PPV) of 89.9% for nodule candidate detection in a private dataset. Cascio *et al*. [99] introduced a model-based approach for nodule segmentation and detection. 3-D Mass–Spring Model (MSM) that uses spring forces and torques have been studied by researchers for accurate nodule segmentation. The framework has been evaluated on the LIDC dataset and obtained a sensitivity of 97% with 6.1FPs/CT and 88% with 2.5FPs/CT respectively. Wavelet plays an important role in texture-related feature extraction. As most of the nodules are irregular, therefore, wavelet-based features can be extracted for accurate nodule segmentation and detection. Ma *et al*. [100] proposed a CADe system using the 'Coiflet 1' wavelet. A sensitivity of 88.9% has been obtained by the system. Kravchenko *et al*. [101] used fractal dimension transformation-based features for nodule detection. Researchers have achieved a sensitivity of 88.97% with 3.3 FPs/scan and 91.03% with 2.8 FPs/scan using SVM and AdaBoost classifiers respectively. Veronica [103] proposed a nodule detection scheme based on an artificial neural network (ANN). The weights of the ANN have been optimized using the Oppositional based 'Ant Lion Optimization' (OALO) algorithm and achieved a sensitivity of 93.3% with the ELCAP dataset. An example of a sample lung HRCT image is portrayed in Figure 4.1.The corresponding lung nodule has been shown with proper labeling.

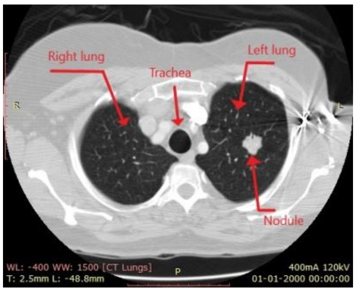

Figure 4.1: Original lung HRCT image marked by the radiologist (red arrow). Source: LIDC-IDRI.

4.2 Research Contributions

In this chapter, an adaptive mathematical morphology-aided filter has been introduced for accurate segmentation and further detection of lung nodules in HRCT images. The block diagram of the proposed framework has been shown in Figure 4.2.

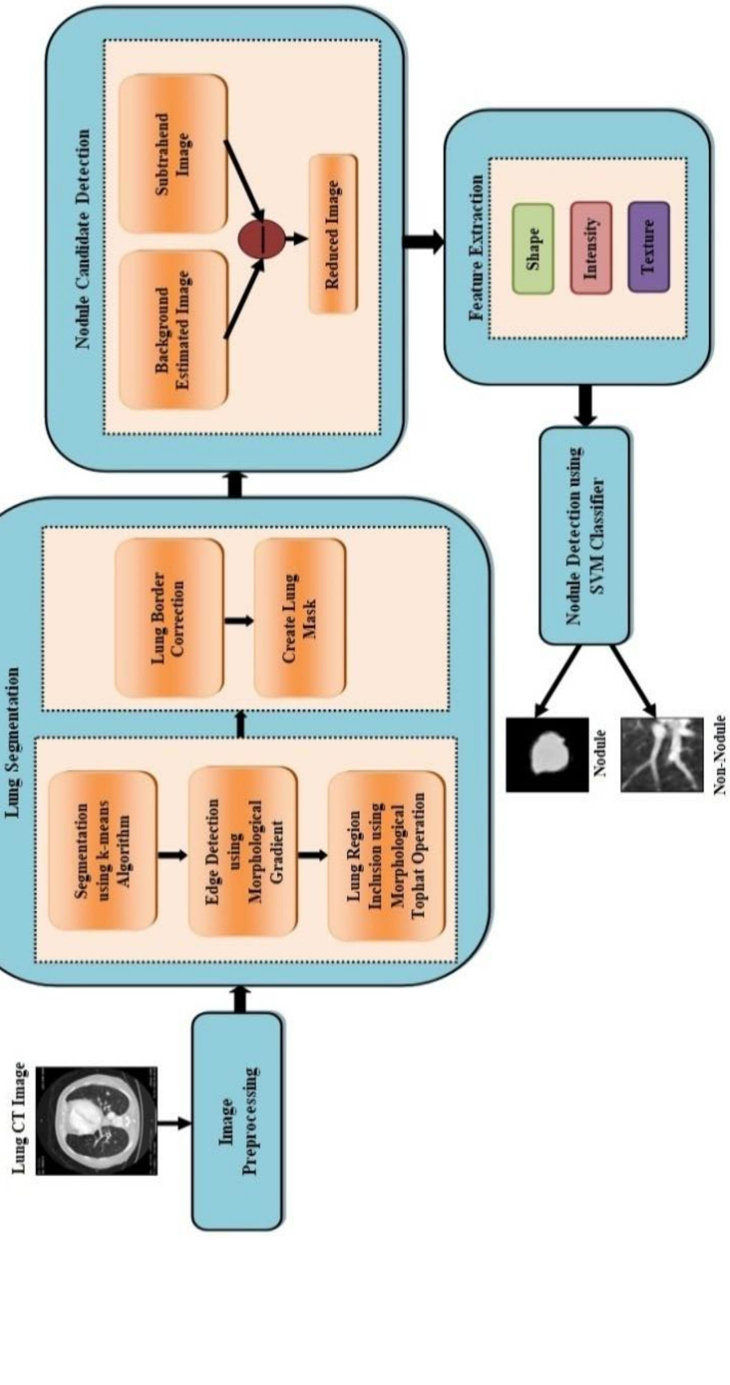

Figure 4.2: Block diagram representation of the proposed framework.

The major contributions of this reported work are as follows:

- **An improved lung segmentation algorithm is presented employing morphological techniques.**
- **Considering the morphological and deformable properties of the lung nodules, adaptive structuring elements have been introduced for the development of morphological filters.**
- **Grayscale adaptive morphological filters are developed for the segmentation and detection of large varieties of candidate nodules.**

Therefore, the development of this morphological technique by selecting the structuring element adaptively, depending on the morphological properties of the nodule is the major contribution of this work. The introduction of this reported technique has significantly improved the performance of nodule segmentation and detection, compared to the recently published state-of-the-art techniques.

4.3 Grayscale Morphology for Image Processing

Mathematical morphology is an effective image-processing methodology based on the algebra of non-linear operators acting on object shapes and is used for image segmentation, shape analysis, and texture analysis. Initially, the theory behind morphology was developed based on set theory. Since then, gray-level morphology-based techniques have been introduced with the help of umbra transform and later using the concept and notion of complete lattice theory. A grayscale image is defined as a scalar-valued function $\xi : D \subset \mathbb{N}_0 \to \mathbb{N}_0$ that can take any values within the range $R(\xi) \in \mathbb{N}_0[0, 255]$. A normalized grayscale image is defined as $\xi : D \subset \mathbb{R} \to \mathbb{R}$ where the image function range is $R(\xi) \in \mathbb{R}[0, 1]$. The image intensity value for a grayscale image is denoted as $\xi(\mathrm{Q})$ with point coordinate $Q = (\mathrm{q}_1\, \mathrm{q}_2)^T$ on a 2D Euclidian space. The concept of structuring element (SE) with certain geometrical patterns plays a vital role in accurate shape extraction from the image. The structuring elements (SEs) are translated over the image plane and different morphological operations have been performed for shape detection. In classical morphology the basic grayscale erosion and dilation operations are the two most fundamental operations and can be defined by following the notions of lattice theory as follows:

Let τ be the set of grayscale images with the domain $D \subset \mathbb{R}$,i.e., $\tau = \{\xi \mid \xi : D \to \mathbb{R}\}$. A complete lattice with partial order " $\leq$ " is then defined by $\xi \leq \eta \Leftrightarrow (\forall x \in D)\, \xi(x) \leq \eta(x)$ where $\xi, \eta \in \tau$. A lattice is said to be complete if all its subsets have both the infimum ($\wedge$) and supremum ($\vee$) values. Now, the basic morphological operations are given as:

Grayscale Erosion

$$[\varepsilon_S(\xi)](x) = \bigwedge_{y \in S_x} \xi(y), \;\; x \in D, \tag{4.1}$$

and Grayscale Dilation

$$[\delta_S(\xi)](x) = \bigvee_{y \in S^*_x} \xi(y), \quad x \in D, \tag{4.2}$$

where, S is the structuring element translated over the image ξ and S^* is the reflected or transposed structuring element, obtained by reflection of *S* through the origin. The grayscale *'Opening'* and *'Closing'* operations are defied with the help of grayscale *'Erosion'* and *'Dilation'* as follows:

Grayscale Opening

$$\alpha_S = \delta_S \circ \varepsilon_S, \tag{4.3}$$

Grayscale Closing

$$\beta_S = \varepsilon_S \circ \delta_S \tag{4.4}$$

In classical or conventional grayscale morphology the shape and size of the structuring element (*S*) is defined only once for the entire image and it can not be changed. Therefore, conventional grayscale morphological operations fail to capture the true shape variations of irregularly shaped objects. This is the main drawback of classical morphology.

4.4 Adaptive Grayscale Morphology: a cursory view

Adaptive Morphology is the generalization of the translation and the rigidity of the structuring element, where the shape and the orientation of the structuring element change according to the morphological features of the object. In morphological image processing, the selection of proper structuring elements is important for the accurate extraction of ROI. Adaptive structuring element (ASE) can change its shape and size by considering different image features, e.g., contrast, local curvature, the orientation of the ROI, the gradient magnitude, etc. Therefore, adaptive morphology can extract irregularly shaped objects more accurately with the help of adaptive structuring elements (ASEs) that have been considered for each pixel uniquely. The adaptation of structuring elements can be achieved with the help of location dependency [104] of SE in the image domain *D* or by considering the image content, e.g., morphological amoebas [105], region growing [106], elliptical adaptive structuring elements [107], etc. Nodule detection is a challenging task owing to the presence of elongated vessel structures (FPs). The lung nodule resembles an elliptically shaped structure in the CT slices. Therefore, in this work, adaptive structuring elements with elliptical shapes have been used for accurate candidate region extraction. An adaptive morphological image filter has been designed by considering elliptical shape adaptive structuring elements. The proposed filter can improve nodule detection accuracy by suppressing vessel-like structures significantly. Let $\mathrm{Q}=(\mathrm{q}_1\,\mathrm{q}_2)^T$ denote 2-D point coordinates for point *Q* in a grayscale image. Now for each pixel, $Q \in D(\xi)$ local structural variations in the input image are computed using second-order tensors given by:

$$T(Q) = \begin{pmatrix} T_{q_1\,q_1} & T_{q_1\,q_2} \\ T_{q_1\,q_2} & T_{q_2\,q_2} \end{pmatrix}(Q) = G_\sigma * (\nabla\xi(Q)\nabla^T\xi(Q)) \tag{4.5}$$

where $\xi(Q)$denotes the image intensity value for a point *Q*, $\nabla = (\frac{\delta}{\delta q_1}\frac{\delta}{\delta q_2})$ the first order derivative, and $G_\sigma$is Gaussian Kernel with standard deviation σ. The σ value is derived from the following equation:

$$\sigma = \frac{r_w}{\sqrt{2\ln 2}} \tag{4.6}$$

here, r_w is the filter bandwidth radius. Table 4.1 shows different relations between $\lambda_1(Q)$ and $\lambda_2(Q)$.

Table 4.1: Different conditions for the determination of different orientations

Relation	Comment
$\lambda_1 \approx \lambda_2 \gg 0$	Presence of edge crossing or point
$\lambda_1 \gg \lambda_2 \approx 0$	Presence of edge
$\lambda_1 \approx \lambda_2 \approx 0$	Absence of edge

According to Table 4.1, the relation ($\lambda_1 \gg \lambda_2 \approx 0$) provides information about the presence of an edge. Therefore, for each pixel Q the eigen values $\lambda_1(Q)$, $\lambda_2(Q)$ and the corresponding eigenvectors $\mathbf{e_1}(Q)$ and $\mathbf{e_2}(Q)$ that satisfy the inequality $\lambda_1 \gg \lambda_2 \approx 0$ have been chosen from the local structure tensor $T(Q)$. The eigenvector $\mathbf{e_1}(Q)$ represents the local dominant direction of variation in the image. Now, an Adaptive Elliptical Structuring Element (AESE) has been assigned to each point $Q \in D(\xi)$ that is created by capturing data variation surrounding that point. The SEs can change their shape and orientation by varying its three parameters, viz., semi-major axis a, semi-minor axis b, and orientation ψ .The axes $a(Q)$, $b(Q)$ of the adaptive SE for pixel Q are then obtained from the eigen values of $T(Q)$ by the following expressions:

$$a(Q) = \frac{\lambda_1(Q)}{\lambda_1(Q) + \lambda_2(Q)} \times M, \tag{4.7}$$

$$b(Q) = \frac{\lambda_2(Q)}{\lambda_1(Q) + \lambda_2(Q)} \times M \tag{4.8}$$

It is observed from equations (4.7) and (4.8) that the AESE will dynamically range from the maximum allowed semi-major axis length *M*, where there is a significant variation in the image ($\lambda_1 \gg \lambda_2 \approx 0$) to a disk of radius *M/2* where $\lambda_1 \approx \lambda_2$ i.e. with no dominant direction. The orientation of the adaptive structuring element has been computed from the eigen vector components as follows:

$$\psi(Q)=\begin{cases}\arctan\left(\dfrac{e_{2,q_2}(Q)}{e_{2,q_1}(Q)}\right), & e_{2,q_1}(Q)\neq 0,\\ \pi/2, & e_{2,q_1}(Q)=0\end{cases} \tag{4.9}$$

where, $e_{2,q_1}(Q)$ and $e_{2,q_2}(Q)$ are the components of the eigenvector $\mathbf{e_2}(Q)$. Figure 4.3 shows the parameters of the adaptive SE and their relation to the two eigenvectors $\mathbf{e_1}$ and $\mathbf{e_2}$ respectively.

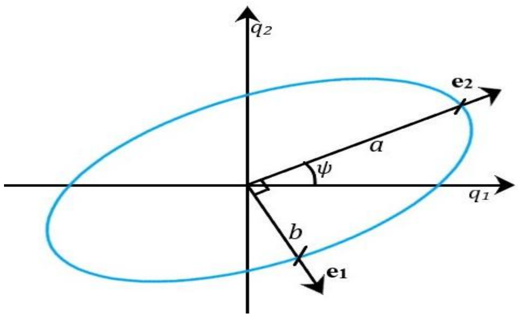

Figure 4.3: Different adaptive elliptical SE parameters showing relation to eigenvectors $\mathbf{e_1}$ and $\mathbf{e_2}$ [107].

After that, an elliptical neighbourhood surrounding the region $N_E(Q)$ has been obtained from the parameter values of $a(Q)$, $b(Q)$, and $\psi(Q)$ for each pixel $Q \in D(\xi)$ as given below:

$$N_E(Q)=E_Q(a(Q),b(\mathrm{Q}),\psi(Q)) \tag{4.10}$$

Here, E_Q is the associated adaptive ellipse for the pixel Q. The adaptive erosion (ε_{Adpt}) and dilation (δ_{Adpt}) operations are then defined over this neighbourhood region as:

Grayscale Adaptive Erosion

$$\varepsilon_{Adpt}(\xi)=\bigwedge_{P:P\in N_E(Q)}\xi(P)\ \forall Q\in D(\xi) \tag{4.11}$$

Grayscale Adaptive Dilation

$$\delta_{Adpt}(\xi) = \bigvee_{P:P\in N_E(Q)} \xi(P) \; \forall Q \in D(\xi) \tag{4.12}$$

The grayscale adaptive opening and closing operations are then defined as:

Grayscale Adaptive Opening

$$\alpha_{Adpt}(\xi) = (\delta_{Adpt} \circ \varepsilon_{Adpt})(\xi) \tag{4.13}$$

Grayscale Adaptive Closing

$$\beta_{Adpt}(\xi) = (\varepsilon_{Adpt} \circ \delta_{Adpt})(\xi) \tag{4.14}$$

Figure 4.4 shows different adaptive elliptical structuring elements (AESEs) with semi-major axis length L_a, semi-minor axis length L_b, and angle ψ in degree that are used for nodule candidate detection. It can be observed from Figure 4.4 that the elliptical-shaped structuring elements have different sizes and orientations that are formed by considering pixel intensity variations. Owing to the adaptive elliptical structure, the adaptive elliptical structuring element (AESE) can detect and preserve the nodule structure more precisely as compared to rigid SEs. In this study, AESE has given promising detection results by removing elongated vessel structures (FPs) significantly from the CT slices. This fact has been demonstrated in the results and discussion section elaborately by considering the proposed nodule candidate detection algorithm using this AESE as a structuring element.

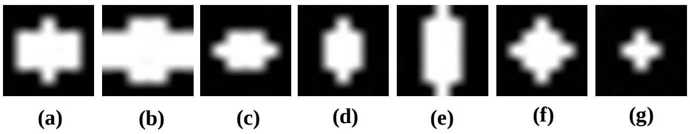

Figure 4.4: AESEs used by adaptive filter: (a) L_a =2.84, L_b=0.15, $\psi = -68.29$, (b) L_a =2.84, L_b=0.15, $\psi = -109.17$, (c) L_a =1.87, L_b=1.12, $\psi = -152.76$, (d) L_a =2.98, L_b=0.01, $\psi = -90.32$, (e) L_a =1.58, L_b=1.41, $\psi = -98.14$, (f) L_a =2.86, L_b=0.13, $\psi = -55.71$, (g) L_a =2.30, L_b=0.69, $\psi = -20.73$.

4.5 Adaptive Morphology Based Computer-Aided Detection (CADe) Model for Lung Nodule Segmentation and Detection

Nodule segmentation is an important step for accurate nodule detection. In this work, a new adaptive morphology-based segmentation technique (AMST) technique has been developed by introducing an adaptive bottom-hat (ABHT) filter for accurate segmentation and detection of nodule candidate regions. Initially, the lung regions have been segmented using k-means and morphological top-hat operation. After that, the proposed ABHT filter has been applied for vessel suppression and nodule candidate detection. A detail of each module has been described in the next subsequent sections.

4.5.1 Image Pre-Processing

In the pre-processing stage, an image filter has been used to enhance the lung CT images and remove noise for better visibility of nodule contours and locations. Owing to low radiation dose and changes in different scan parameters, e.g., exposure time, collimation/reconstructed slice thickness, detector efficiency, etc., lung CT images include noise artefact. The objective of this module is to suppress noise and enhance the image quality for further processing. Among various types of noises, the salt-and-pepper noise is the most common noise found in a CT slice. The median filter exhibits excellent noise-reduction capabilities in the presence of salt-and-pepper noise and at the same time, it preserves the sharp edges of an image. Therefore, in this work median filter has been used for image enhancement and noise removal.

4.5.2 Extraction of Thoracic Lung

This stage simplifies the nodule detection process by keeping only the pulmonary parenchyma through eliminating all artefacts outside the lung region. In this reported work, a thoracic lung segmentation technique (Algorithm 4.1) has been introduced using a k-means algorithm combined with image gradient and morphological top-hat operation. Employing the clustering technique, the pre-processed image (I_{pre}) has been segmented into foreground and background regions. The block diagram of the lung region segmentation algorithm has been elaborated in Figure 4.5. After the pre-processing stage the k-means clustering algorithm has been employed to segregate the foreground and background regions of the lung region.

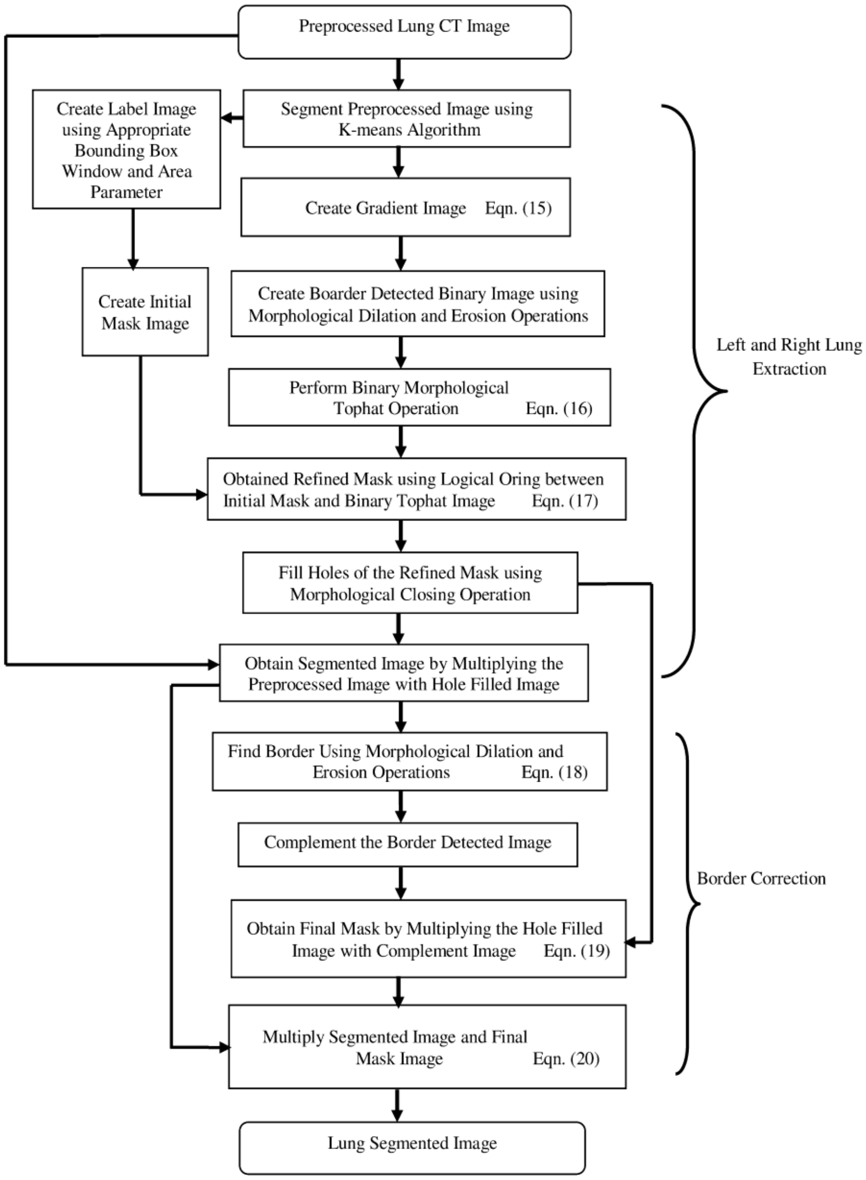

Figure 4.5: Block diagram of the lung segmentation algorithm (Algorithm 4.1).

The segmented left and right lungs image I_{seg} have been extracted from the corresponding segmented regions by considering the appropriate bounding box window and an area parameter. The label image obtained from the bounding box contains the desired lung regions. Image artefact, such as patient name, patient id, and different regions that are outside the desired bounding boxes are converted to the background. Then an initial mask image I_{m0} has been created from the I_{seg} image. After that, the pleural boundary and the boundaries of high-intensity regions, e.g., nodules and vessels have been detected with the help of morphological gradient operations. The gradient image I_{grad} obtained by:

$$I_{grad}(n) = \partial_S(I_{seg}(n)) - \varepsilon_S(I_{seg}(n)) \tag{4.15}$$

where, ∂_S and ε_S are the grayscale dilation and erosion operations, employing fixed circular structuring elements over the lung segmented image I_{seg}. A binary gradient image mask I_{bgrad} has been obtained by thresholding the resultant gradient image I_{grad}. Morphological binary top-hat operation has been performed on the border/contour detected image I_{bgrad} to include the high-intensity nodule and vessel regions. A binary black top-hat operation has been used in this study that can restrict its region inclusions without further extending the lung border and can re-include nodules that are located near the lung border regions and the regions surrounding the lung-hili. The black top-hat image has been obtained from I_{bgrad} as follows:

$$I_{btop\_hat}(n) = I_{bgrad}(n) \bullet S - I_{bgrad}(n) \tag{4.16}$$

here, $\bullet$ is the binary morphological closing operation with a structuring element S. After that, the initial mask image I_{m0} has been modified by:

$$I_{m1}(n) = I_{btop\_hat}(n) \, OR \, I_{m0}(n) \tag{4.17}$$

The image $I_{m1}(n)$ contains the mask of the left and right lung regions. A binary closing operation has been performed on image mask I_{m1} so that it can include juxtapleural nodules. The lung segmented image (I_{seg_1}) obtained by applying I_{m1} contains lung border. Therefore, a border correction technique has been introduced for lung border removal with the help of a border image obtained as:

$$I_{brdr}(n) = \partial_S(I_{seg\_1}(n)) - \varepsilon_S(I_{seg\_1}(n)) \tag{4.18}$$

Finally, the mask image I_{m1} has further been refined as follows:

$$I_{m\_final}(n) = (I_{brdr}(n))^{c} \times I_{m1}(n) \tag{4.19}$$

Here, c denotes the image complement operation and $\times$ denotes image multiplication operation. Finally, the lung image I_{lung} is obtained as:

$$I_{lung}(n) = I_{seg\_1}(n) \times I_{m\_final}(n) \tag{4.20}$$

The final lung segmented image I_{lung} was obtained by equation (4.20) contains the lung regions with no lung borders. Figure 4.6 shows images obtained from different stages of the lung segmentation algorithm.

4.5.3 Nodule Candidate Detection using Adaptive Morphological Filter

The performance of the CADe system is mostly affected by objects other than the object of interest, e.g., blood vessels present in CT slices. Reduction of false positives and at the same time selection of desired candidate nodules in an early stage can improve the sensitivity and detection accuracy of the CADe system by a considerable amount. In this stage, nodule candidate regions are detected with the help of adaptive morphological operations. A morphological image filter based on the adaptive bottom-hat transformation has been introduced that can detect irregular nodules from the CT slices with the help of adaptive SE. An adaptive SE can capture nodule irregularity by changing its shape and orientation. Therefore, the adaptive

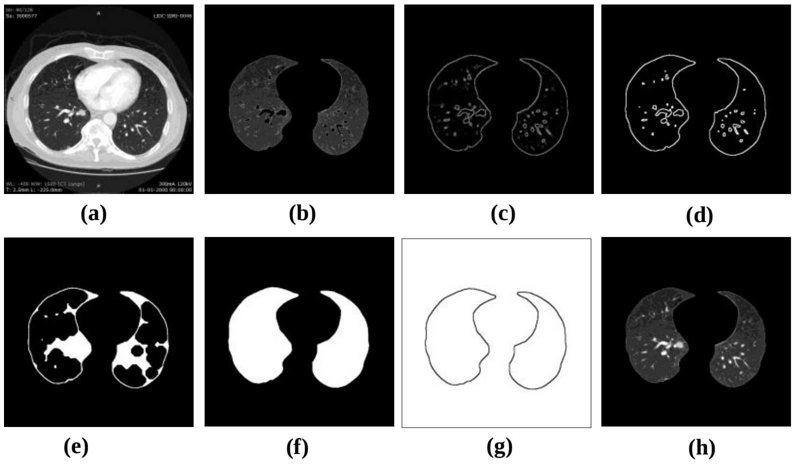

Figure 4.6: Lung segmentation outputs: (a) original lung CT image, (b) segmented image using k-means algorithm, (c) gradient image, (d) outlined image mask, (e) top-hat image mask, (f) lung mask image, (g) complement of border detected image, (h) border corrected lung segmented image.

bottom-hat (ABHT) filter can reduce more false positives by forming appropriate elliptical SE over the ROI under consideration and can improve the detection accuracy of CADe-based systems. The block diagram of the proposed adaptive morphological filter-based nodule candidate detection algorithm (Algorithm 4.2) has been given in Figure 4.7. A bottom-hat morphological operation is defined as the residual image of the morphological closed image and original image. In this study, an adaptive bottom-hat operation has been introduced. An adaptive bottom-hat transformation with the help of an adaptive structuring element can be defined as:

$$\gamma_{Adpt}(\xi(p)) = \varepsilon_{Adpt}(\partial_{Adpt}(\xi(p))) - \xi(p) \tag{4.21}$$

where, ε_{Adpt} and ∂_{Adpt} are the adaptive erosion and dilation operations over an image pixel $\xi(p)$. Adaptive bottom-hat transformation γ_{Adpt} can detect low-intensity regions and at the same time can preserve the appropriate structure of ROI with the help of adaptive structuring elements.

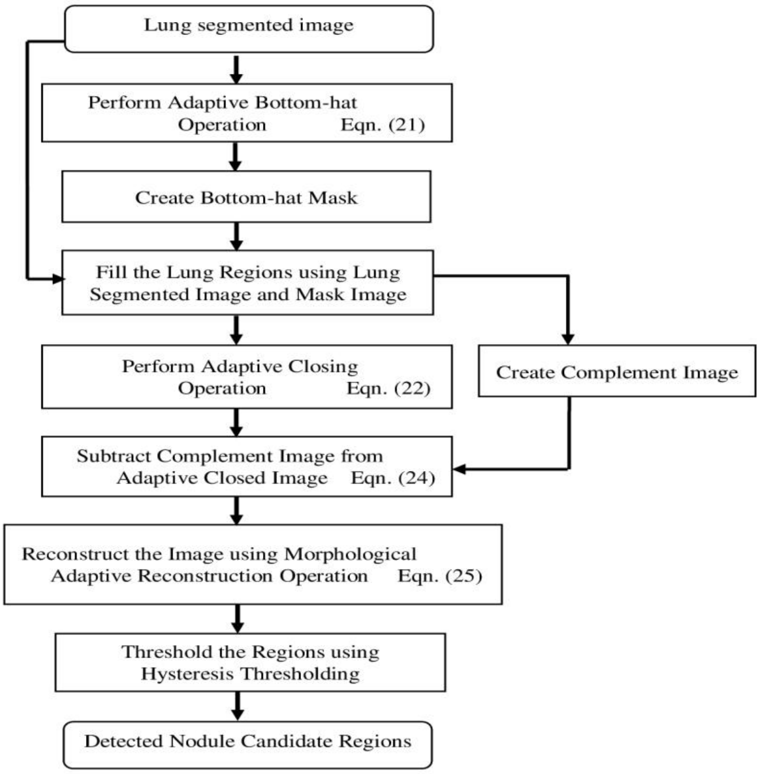

Figure 4.7: Block diagram of the nodule candidate detection algorithm (Algorithm4.2).

A lung nodule is a very small pathology and most of the time it is surrounded by relatively low-intensity lung regions. Hence, an adaptive bottom-hat operation can explore and extract lung tissues surrounding a nodule that in turn helps to detect nodules by extending the background regions. The appropriate low-density lung regions surrounding the nodule have been extracted by adaptive bottom-hat operation and the background mask has been created. A region-fill algorithm has been used to connect the newly explored lung backgrounds surrounding the nodule. After that, an adaptive closing operation has been used to remove small dark holes and to brighten small dark regions detected by adaptive bottom-hat operation previously. Next, the nodule candidate locations have been identified by introducing an adaptive *"Background Reduction"* technique. In this technique, the background reduction image has been obtained by subtracting the subtrahend image from the background estimate image. The background estimate image and subtrahend image are defined in equations (4.22) and (4.23) respectively.

$$\textit{Bacaground estimated image} = I_{bgimg}(p) = \varepsilon_{Adpt}(\gamma_{Adpt}(\xi(p))) \qquad (4.22)$$

and

$$\textit{Subtrahend image} = I_{simg}(p) = \oplus((\gamma_{Adpt}\xi((p)))^{C}) \qquad (4.23)$$

where, *c* and $\oplus$ denotes complement and regionfill operations over an image $\xi(p)$. Finally, the background-reduced image is obtained as:

$$\textit{Background reduced image} = I_{brimg}(p) = I_{bgimg}(p) - I_{simg}(p) \qquad (4.24)$$

The background reduced image $I_{brimg}(p)$ contains the candidate nodule location (x, y) along with very few FPs locations. The candidate nodules detected in I_{brimg} can't preserve the true shape of the actual candidate regions owing to the applications of different morphological operations. Hence, the background-reduced image I_{brimg} is then passed through a morphological reconstruction operation for shape restoration. Morphological reconstruction is the process of repeated dilation of an image called the Marker Image (I_{marker}), until the contour of the marker image fits under a second image, called the Mask Image (I_{mask}), where, $I_{marker} \subseteq I_{mask}$. In this work, the marker image is I_{brimg}, and the lung segmented image I_{lung} obtained from the output of the lung segmentation algorithm (Algorithm 4.1) has been used as mask image. The initial image is obtained as:

$$\omega_{\theta}^{(1)}(I_{brimg}) = \partial_{Adpt}(\omega^{(1)}(I_{brimg})) \cap I_{lung} \qquad (4.25)$$

where, ∂_{Adpt} and $\cap$ are the adaptive dilation and intersection operations respectively. The reconstructed image I_{recst} has been obtained iteratively by dilation of background reduced image I_{brimg} with respect to I_{lung} until

$$\omega_{\theta}^{(n+1)}(I_{brimg}) = \omega_{\theta}^{(n)}(I_{brimg}) \cdot \tag{4.26}$$

Considering the deformable shape and lower intensity variation along the boundary region of the object the choice of proper thresholding technique is very critical. In this work, hysteresis thresholding has been used to threshold each candidate nodule region that can incorporate the lower-intensity boundary pixels. In the hysteresis thresholding technique, two threshold values are chosen to separate the foreground from the background, viz., the lower threshold, and the upper threshold. The set of pixels with intensity values larger than the upper threshold value is set to '1' and at the same time, the set of pixels whose values lie between the higher and lower threshold, but are connected to a pixel whose value is above the higher threshold will also be marked ‘1’. After thresholding, candidate regions are further refined by computing area and elongation features. Finally, a nodule candidate list has been prepared by performing logical AND operation between the thresholded image and the lung segmented image. Different intermediate and final output images produced by the ABHT filter have been shown in Figure 4.8. The sensitivity of the ABHT filter has been discussed elaborately in the results and discussion section.

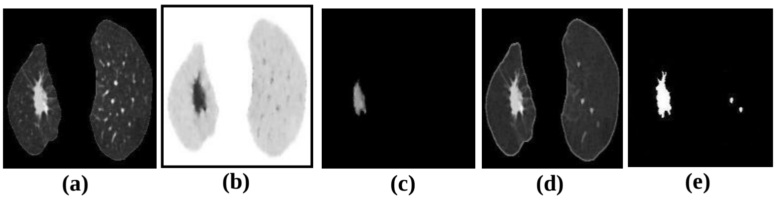

Figure 4.8: Adaptive bottomhat filter response: (a) original segmented image, (b) subtrahend image, (c) background reduced image, (d) reconstructed image, (e) thresholded nodule candidate.

4.5.4 Feature Extraction for Nodule Detection

In the feature extraction stage, different representative information is extracted from each of the candidate regions. After reducing the FPs from the CT image using the adaptive morphological filter, the extraction of appropriate features from the lung regions helps to identify the nodule candidates. Initially, shape and intensity-based features have been considered to separate nodules from elongated vessel structures. Different shape and intensity-based features, viz., perimeter, diameter, circularity, ellipticity, roundness, solidity, compactness, eccentricity, aspect ratio, extent, mean intensity, and maximum intensity have been extracted for nodule detection. Although the shape and intensity-based features give distinguishable values by capturing the morphological and gray-level distribution of lung nodules, they give low-performance indices of the CADe system. To overcome this limitation, texture variations of nodule and vessel regions are also analyzed by considering texture features. Finally, the 14 texture features have been combined with 10 shape-based and 2 intensity-based features to form a 26-dimensional feature vector that has been used by the proposed system. In this work different morphological features viz., circularity, ellipticity, roundness, compactness, eccentricity, solidity, aspect ratio, and extent have been used for nodule detection. The detail expression of each morphological feature has been elaborated in chapter-2. Apart from morphological features, in this work, different intensity and texture-based features have also been estimated for nodule detection as follows:

- **Max Intensity:** The maximum pixel gray level value within an ROI has been considered by this feature. Small nodules can be detected by using the maximum intensity feature because high-intensity blood vessels (FPs) are generally absent in the small nodule. It is observed that nodules have a lower maximum intensity value than vessels.
- **Mean Intensity:** This feature finds the average gray value of the pixels from the ROI. In general, nodules show a lower mean intensity value than vessels. Therefore, this feature can be used as a false positive reducer at the classifier level.
- **GLCM–based texture features:** The regional textural variation differentiates the nodule candidates from the false-positive objects. A gray-level co-occurrence matrix (GLCM) describes the spatial relationship of a pair of pixels by considering the frequency of occurrence within a region. The GLCM-based texture features have been used to compute different statistical texture features from each

of the detected candidate regions. A set of 14 features, viz., variance, contrast, inverse difference moment, angular second moment, sum variance, difference variance, sum average, entropy, sum entropy, difference entropy, correlation, maximal correlation coefficient, information measure of correlation I, information measure of correlation II have been computed by utilizing the GLCM matrix. The details of each of these texture-based features can be found in the work of Harralick *et al*. [108].

4.6 Results and Interpretation

The performance of the proposed CADe system has been validated through experiments using the CT images collected from two different resources, viz., LIDC-IDRI [20], and a private dataset collected from local patients in consultation with an expert radiologist. LIDC-IDRI is the world's largest repository and contains 1018 patients for lung cancer research. All the images are in DICOM format with a size of 512×512. The tube voltage and current used for data acquisition were 120kV (n=92), 135kV (n=7), 140kV (n=1), and 198 to 570mA respectively [44]. The annotated results of each patient were evaluated by four professional radiologists. They marked lesions based on nodule diameter as "nodule $<$3mm", "nodule $\geq$3mm" and "non-nodule $\geq$3mm" in the entire dataset. Different parameters, e.g., sphericity, lesion location, tumor type, etc. have been considered for the marking procedure. A total of 928 nodules marked by all four radiologists are available as ground truth (GT) images. Different nodules are also been labeled to indicate the degree of the risk factor of lung cancer and contain a value of '1' with most likely benign to a value of '5' indicating most likely malignant. In this work, a total of 95 CT scans have been selected randomly from LIDC-IDRI dataset for nodule detection. The scans consist of 200 nodules with a diameter ranging from 8 mm to 30 mm have been considered in this work. Figure 4.9 illustrated the annotated number of nodules according to their diameter range of 8-30 mm in the LIDC-IDRI dataset. To carry out the research work, 24 numbers of patient data have been collected from Theism Ultrasound Centre, Kolkata, India. The CT scans have been acquired using a Siemens Somatom Spirit scanner with a tube voltage of 130 KV, tube current of 100 mA, and rotation time of 1.0 Sec. The slice thickness varies in the range of 1-5 mm with a permitted Field Of View (FOV) of 300 mm having been used for image acquisition. A total number of 50 nodules in the diameter range of 8-30 mm that are properly marked by an expert radiologist have been considered for performance evaluation of the proposed

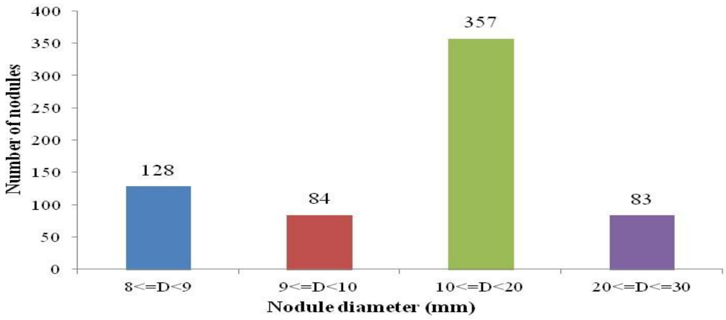

Figure 4.9: Histogram representation of the nodule diameter (8-30mm) distribution in the LIDC-IDRI dataset.

CADe system. The validation of this proposed framework has been done by investigating two aspects, viz., Detection Accuracy (DA), and Segmentation Accuracy (SA). Initially, a 3×3 median filter has been used for noise removal from the lung CT image. Then the lung region is segmented using the k-means algorithm and morphological binary top-hat operation. The number of clusters is set to 2 for the foreground and background partitioning of the image. After that, lung regions are selected from the segmented image by considering an appropriate bounding box of size 470×470. The regions that have an area greater than 1000 and are located within the minimum and maximum row locations of 40 and 470 are selected as lung regions. All the values are chosen experimentally. After lung segmentation, adaptive morphology-based operations, e.g., adaptive erosion, dilation, closing, and bottom-hat operations have been studied for ABHT filter design. An adaptive SE with a window size of 7×7 (M=3) has been considered throughout the work. The robustness of the proposed ABHT filter is demonstrated by comparing the response of the filter with the conventional bottom-hat filter. Figure 4.10 has reflected the number of false positives generated by employing the adaptive and non-adaptive filters applied over 4 groups each containing 50 CT slices. It can be observed from Figure 4.10 that the ABHT filter can reduce more false positives than the conventional non-adaptive filter. The primary objective of this work is to reduce FPs from HRCT images and consequently detect a wide range of lung nodules with a higher degree of specificity, sensitivity, and accuracy.

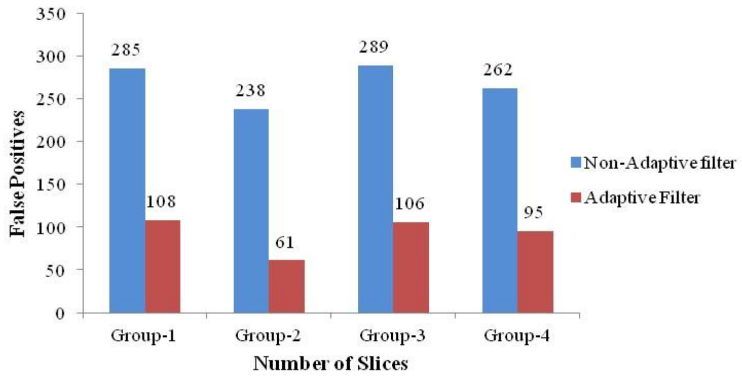

Figure 4.10: False positive response obtained by (a) Non-Adaptive, and (b) Adaptive filter on LIDC-IDRI dataset.

The Detection Rate (Sensitivity) of the proposed ABHT filter has been evaluated over different nodules with varying shapes and sizes. The dataset has been partitioned into different segments according to the nodule diameter (in mm). Tables 4.2 and 4.3 show the sensitivity of the ABHT filter by keeping the percentage of true nodules as candidate regions for further processing.

Table 4.2: Sensitivity of ABHT filter on LIDC-IDRI dataset

Gr. No.	**Nodule Diameter (D) (in mm)**	**Number of Nodule**	**#Nodule Detected by ABHT Filter**	**Sensitivity (%)**
Gr-1.	$8 \leq D < 9$	50	42	84
Gr.-2.	$9 \leq D < 10$	50	45	90
Gr.-3.	$10 \leq D < 20$	50	49	98
Gr.-4.	$20 \leq D \leq 30$	50	50	100

Table 4.3: Sensitivity of ABHT filter on a private dataset

Gr. No.	**Nodule Diameter (D) (in mm)**	**Number of Nodule**	**#Nodule Detected by ABHT Filter**	**Sensitivity (%)**
Gr-1.	$8 \leq D < 10$	20	16	80
Gr.-2.	$10 \leq D < 30$	30	28	93.33

It is observed from Table 4.2 that the overall detection rate is above 95% for nodules having a diameter greater than 10 mm. The detection rate is less than 95% for sub-centimetre (<10 mm) nodules. The proposed system is unable to detect the small diameter nodules having low intensity. It is observed from Table 4.3 that the detection sensitivity of ABHT is lower in the private dataset owing to different scan parameter settings of the CT scanner. Figure 4.11 depicted that the ABHT filter produces only 1.85 FPs/slice as compared to the other four filters, viz., Multi-scale Gaussian [109], 3-D blob [110], Cylinder [65], and Non-Adaptive filter. False-positive response images using adaptive and non-adaptive filters have been shown in Figure 4.12.

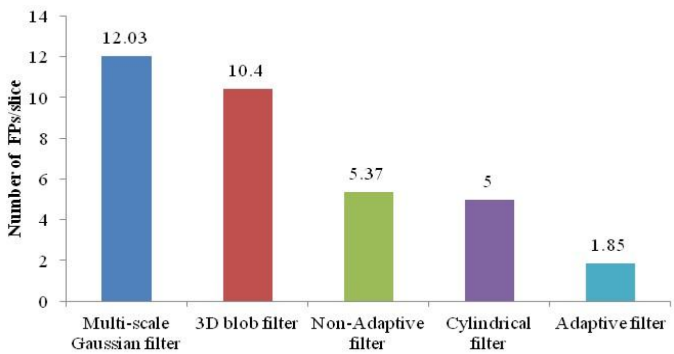

Figure 4.11: Average false-positive response per slice obtained by five different filters applied on LIDC-IDRI dataset: (a) Multi-scale Gaussian filter [109], (b) 3-D blob filter [110], (c) Non-Adaptive filter, (d) Cylinder filter [65], and (e) Proposed Adaptive filter.

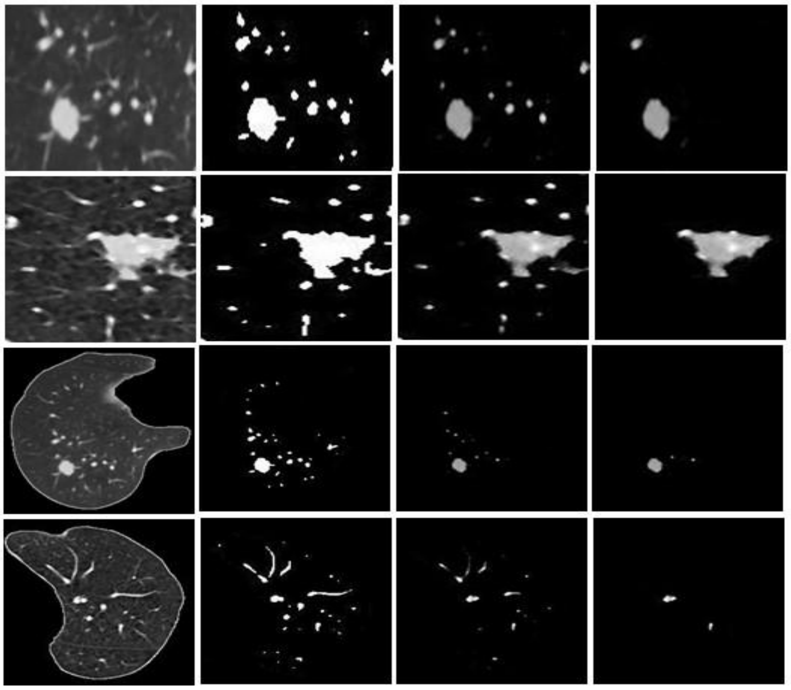

(a) (b) (c) (d)

Figure 4.12: False positive response image by different filters: (a) original lung segmented CT image with FPs, (b) Hysterian thresholded image, (c) removed FPs by Non-adaptive morphological filter, (d) removed FPs by Adaptive Morphological filter.

4.6.1 Lung and Nodule Segmentation Performance of the System

After that, the segmentation accuracy of the proposed framework has been investigated by considering two aspects, viz., lung segmentation (Figure 4.13) and nodule segmentation (Figure 4.14). In this work validation of the segmentation performance has been done by measuring five different quantitative evaluation criteria, viz., Dice Similarity Coefficient (DSC), Jaccard index (JI), Sensitivity (Sen), Specificity (Spec) and Accuracy (Acc). The expressions for Sensitivity, Specificity, and Accuracy have already been introduced in chapter-3. The expressions for DSC and JI have been written below. The value of DSC and JI ranges from 0 to 1 where '0' indicates no overlap between the Ground Truth (GT_{Im}) and Automatically Segmented (AS_{Im}) images and '1' indicates complete overlapping. The Dice Similarity Coefficient (DSC) and Jaccard index (JI) are expressed as follows:

$$DSC = \frac{2|AS_{Im} \cap GT_{Im}|}{|AS_{Im}|+|GT_{Im}|} \tag{4.27}$$

$$JI = \frac{|AS_{Im} \cap GT_{Im}|}{|AS_{Im} \cup GT_{Im}|} \tag{4.28}$$

The lung segmentation and nodule segmentation results obtained from LIDC-IDRI and private dataset are portrayed in Table 4.4 and Table 4.5 respectively.

Table 4.4: Lung and nodule segmentation performance of the system on the LIDC-IDRI dataset

Region of Interest	**Number of ROIs**	**Segmentation Performance Indices**					
		Values	**DSC**	**JI**	**Sen. (%)**	**Spec. (%)**	**Acc. (%)**
Lung	50	Min	0.9433	0.9456	96.83	95.56	96.13
		Max	0.9919	0.9840	98.89	97.22	98.27
		Avg	0.9872	0.9780	98.14	96.88	96.92
Nodule diameter greater than 10 mm	20	Min	0.8854	0.8639	98.23	96.34	97.12
		Max	0.9732	0.9355	100	99.68	99.76
		Avg	0.9538	0.9126	99.13	97.62	98.45
Nodule diameter between 8-10 mm	20	Min	0.8467	0.8217	96.89	94.46	95.13
		Max	0.9589	0.9172	99.76	97.28	97.82
		Avg	0.9453	0.8934	97.88	95.33	96.26

Table 4.5: Lung and nodule segmentation performance of the system on private dataset

Region of Interest	**Number of ROIs**	**Segmentation Performance Indices**					
		Values	**DSC**	**JI**	**Sen. (%)**	**Spec. (%)**	**Acc. (%)**
Lung	50	Min	0.9137	0.8953	96.72	94.56	95.21
		Max	0.9713	0.9625	97.31	96.15	97.11
		Avg	0.9543	0.9482	96.99	95.37	96.23
Nodule diameter greater than 10 mm	20	Min	0.8289	0.8324	97.44	94.93	96.16
		Max	0.9388	0.9076	98.81	96.72	97.88
		Avg	0.9157	0.8823	97.45	95.88	96.69
Nodule diameter between 8-10 mm	20	Min	0.8786	0.7989	94.95	93.10	94.22
		Max	0.9334	0.8961	97.12	95.91	96.97
		Avg	0.9089	0.8845	95.93	93.54	94.61

Figure 4.13 shows different segmented lung regions obtained by the proposed framework. The nodule segmentation results are shown in Figure 4.14.The variations in obtained nodule segmentation results from the ground truth nodule have been shown by a different colour in Figure 4.14 (d) and the performance indices have been mentioned in Figure 4.14 (e).

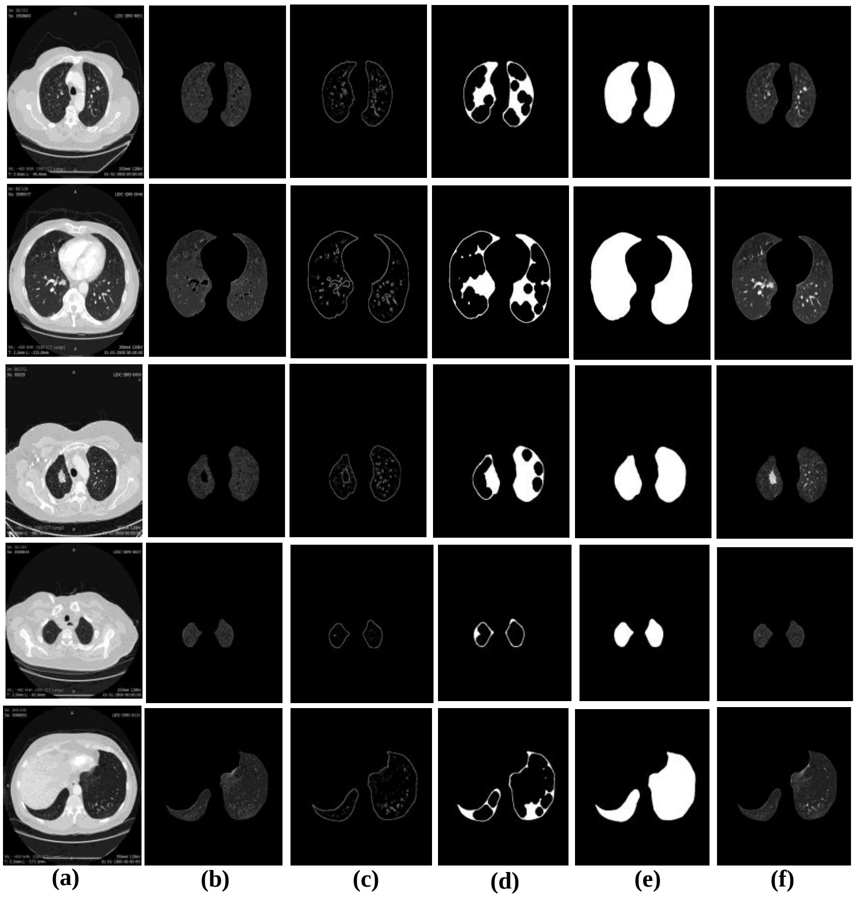

Figure 4.13: Lung volume segmentation: (a) original lung CT image, (b) lung segmentation using K-means algorithm, (c) gradient image, (d) binary tophat image, (e) final lung mask, (f) segmented lung image.

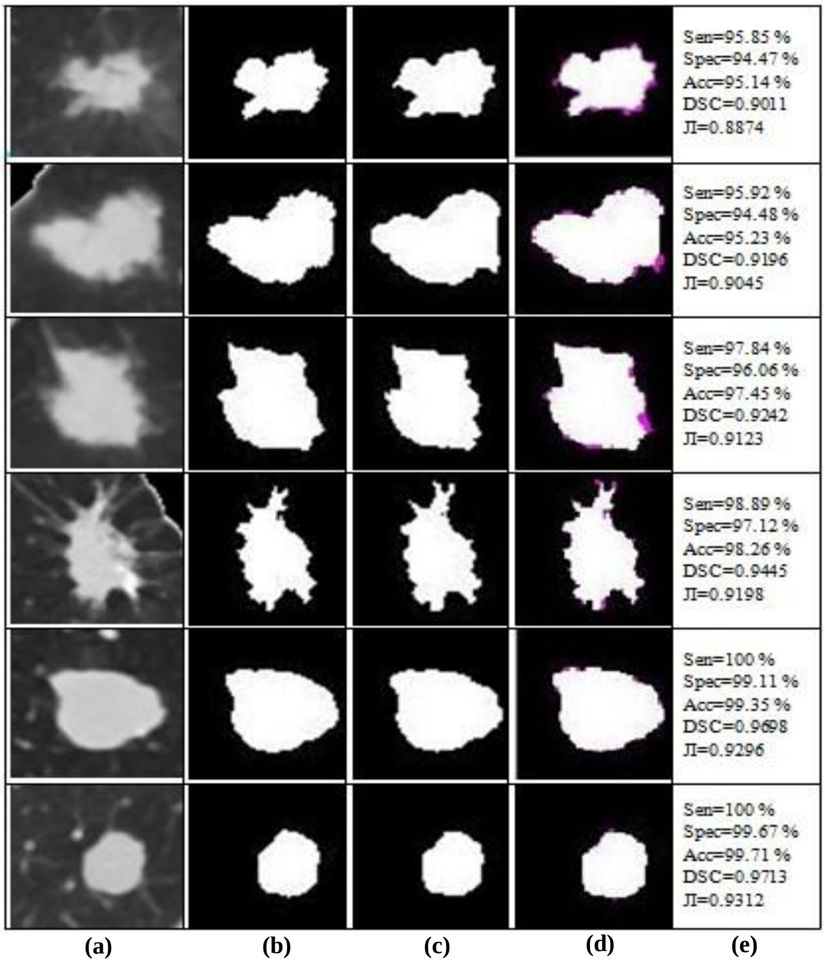

Figure 4.14: Nodule segmentation: (a) original nodule image, (b) ground truth nodule, (c) segmented nodule by the proposed CADe system, (d) nodule similarity measured image, (e) nodule segmentation performance indices.

4.6.2 Nodule Detection Performance of the System

In this study, the SVM classifier with radial basis function (RBF) kernel has been used for nodule detection. The weight and bias of SVM have been learned by computing different features from the training nodule dataset. For a d dimensional feature space and the training dataset $TS = (x_1, y_1), \ldots\ldots\ldots, (x_n, y_n)$, (where $x_n \in d$ with class label $y_n \in \{+1, -1\}$, +1 label denotes a nodule and –1 to a non-nodule), the decision boundary of the SVM classifier is given by $g(x) = \text{sgn}\left(\sum_{i=1}^{n} y_i \,\omega_i * Ker(x, x_i) + \gamma^*\right)$. Here, $Ker(x, x_i)$ is the kernel function $\gamma \in R$ and ω ω is constrained defined as follows: $0 \le \omega_i \le P^+$, for $y_i = +1$, and $0 \le \omega_i \le P^-$ for $y_i = -1$. Where P^+ and P^- are penalties for positive and negative class respectively. The SVM classifier has been trained using a ten-fold cross-validation technique. Shape, Intensity, and Texture features described in subsection 4.5.4 have been used for nodule recognition. To analyse the effectiveness of the chosen features, different combinations of features have been used for nodule detection. The performance of the nodule detection module has been verified from the estimated performance indices as sensitivity, specificity, and accuracy. Variation of the performance metrics depending on the feature set has been depicted in Figure 4.15. It has been observed from Figure 4.15 that the proposed system gives promising performance when texture features have been combined with shape and intensity features.

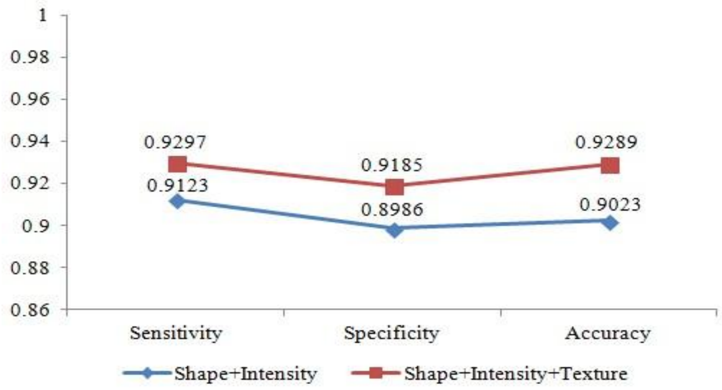

(a)

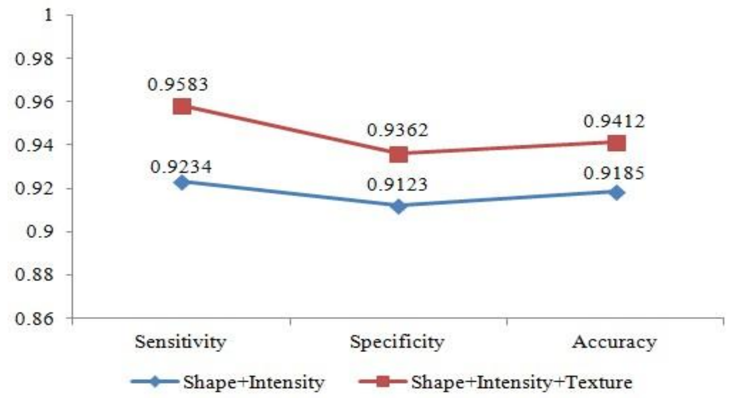

(b)

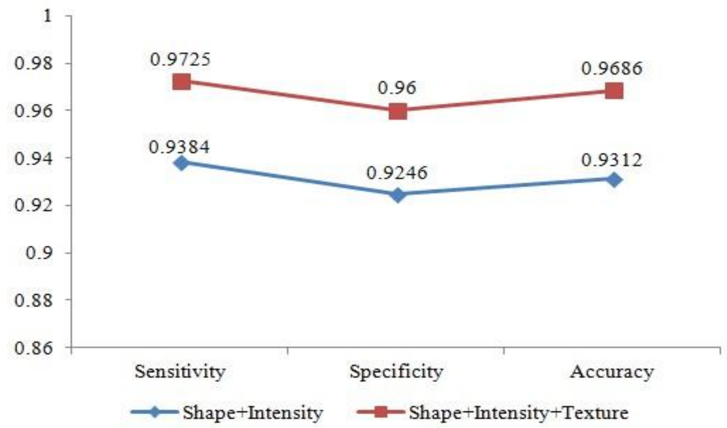

(c)

Figure 4.15: Sensitivity, Specificity, and Accuracy of the CADe system on LIDC-IDRI dataset by considering texture features for nodule diameter (D): (a) $8 \leq D < 10$, (b) $10 \leq D < 20$, (c) $20 \leq D \leq 30$.

The performance of the nodule detection technique has been validated on LIDC-IDRI dataset and a private dataset. The entire LIDC-IDRI dataset and private dataset have been categorized into four and two groups respectively according to the diameter of the nodules as per the annotation made by the experts. The performance of the proposed system for the detection of nodules of different diameters has been estimated by sensitivity, specificity, and accuracy as tabulated in Table 4.6 for the LIDC-IDRI dataset and Table 4.7 for the private dataset. It can be observed from Table 4.6 that a minimum sensitivity value of 92.90% has been achieved for group-1 nodules (diameter of $8 \leq D < 9$) and a maximum detection sensitivity of 97.25% has been achieved by the system for the group-4 nodules (diameter of $20 \leq D \leq 30$). The group-wise performance analysis has also been tabulated in table 4.7 on a private dataset. Table 4.8 shows the nodule detection performance comparison results of the proposed system with recent state-of-the-art CADe systems. Dolejsi *et al*. [109] used a multi-scale Gaussian filter for initial nodule candidate detection. Authors have used different features based on shape, intensity, covariance matrix, and Hessian matrix for true nodule detection and achieved a sensitivity of 89.62% on the LIDC dataset. Teramoto *et al*. [65] introduced a cylindrical nodule-enhancement filter for candidate nodule detection. A sensitivity of 80% with 4.2 FPs/scan has been achieved by the researchers. Santos *et al*. [62] proposed a CADe framework using Gaussian mixture models and obtained 80.50% sensitivity with 1.17 FPs/scan. Wang *et al*. [111] detected candidate nodules using Chan-Vese (CV) model and obtained a sensitivity of 88% with 4 FPs/scan. Gong *et al*. [44] introduced a CADe system using a template-matching technique. Researchers have achieved a detection sensitivity of 90.24% with 4.54 FPs/scan. Zhang *et al*. [112] proposed a CADe system by introducing a new feature named Voxel Removal Rate (VRR) for nodule detection. The proposed system obtained a detection sensitivity of 89.3% with 2.1 FPs/scan. From Table 4.8, it is observed that the proposed adaptive morphology-based segmentation technique (AMST) has detected wide varieties of lung nodules with improved performance indices in comparison with the recently published works.

Table 4.6: The nodule detection performance of the CADe system on the LIDC-IDRI dataset

Gr. No.	**Nodule Diameter (D) (in mm)**	**Sensitivity (%)**	**Specificity (%)**	**Accuracy (%)**
Gr.-1.	$8 \le D < 9$	92.90	91.33	92.86 with 2.3 FPs/scan
Gr.-2.	$9 \le D < 10$	93.55	92.86	93.27 with 1.9 FPs/scan
Gr.-3.	$10 \le D < 20$	95.83	93.62	94.12 with 1.6 FPs/scan
Gr.-4.	$20 \le D \le 30$	97.25	96.00	96.86 with 1.4 FPs/scan

Table 4.7: Nodule detection performance of the CADe system on a private dataset

Gr. No.	**Nodule Diameter (D) (in mm)**	**Sensitivity (%)**	**Specificity (%)**	**Accuracy (%)**
Gr.-1.	$8 \le D < 10$	89.93	88.63	90.86 with 3.8 FPs/scan
Gr.-2.	$10 \le D < 30$	93.74	91.52	93.12 with 3.6 FPs/scan

Table 4.8: Nodule detection performance comparison of the proposed CADe system with other state-of-art systems applying to the LIDC-IDRI dataset

CADe Systems	**Number of cases**	**Sensitivity (%)**	**FPs/scan**
Dolejsi *et al*. [109]	38 scans 202 nodules	89.62	——
Teramoto *et al*. [65]	84 scans 103 nodules	80	4.2
Santos *et al*.[62]	140 scans 260 nodules	80.50	1.17
Wang *et al*. [111]	103 scans 127 nodules	88	4
Gong *et al*.[44]	100 scans 302 nodules	90.24	4.54
Zhang *et al*. [112]	71 scans 168 nodules	89.3	2.1
Proposed CADe system	95 scans 200 nodules	**94.88**	**1.8**

4.6.3 Discussion

It has been observed that the developed nodule detection framework outperforms the existing state-of-the-art methods both qualitatively and quantitatively. The developed method has been implemented using the concept of adaptive morphology. The structural variations of lung nodules have been captured accurately by varying the shape of the structuring element. The proposed adaptive bottom-hat transformation-based morphological filter can remove vessel-like structures from the HRCT image. The adaptive SE can capture nodule irregularity by changing its shape and orientation. Thus the proposed adaptive bottom-hat (ABHT) filter can reduce more false positives with the help of appropriate elliptical SE over the ROI under consideration and can improve the detection accuracy of CADe-based systems. The proposed ABHT filter produces only 1.85 FPs/slice as compared to the other four filters, viz., Multi-scale Gaussian [109] , 3-D blob [110], Cylinder [65], and Non-Adaptive filter. Therefore, with the help of the ABHT filter the proposed CADe system has obtained the highest nodule detection accuracy of 94.27%with 1.8 FPs/scan on LIDC-IDRI dataset and 92.83% with 3.2 FPs/scan on a private dataset.

4.7 Summary

In this work, an adaptive morphology-based CADe system has been introduced for the detection and segmentation of lung nodules from CT images. In this work, the structuring elements have been considered adaptively according to the morphological properties of the object of interest. Employing the adaptive structuring element, adaptive morphological techniques have been introduced for the development of an adaptive morphological filter. The adaptive morphology-based nodule detection technique is introduced to segment wide varieties of nodules. The proposed framework has obtained sensitivity values varying between 92.90% to 97.25%, specificity values varying between 91.33% to 96.00%, and accuracy values varying between 92.86% to 96.86% on LIDC-IDRI dataset. Similarly, the system obtained sensitivity values vary between 89.93% to 93.74%, specificity values vary between 88.63% to 91.52%, and accuracy values vary between 90.86% to 93.12% for a private dataset. The system can detect different isolated, irregular, and some small juxta-pleural nodules with a diameter between 8-30 mm. In this work, shape, intensity, and texture-based features have been used to differentiate nodules from other non-nodule regions. SVM classifier with RBF kernel function has been used for nodule detection. However, the proposed framework has not obtained a significant segmentation and detection performance for Juxta-Vascular and small low-density nodules owing to the complex structure and low-intensity variation. Considerable performance indices have been achieved by the proposed indigenous adaptive morphology-based nodule segmentation and detection system that can be considered as a second opinion for the accurate detection of lung nodule at an early stage.

• Publication:

Amitava Halder, Saptarshi Chatterjee, Debangshu Dey, Surajit Kole and Sugata Munshi, "An Adaptive Morphology Based Segmentation Technique for Lung Nodule Detection in Thoracic CT Image," in *Computer Methods and Programs in Biomedicine, Elsevier,* (Impact Factor: 6.10), vol. 197, 105720, Dec. 2020, doi:10.1016/j.cmpb.2020. 105720.

Chapter 5

An Integrated Deep Learning System for Lung Nodule Segmentation and Characterization

5.1 Background and Motivation

Lung cancer has been identified as a major threat to human health that remains the leading cause of cancer-related deaths all over the world. It is the most common cancer with the highest mortality rate of 18.4% of the entire cancer population, as reported by GLOBOCAN in 2018 [81]. According to the report of the WHO) [1], in the year 2020, 1.80 million deaths were found worldwide. In 2022, the ACS [5] estimated the deaths of about 130,180 people inthe United States. Histopathologically, lung cancers can be categorized as non-small cell carcinoma (NSCLC) and small cell lung carcinoma (SCLC). NSCLC is a more common subtype and contributes 80%, whereas SCLC is a relatively uncommon subtype and accounts for 20% of total lung cancer cases all over the world [113]. It has been seen that about 70% of lung cancer patients are diagnosed with advanced stages [114-115]. Therefore, early-stage detection of this disease by routine check-ups is of utmost importance to decrease the lung cancer mortality rate. Medical imaging devices with different image modalities, e.g., chest X-ray, HRCT images, etc., can be used for accurate nodule detection. Among them, HRCT images are the most popular and preferred image modality due to their high resolution. A reduction of 20% in mortality rate is possible if HRCT scan images are used rather than conventional chest X-rays [19]. Figure 5.1 (a) and (b) show different benign and malignant HRCT nodule images that are taken from LIDC-IDRI [20] dataset.

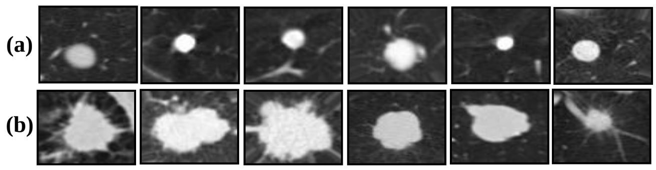

Figure 5.1: HRCT nodule images collected from LIDC-IDRI dataset: (a) benign, (b) malignant.

It can be observed from Figure 5.1 that the nodules are visible prominently in the HRCT image modality. Apart from advancements in image acquisition techniques, different image processing, and pattern recognition techniques are in use for accurate nodule detection, segmentation, and characterization. The systems developed by the researchers can be used as a second opinion for radiologists and doctors. For this, traditional machine learning (ML)-based systems are invented for automatic nodule detection and characterization. Recently deep learning -based frameworks have emphasized their automatic feature extraction capability. The newly invented systems can detect and characterize nodules with higher performance indices. Among different DL-based systems, the frameworks based on CNN are the most used architecture for their simplicity. In literature, different frameworks e.g., VGG [116], AlexNet [117], LeeNet [118], ResNet [119], etc. have been introduced based on convolution operation. Therefore, CNN-based systems can be used for nodule detection and characterization. Huang *et al*. [120] developed a novel framework by combining the Deep Transfer Convolutional Neural Network (DTCNN) and Extreme Learning Machine (ELM). The proposed DTCNN-ELM model obtained specificity, sensitivity, and accuracy of 95.15%, 93.69%, and 94.57% on the LIDC-IDRI dataset. In [121], a dense binary-tree network is introduced based on convolution operation. The system was used for lung nodule characterization. The framework can preserve the densely connected mechanism of DenseNet and at the same time extract features at different levels from the lung nodule HRCT images. The proposed system achieved a maximum accuracy of 88.31% on the LIDC-IDRI dataset. Liu *et al*. [122] developed a 3D CNN for nodule classification. The framework has obtained an accuracy of 90.60% on the LIDC-IDRI dataset. In [123], a novel Multi-section CNN has been introduced for nodule malignancy estimation. The proposed framework can encode the nodule's volumetric information using a view pooling layer. An accuracy of 93.18% has been achieved by the system on the LIDC-IDRI dataset. In [124], a semi-supervised system has been developed for nodule characterization. The system consists of an unsupervised reconstruction network that has been combined with learnable transition layers and a supervised classification network for better feature extraction. An accuracy of 92.53% is achieved by the proposed model. Shen *et al*. [125] introduced a novel interpretable deep learning framework for nodule characterization. The work combines low-level diagnostic features with the features obtained from convolutional layers. The system obtained an accuracy value of 84.20% on the LIDC-IDRI dataset. Multi-scale features have an important role in object segmentation and classification. In deep learning multi-scale features can be captured by increasing the receptive field. In standard CNN this can be achieved in two ways: 1) by increasing network depth and 2) by enlarging kernel dimension. But the accuracy of the network degrades rapidly with an increase in depth. Enlarging kernel size also increases network parameters, which leads to high training time and computational resources. To solve this problem effectively, the concept of atrous convolution has been first introduced in [126]. The atrous convolution operation can enlarge the receptive field and at the same time maintain the filter size with the same number of training parameters. Therefore, in literature, atrous convolution-based networks are widely used for object segmentation [127-128], classification [129], disease diagnosis [130], human activity recognition [131], noise reduction [132], etc. Qayyum *et al*. [130] introduced an automated framework based on atrous/dilated convolution to detect parasite-infected red blood cells for diagnosing malaria. Researchers have achieved an accuracy, precision, recall, and F1 score of 96.05%, 95.80%, 96.33%, and 96.06%, respectively on the Malaria Cell Images Kaggle dataset. Ward *et al*. [131] designed a dilated temporal CNN for people with cognitive disabilities. The proposed system obtained an average accuracy of 92.66%. Bozorgpour *et al*. [133] developed a DL-based system for the detection of myeloma plasma cells. The shape variations of myeloma cells are captured by learning segmentation maps in various scales based on the concept of atrous convolution. The proposed framework ranked second in the SegPC2021 grand challenge with a mIoU score of 0.9385. In [134], an end-to-end DL framework is introduced using dilated convolution operation for SAR image despeckling. The proposed system was tested on different natural noisy images. The framework demonstrates good speckle-reduction ability and obtained PSNR and SSIM values of 22.97±0.052 and 0.656±0.001, respectively on the Airplane image. Lung nodules are deformable in shape and exhibit lower intensities in the boundary region. Apart from that, in many cases, small benign and malignant nodules resemble similar shapes and intensity profiles in the HRCT images. Therefore, considering the deformability of lung nodules and inspired by previous works, a novel integrated deep-learning framework based on atrous/dilated convolution has been introduced for lung nodule segmentation and classification.

5.2 Research Contributions

In this chapter, a new CADx framework has been developed for lung nodule segmentation and characterization. The framework with its dilated pyramid-based structure can extract useful nodule information from the feature maps at a different scale. The extracted multi-scale features can capture shape and intensity variations of benign and malignant nodules from lung HRCT images effectively. The proposed integrated deep learning framework incorporates atrous convolution operation for lung nodule segmentation and characterization.

The primary contributions of this work are mentioned below:

- **An atrous convolution-aided integrated CNN framework is introduced for lung nodule segmentation and characterization.**
- **A novel attention-based mechanism has been employed for better nodule segmentation.**
- **Multi-scale features have been captured to classify lung nodules based on atrous convolution.**
- **Residual connections have been introduced for better feature preservation.**
- **The proposed framework has obtained higher classification indices compared to the state-of-the-art techniques owing to the introduction of atrous convolution-based segmentation and classification modules.**

5.3 Dataset Details and Pre-processing

The CADx framework is tested and validated through experiments using the HRCT nodule images. The images are taken from the LIDC-IDRI [20] dataset, which is available to the public for lung cancer research. A total of 1018 chest CT scans with a dimension of 512×512 are collected from 1010 patients. The slice thickness of each image varies from 1.25 to 2.5 mm with a pixel size of 0.48-0.72 mm. The individual cases in LIDC-IDRI have been marked by four (4) professional thoracic radiologists based on the nodule diameter d with values of "d ≥3mm", and "d <3mm" respectively for nodule detection. Apart from that, individual cases also have been described by semantic, texture, margin, and malignancy features and are publicly available in an XML file. In this study, the malignancy feature has been used to prepare the dataset for lung nodule characterization. An average malignancy score of less than 3 has been chosen as the benign case. On the other hand, the average malignancy score value greater than 3 is recognized as malignant nodules as suggested by four expert thoracic radiologists. The cases with a malignancy score equal to 3 are marked as undefined and are not taken in the training and test dataset of the framework. It is seen that all the slices in LIDC-IDRI dataset have a high dimensionality of 512×512 which can increase the training time of the network unnecessarily. Hence, in this work, all the slices have been cropped and resized to 64×64 image patches that contain the ROI i.e. lung nodule only. The images collected from LIDC-IDRI are small for training the network. Hence, in this work, different augmentation techniques have been applied to increase the size of the dataset. The augmentation techniques also help to reduce the over-fitting problem. Therefore, each extracted candidate nodule patch is then translated along the x and y-axis with ±2 pixels, horizontal and vertical flip operations, and apply rotation operations of 90º, 180º, and 270 º to generate the augmented images.

5.4 Convolutional Neural Network for Image Classification

This type of architecture initially appeared in the works of Hasegawa *et al.* [135], Lin *et al.* [136], and Lo *et al.* [137]. Lin *et al.* [136] have applied CNN for FP reduction and achieved a cited accuracy. However, owing to limited computational resources, CNN did not receive popularity at that time. In recent years, with the advent of powerful graphics processing units (GPUs) such as TitanX (8 GB, 12 GB), CNNs have gained popularity, especially in the field of biomedical image processing. CNN is the most dominant architecture in deep learning and acts as a powerful feature extractor and classifier.

5.5 An Introduction to Atrous Convolution

Multi-scale image features are of utmost importance for accurate object classification. The dilated convolution also known as atrous convolution is an effective way to capture multi-scale features from images. Let *I* be a grayscale image, then for each location p(x,y) on the image and a filter *w(i,j)*, the *2-D*atrous convolution is defined as follows [138]:

$$f(x,y)=\sum_{i=1}^{M}\sum_{j=1}^{N} p(x+r\times i, y+r\times j)\, w(i,j) \tag{5.1}$$

Here *f(x, y)* is the output image pixel obtained by applying the atrous/dilation convolution with a dilation rate of *r* over the input image pixel *p(x,y)*. The input feature map is convolved with filters that are upsampled by inserting *r-1* zeros. The standard convolution operation can be implemented by setting *r=1*. The atrous convolution operation produces multi-scale features by modifying the filter's field of view. This modification is done by inserting holes inside the filter that are reset to 0. Atrous convolution effectively enlarges the filter size from $k \times k$ to $(k+ (k-1)\ (r-1))\ (k+ (k-1)\ (r-1))$ without increasing the network parameters. This is possible and can be achieved by setting different sampling rates. It can be observed from Figure 5.2 that a 3×3 (Figure 5.2 (a)) filter can act as a filter of size 5×5 (Figure 5.2 (b)) or 7×7 (Figure 5. 2 (c)) with a dilation rate of (2, 2) and (3, 3) respectively. The extracted multi-scale features from each sampling rate are then fused to obtain the feature vector and can be used to predict the object label.

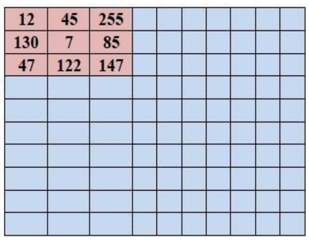

Filter Size= (3,3)
Dilation Rate= (1,1)
(a)

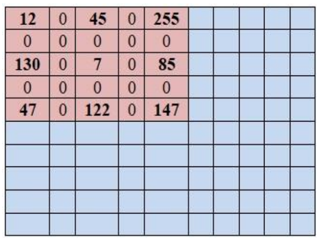

Filter Size= (3,3)
Dilation Rate= (2,2)
(b)

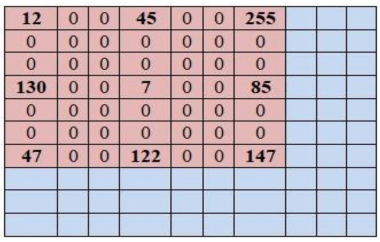

Filter Size= (3,3)
Dilation Rate= (3,3)
(c)

Figure 5.2: The receptive fields of dilated convolution with dilation rate: (a) r=1, (b) r= 2 and (c) r= 3.

5.6 System Implementation

In this section, the ATCNN framework is described in detail. The network has two sub-modules, viz., 1) Segmentation and 2) Classification that represents a complete framework for nodule classification.

5.6.1 Segmentation Module

Atrous convolution operation has been used for both segmentation and classification modules. The basic Atrous convolution-based operation with its different sampling rates allows the network to effectively enlarge the field of view of filters without increasing the number of network parameters. Nodule segmentation is a difficult task due to texture variations. The proposed framework has used Atrous Spatial Pyramid Pooling (ASPP) block to robustly segment and classify lung nodules at multiple scales. The segmentation module of ATCNN has been designed by utilizing the point-wise and depth-wise convolutions of DeepLabV3+ [139] architecture. In the original DeepLabV3+, there are five atrous convolution layers as shown in Figure. 5.3.

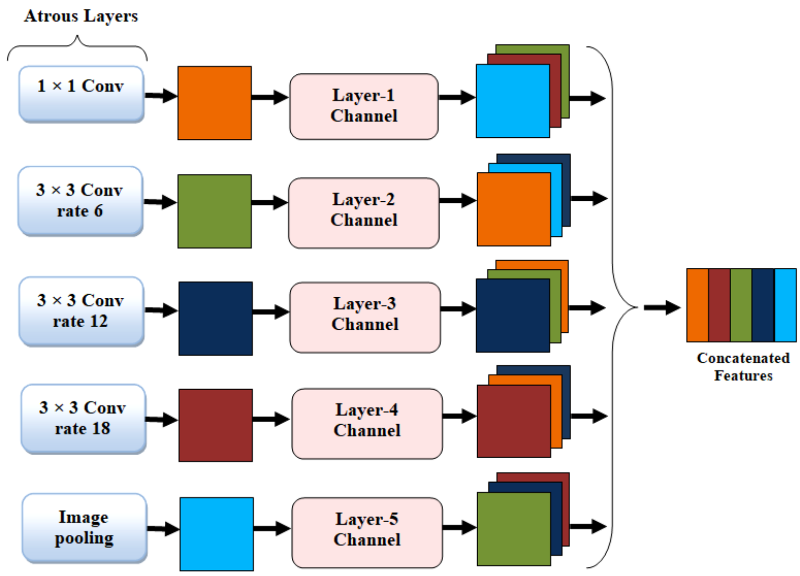

Figure 5.3: Multi-scale feature concatenation block.

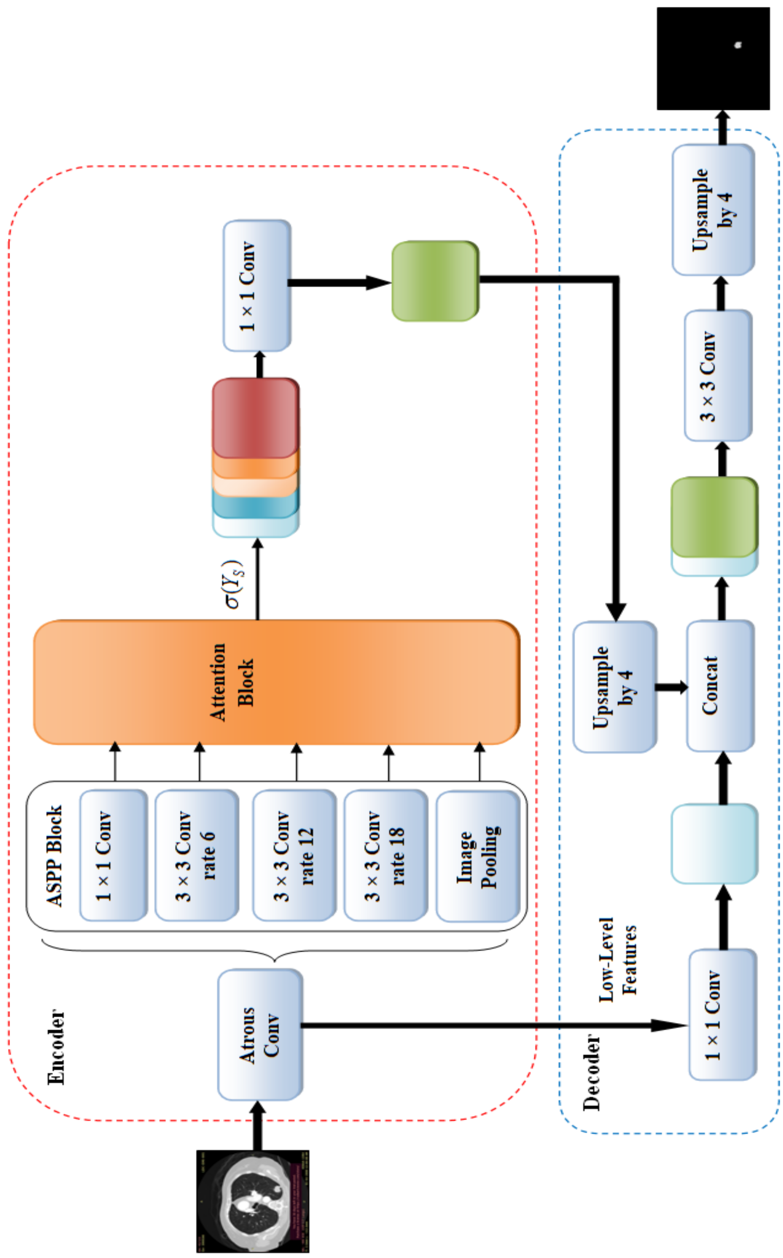

Figure 5.4: Block diagram of ATCNN showing segmentation module.

It can be seen in Figure 5.3 that all the multi-scale features extracted from atrous layers are processed with the same attention level. The extracted features are simply concatenated and fed to the next block. The malignant nodules show variations in shape and texture properties. Therefore, it is necessary to extract those relevant features, which can capture explicit relationships among channels of different atrous layers. In this work, this is achieved by introducing a novel attention-based mechanism inside the "Attention Block" of the segmentation module. Figure 5.4 shows the segmentation module of the proposed ATCNN framework. The introduced attention block has been shown in orange colour inside the segmentation module of Figure 5.4.The block has been placed inside the encoder section to improve the nodule segmentation performance. Initially, the global contextual information has been captured from each feature map produced by each atrous layer. The global average pooling (GAP) operation has been used for this purpose. The GAP operation finds the average from the entire feature map and turned into a single value. Thus the feature vector extracted from feature maps by applying the GAP operation represents the useful global contextual information among the channels. After that, the attention block used two fully connected (FC) layers to learn nonlinear relationships among channels as shown in Figure 5.5.

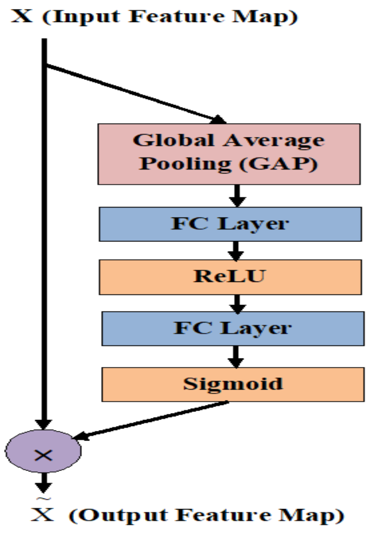

Figure 5.5: Channel-wise attention-based on fully connected nodes.

Let there be S_L ($S_L \in \{1, 2, ..., 5\}$) layers (scales) of dilated convolution in the encoder block inside the segmentation module. Then the learned scale factor S_f for the f_{th} channel can be obtained from the two FC layers as:

$$S_f = \sigma(\mathbf{W_2}\,\delta(\mathbf{W_1}\, g_f)) \tag{5.2}$$

where, g_f is the output obtained by applying global average pooling operation on the input feature map, $\mathbf{W_1}$ and $\mathbf{W_2}$are the learned weight matrices for 1st (hidden) and 2nd (output) fully connected layers, and δ and σ are the activation functions for 1st and 2nd layer respectively. The Rectified Linear Unit (*ReLU*) and sigmoid functions have been used for δ and σ. The output feature map $Z = [x'_1, x'_2, \dots, x'_f]$ is obtained by multiplying every element of the input feature map $X = [x_1, x_2, \dots, x_f]$ with its corresponding scale factor S_f as follows:

$$x'_f = S_f \, . x_f \tag{5.3}$$

It is seen from Figure 5.5 that channel-wise nonlinearity is introduced with the help of fully connected neurons. The important features are learned automatically and prioritized by assigning more weight values using equations (5.2) and (5.3). Apart from learning important features from each channel, the attention block also has introduced the depth-wise attention mechanism. In the original DeepLabV3+ architecture, extracted features from each scale S ($S \in \{1, 2, ..., 5\}$) are simply concatenated and produce the output $Y = [X_1, X_2, ..., X_5]$ as shown in Figure 5.3. Thus DeepLabV3+ architecture gives equal priorities to each feature and most of the time fails to encode important features for segmentation. But in the proposed framework, the trainable attention block learns a weight for each scale. Finally, depth-wise aggregation is used to combine the extracted layer features, as shown in Figure 5.6.

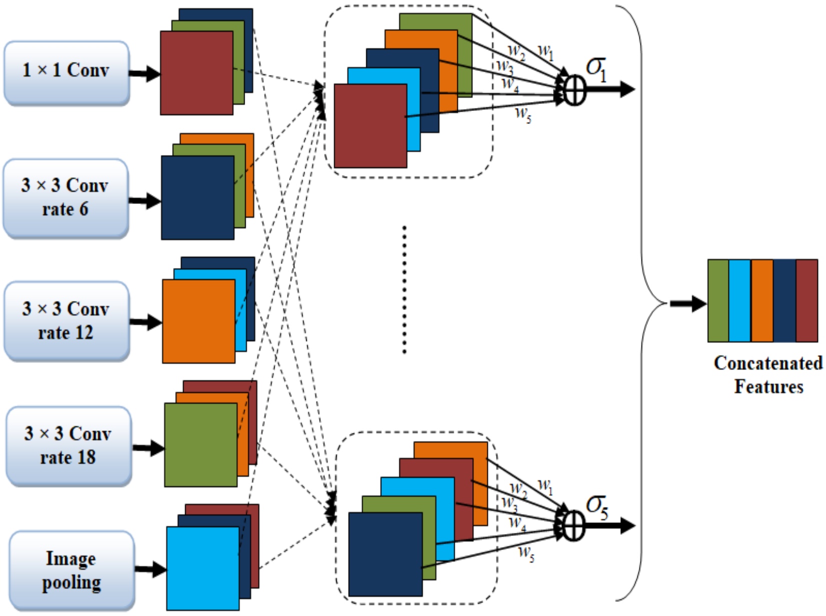

Figure 5.6: Depth-wise attention-based on fully connected nodes.

The output of the attention block is calculated as follows:

$$Y_f = \sigma\left(\sum_{s=1}^{5} w_s X_s^f\right) \tag{5.4}$$

where, X_s^f, w_s are the output feature and learned weight matrix obtained from the f^{th} channel at *the* S^{th} scale, the sigmoid activation function is denoted as σ, and Y_f is the final combined output of the f^{th} channel dilated convolution. Apart from that, the ASPP block has been used inside the encoder to extract multi-scale contextual information. Dilation rates of r=6, 12, and 18 have been used inside the ASPP (Figure 5.4) block of the encoder module. After that, the encoded features are fed to the decoder module to recover the nodule boundary for accurate segmentation. An upsampling factor of 4 has been used for this purpose. After concatenation, a 3×3 convolution operation is applied to further refine the obtained features. Finally, the decoder module used another bilinear upsampling with a factor of 4 to reconstruct the segmented nodule image.

5.6.2 Classification Module

The high-dimensional segmented nodule images produced by the segmentation module of ATCNN are then resized to 64×64 image dimensions. After that, the cropped and resized image patches are sent to the classification module for nodule characterization. The classification module of ATCNN contains both convolution (r=1) and atrous convolution (r>1) operations that can capture multi-scale features from the image patches. Let I_m be the nodule HRCT image and W is the learning kernel, now the basic convolution operation over I_m is written as:

$$F(i,j)=(W*I_m)(i,j)=\sum_p \sum_q W(p,q)*I_m(i-p,j-q) \tag{5.5}$$

where,* is the convolution operation, and F is the feature map that has been obtained by applying the convolution operation. The classification module of ATCNN has been designed using the conventional convolution operation that uses VGG [116] like structure. Layers 1, 2, 3, 4, 5, and 6 of the system have used 16, 32, 64, 128, 256, and 512 respectively, as the number of filters. In the 5th and 6th layers, two dilation pyramids have been used to capture multi-scale features. The 5th layer pyramid (Dilation Pyramid-1) contains an odd number of dilation rates, i.e., r= 1, 3, 5, 7, whereas the 6th layer pyramid (Dilation Pyramid-2) contains an even number of dilation rates, i.e., r= 2, 4, 6, and 8 respectively as shown in Figure 5.7. A dilation rate of r=1 has been used for layers 1, 2, 3, and 4. Increasing the network layer depth often gives a vanishing gradient phenomenon and can degrade the classification performance of DL-based systems. The skip/residual connection is used to avoid the vanishing gradient phenomenon. Therefore, in this work, residual connections have been introduced in the classification module of the ATCNN network. The two residual connections viz., Residual Connection-1 and Residual Connection-2 have been introduced between the input and 3rd layer and between the 4th and 6th layer, respectively. Thus the proposed ATCNN framework can preserve the features that have been produced from its initial layers. A standard kernel of size 3×3 has been used for all the layers inside the classification module. Finally, the extracted multi-scale features from dilated pyramid-1 and 2 are concatenated and passed through the fully connected (FC) layer for nodule characterization.

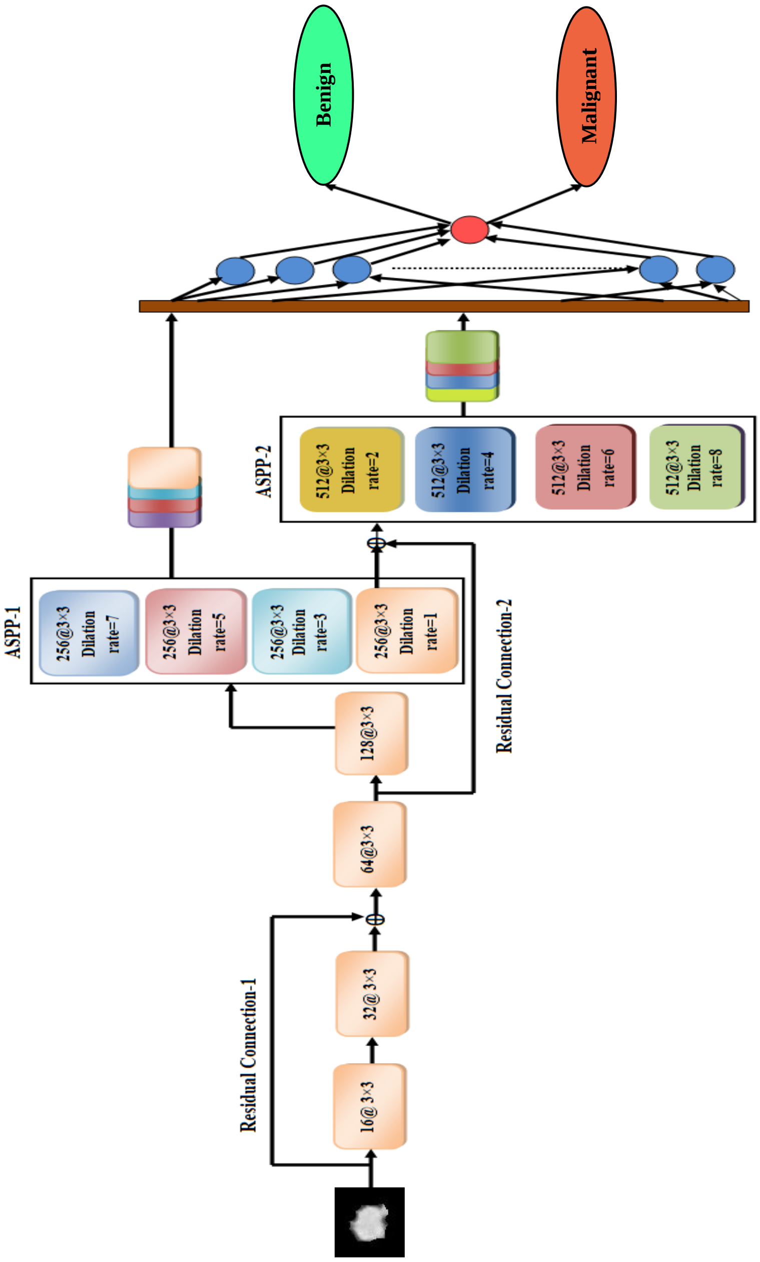

Figure 5.7: Block diagram of ATCNN showing classification module.

Activation function *ReLU* has been used for all the convolution layers and can be written as:

$$ReLU(x) = \begin{cases} 0 & for\, x < 0 \\ x & for\, x \geq 0 \end{cases} \tag{5.6}$$

The classical backpropagation (BP) algorithm has been used to train the classification module. The weights of the network are updated by minimizing the loss function L_{loss}. In this work, Binary Cross Entropy (BCE) is used as a loss function. Let p be the probability of a nodule of being benign and $(1\text{-}p)$ for malignant, then binary cross-entropy or log loss for the two-class problem can be defined as:

$$L_{bce} = -\frac{1}{N}\sum_{i=1}^{N} y_i \, log\,(p\,(y_i)) + (1 - y_i)\, log\,(1 - p\,(y_i)) \tag{5.7}$$

where, N is the total number of nodule images in the training set and y_i is the true label of the training dataset with values '0' and '1' for benign and malignant nodules respectively. Hence, the proposed integrated framework, with the help of atrous convolution-based operation can capture multi-scale features from the target HRCT nodule images that can be used both for segmentation and classification tasks. Different variants of ATCNN viz., ATCNN with one dilated pyramid layer (ATCNN1P), ATCNN with the two-layer atrous pyramid (ATCNN2P), ATCNN two-layer atrous pyramid and residual connections (ATCNN2PR) also have been analyzed for nodule characterization. The classification module of ATCNN1P, ATCNN2P, and ATCNN2PR have used VGG like structure with a standard kernel of size 3×3 and the same number of filters as shown in Figure 5.7. However, ATCNN1P has used one Atrous Spatial Pyramid Pooling (ASPP) block with dilation rates, i.e., r= 1, 3, 5, 7. On the other hand, ATCNN2P has used two ASPP blocks viz. ASPP-1 and ASPP-2 with dilation rates of r= 1, 3, 5, 7 and r= 2, 4, 6, 8 in the 5th and 6th layer respectively. Finally, ATCNN2PR, along with two ASPP blocks, has introduced two residual connections between the input and 3rd layer and between the 4th and 6th layer, respectively for better nodule classification. The details of the obtained results have been discussed below elaborately.

5.7 Experimental Validation and Discussion

This section analyses the performance of the proposed ATCNN framework by considering three aspects viz., (1) nodule segmentation results (2) nodule classification results, and (3) comparing with existing DL-based frameworks. The results obtained from nodule segmentation and classification modules of the ATCNN network have been discussed below in detail.

5.7.1 Dataset and Experimental Setup

The CADx framework is tested and validated through experiments using the HRCT nodule images. The images are taken from the LIDC-IDRI [20] dataset, which is available to the public for lung cancer research. A total of 1018 chest CT scans with a dimension of 512×512 are collected from 1010 patients. The slice thickness of each image varies from 1.25 to 2.5 mm with a pixel size of 0.48-0.72 mm. The individual cases in LIDC-IDRI have been marked by four (4) professional thoracic radiologists based on the nodule diameter d with values of "d ≥3mm", and "d <3mm" respectively for nodule detection. Apart from that, individual cases also have been described by semantic, texture, margin, and malignancy features and are publicly available in an XML file. In this study, the malignancy feature has been used to prepare the dataset for lung nodule characterization. An average malignancy score of less than 3 has been chosen as the benign case. On the other hand, the average malignancy score value greater than 3 is recognized as malignant nodules as suggested by four expert thoracic radiologists. The cases with a malignancy score equal to 3 are marked as undefined and are not taken in the training and test dataset of the framework.The proposed ATCNN network has used a total of 1500 and 500 HRCT nodule slices from LIDC-IDRI to train and test the segmentation module. In the training phase, the backpropagation (BP) algorithm is used with Adam as an optimizer for gradient descent. The segmentation module of ATCNN has been trained with a learning rate (α) of 0.0001 for a maximum of 100 epochs. The classification module of ATCNN has used a uniform dimension of 64×64image patches for lung nodule characterization. A total of 10374 HRCT nodule image patches with a training and validation ratio of 80:20 have been used to train the classification module of the network. Apart from that 4107 nodule slices have been used to test the proposed framework. During the training phase, a learning rate (α) of 0.01 is used for a maximum of 60 epochs by the classification module of ATCNN.

5.7.2 Performance Evaluation of the Framework

The performance of the framework is evaluated through experiments using the HRCT nodule images. The images are taken from the LIDC-IDRI dataset, which is available to the public for lung cancer research. A total of 1018 chest CT scans with the dimension of 512×512 are collected from 1010 patients.

5.7.2.1 Performance of the Segmentation Module

Image segmentation plays an important role in accurate region of interest (ROI) recognition. Recently deep learning methods have achieved remarkable results in the field of image segmentation. The fully convolutional network (FCN) [140] was the first model that used deep learning for semantic segmentation. Apart from FCN, there are outstanding novel segmentation models such as U-Net [141], SegNet [142], RefineNet [143], etc., that have been applied to natural as well as medical images for segmentation tasks. All the models are capable of generating segmentation masks in an end-to-end learning fashion. Therefore, in this work, small lung nodules are segmented for accurate nodule classification. The segmentation module of the proposed ATCNN network has used DeepLabv3+ architecture for nodule segmentation. The framework can extract the true shape of the nodule from the background, and at the same time, can remove other findings, e.g., vessels from the HRCT image slice. The proposed system can classify nodules with higher performance indices due to the introduction of the segmentation module.The nodule segmentation results are then analyzed by computing six segmentation metrics viz., Sensitivity, Specificity, Pixel/Global Accuracy, Dice Similarity Coefficient (DSC), Intersection over Union (IoU)/Jaccard index (JI), and Boundary F1 (BF) score. The used segmentation metrics have been determined using the following standard formulas as mentioned in chapter-3 and chapter-4 respectively. Finally, in this work, a new performance indicator viz., Boundary F1 (BF) score has been used to reflect the contour matching between the GT and the segmented images. A value close to 1 indicates perfect matching of the corresponding class in the predicted image with its ground truth contour. The BF score can be defined using the precision and recall values as follows:

$$BF\,Score = \frac{2 \times precision \times recall}{precision + recall} \tag{5.8}$$

Table 5.1: Nodule segmentation results of the ATCNN on the LIDC-IDRI dataset

#Nodules	**Segmentation Performance Indices**						
	Values	**DSC Score**	**JI Score**	**BF Score**	**Sen. (%)**	**Spec. (%)**	**Acc. (%)**
500	Min	0.8968	0.8792	0.9012	95.24	94.12	94.69
	Max	0.9843	0.9611	0.9661	98.12	99.88	99.45
	Avg	0.9715	0.9520	0.9584	96.71	97.86	96.92

It can be seen from Table 5.1 that the system has obtained a maximum sensitivity of 98.12%, with specificity and accuracy values of 99.88%, and 99.45% on the LIDC-IDRI dataset. The maximum obtained DCS, JI, and BF scores are 0.9843, 0.9611, and 0.9661, respectively. The average nodule segmentation performance indices of ATCNN are 96.71% for sensitivity, 97.86% for specificity, and 96.92% for accuracy with DCS, JI, and BF scores of 0.9715, 0.9520, and 0.9584 on the LIDC-IDRI dataset. The final segmented images obtained by the ATCNN framework have been shown in Figure 5.8. The nodule images have been cropped and highlighted for better visual assessment. Figure 5.8 (a) shows the original cropped nodule slices taken from LIDC-IDRI. The nodules with varying shapes and sizes have been selected to test the segmentation performance of ATCNN. Figure 5.8 (b) shows the ground truth (G.T) images of the selected nodules. The boundary information is obtained by an expert radiologist for accurate G.T. image preparation and labeling. The segmented nodule images obtained from ATCNN are shown in Figure 5.8 (c).

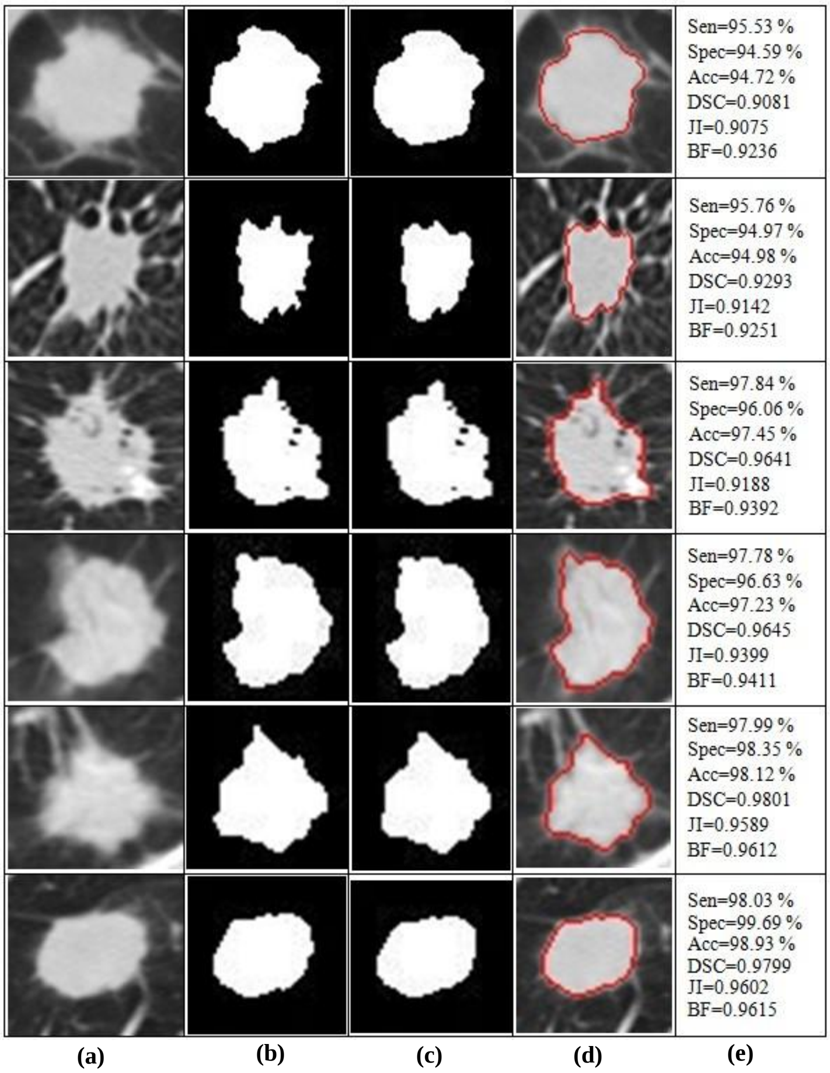

Figure 5.8: Nodule segmentation results: (a) original nodule, (b) ground truth nodule, (c) segmented nodule by ATCNN, (d) nodule overlay image, (e) different nodule segmentation results obtained by proposed ATCNN framework.

It can be visually observed that the segmented nodules have been perfectly matched with ground truth images. The overlaid images are shown in red colour (Figure 5.8 (d)). The segmentation performance indices for each image have been shown in Figure 5.8 (e).

Table 5.2: Performance comparison of different nodule segmentation frameworks on the LIDC-IDRI dataset

#Nodules	Methods	DSC Score	JI Score	BF Score	Sen. (%)	Spec. (%)	Acc. (%)
500	U-Net [141]	0.9281	0.9012	0.8917	90.56	92.22	92.13
	SegNet [142]	0.9476	0.9153	0.9219	90.84	92.97	92.66
	DeepLab V1 [144]	0.9511	0.9342	0.9266	92.12	94.69	93.15
	DeepLab V2 [145]	0.9543	0.9391	0.9310	93.71	95.49	94.10
	DeepLab V3 [146]	0.9599	0.9419	0.9471	95.33	96.69	96.25
	DeepLab V3+ [139]	0.9601	0.9433	0.9486	95.82	97.38	96.33
	Proposed System	**0.9715**	**0.9520**	**0.9584**	**96.71**	**97.86**	**96.92**

Table 5.2 shows the nodule segmentation results obtained by different existing segmentation frameworks on the LIDC-IDRI dataset. The U-Net obtained the lowest sensitivity, specificity, and accuracy of 90.56%, 92.22%, and 92.13% for nodule segmentation. After that, the segmentation task was carried out by considering the SegNet model and obtained a segmentation accuracy of 92.66%. Finally, in this work, shape variations of different nodules have been captured using multi-scale features. Atrous convolution-based frameworks such as DeepLabV1 [144], DeepLabV2 [145], DeepLabV3 [146], and DeepLabV3+ [139] have been used for this purpose. The DeepLabV1, V2, and V3 obtained nodule segmentation accuracy of 93.15%, 94.10%, and 96.25% respectively on the LIDC-IDRI dataset. The DeepLabV3 has removed the conditional random field (CRF) from its module. It is seen from Table 5.2 that a minimum of a 2% increase in nodule

segmentation accuracy has been achieved by DeepLabV3 over DeepLabV2 architecture. After that, to achieve better segmentation accuracy, DeepLabV3+ was used for the nodule segmentation task. The DeepLabV3+ architecture has obtained nodule segmentation sensitivity, specificity, and accuracy of 95.82%, 97.38%, and 96.33% on the LIDC-IDRI dataset which shows the improvement over other atrous convolution-based segmentation frameworks. This is possible, due to the introduction of a simple and effective decoder module in DeepLabV3+ architecture. Finally, in this work, the DeepLabV3+ architecture has been modified by introducing an attention-based block for nodule segmentation. The proposed ATCNN framework, with the help of the attention block, can produce a denser and more accurate segmentation mask of lung nodules. From Table 5.2, it can be observed that the proposed system has obtained the highest nodule segmentation sensitivity of 96.71%, with specificity, accuracy of 97.86%, and 96.92%, among all other state-of-the-art segmentation frameworks. Figure 5.9 shows the nodule segmentation results obtained by different segmentation frameworks. It can easily be interpreted by the visual assessment that the proposed framework can segment the nodule with varying shapes and sizes efficiently. Boundary variations of the nodule have been captured well for the unseen images by the proposed system. Finally, the nodule segmentation result obtained by the proposed system has been compared with different existing deep learning-based nodule segmentation frameworks. Roy *et al*. [147] introduce a deep fully convolutional network for lung nodule segmentation. Researchers have obtained a DSC score of 0.93 on the LIDC-IDRI dataset. Usman *et al*. [148] developed a novel semi-automated 3-D deep residual U-Net. The proposed system obtained an average dice score of 87.5% for nodule segmentation. In [149] a new deep learning framework using Generative adversarial network (GAN) is introduced for nodule segmentation. The proposed Aggregation-U-net GAN (AUGAN) system has obtained a Dice coefficient, Jaccard index, Precision, and Recall of 0.854, 0.756, 0.852, and 0.866, respectively on the LIDC-IDRI dataset. Xiao *et al*. [150] proposed a 3D-UNet Neural Network for lung nodule segmentation and have achieved a dice coefficient index of 95.30% with a recall rate of 99.1%.A new deep-learning model using GAN has been developed in [151]. The introduced segmentation framework is optimized with the Salp Shuffled Shepherd Optimization algorithm and obtained a maximum Accuracy, Dice Coefficient, and Jaccard Similarity Index of 0.9387, 0.7986, and 0.8026 for lung nodule segmentation.

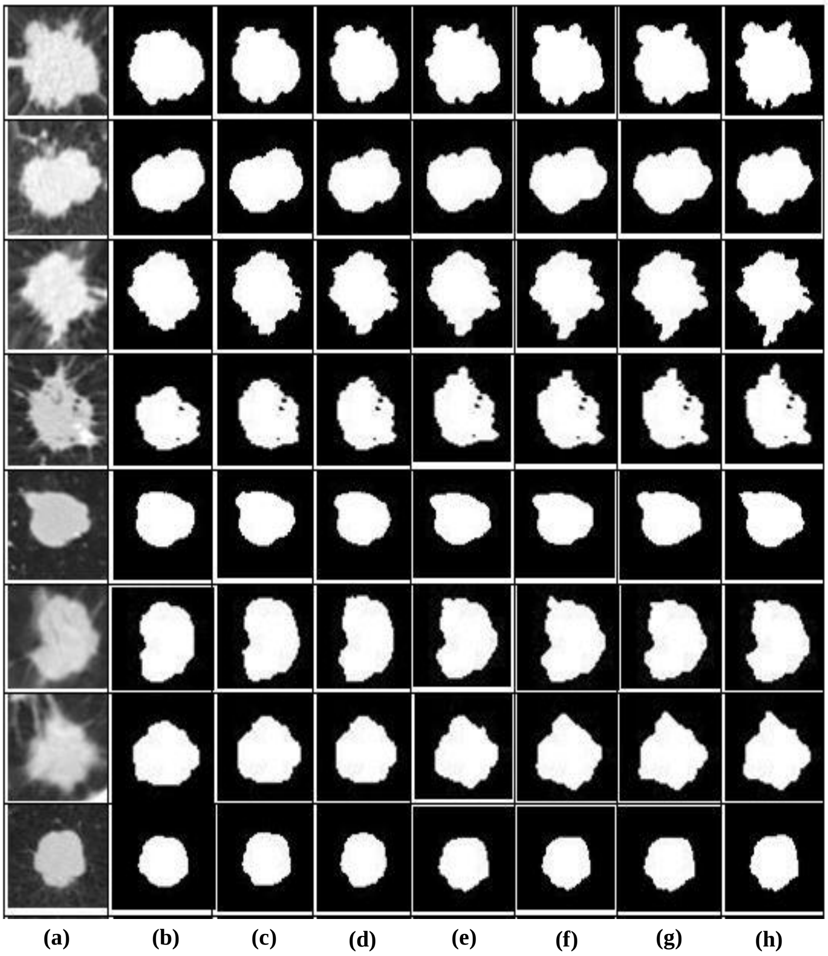

Figure 5.9: Results of different nodule segmentation frameworks: (a) original nodule image, (b) U-Net, (c) SegNet, (d) DeepLabV1, (e) DeepLabV2, (f) DeepLabV3, (g) DeepLabV3+, (h) Proposed System.

Tyagi *et al*. [152] introduced a new DL-based segmentation framework using U-Net architecture and achieved dice coefficient and sensitivity of 80.74% and 85.46%. Lu *et al*. [153] developed a novel deep-learning network named DENSE-UNET for nodule segmentation. The proposed system obtained a Dice score, Precision, and Recall of 0.7442, 0.7551, and 0.7254, respectively on the LIDC-IDRI dataset. Table 5.3 shows the segmentation performance comparison results of different state-of-the-art deep learning frameworks.

Table 5.3: Segmentation performance comparison results of different segmentation frameworks on the LIDC-IDRI dataset

CADx Systems	**DSC Score**
Roy *et al*. [147]	0.9300
Usman *et al*. [148]	0.8750
Shi *et al*. [149]	0.8540
Xiao *et al*. [150]	0.9530
Jain *et al*. [151]	0.7986
Tyagi *et al*. [152]	0.8074
Lu *et al*. [153]	0.7442
Proposed CADx system	**0.9715**

It can be observed from Table 5.3 that owing to the introduction of an attention mechanism combined with a multi-scale feature extraction technique, the proposed ATCNN framework has obtained the highest DSC score of 0.9715 on the LIDC-IDRI dataset.

5.7.2.2 Performance of the Classification Module

This module performs the task of nodule classification. The segmented nodules that are obtained from the nodule segmentation module (Subsection-5.7.2.1) are then passed through this module for malignancy classification. The training time of the classification module can increase due to the high dimensionality of the segmented nodule image, which is 512×512. Therefore, nodule slices have been resized to a uniform dimension of 64×64 image patches before feeding to the classification module. A total of 10374 HRCT nodule image patches with a training and validation ratio of 80:20 have been used to train the classification module of the network. Apart from that 4107 nodule slices have been used to test the proposed framework. Due to the introduction of the segmentation module, the proposed ATCNN can characterize nodules with higher performance indices. Different performance matrices of the proposed ATCNN architecture along with its variants have been shown in Table 5.4.

Table 5.4: Proposed ATCNN framework with classification results on the LIDC-IDRI dataset

Serial Number	**Architecture Under Experiment**	**Without Nodule Segmentation**			**With Nodule Segmentation**		
		Sen. (%)	**Spec. (%)**	**Acc. (%)**	**Sen. (%)**	**Spec. (%)**	**Acc. (%)**
1.	ATCNN with a one-layer atrous pyramid	89.49	91.44	90.12	89.55	92.62	91.93
2.	ATCNN with a two-layer atrous pyramid	93.78	91.65	92.19	94.45	93.17	94.11
3.	ATCNN with two-layer atrous pyramid+ residual connection	**94.67**	**93.96**	**94.03**	**95.84**	**96.89**	**95.97**

The performance indices have been analyzed by considering with and without segmented nodule images. From Table 5.4, it can be seen that the ATCNN network trained with accurate segmented nodule images has obtained almost 2% higher classification accuracy on the LIDC-IDRI dataset. Initially, the ATCNN network was designed with one dilated pyramid layer

(ATCNN1P). The dilated layer has been placed just before the FC layer. The multi-scale features obtained from the dilated layer are flattened and sent to the FC layer. The ATCNN1P network has obtained a sensitivity of 89.55%, specificity of 92.62%, and classification accuracy of 91.93% using segmented nodule images. The ATCNN1P network is then modified by introducing one more layer of the dilation pyramid. The modified architecture is named ATCNN with a two-layer atrous pyramid (ATCNN2P). The ATCNN2P obtained higher classification accuracy owing to the introduction of another dilation pyramid.The first dilation pyramid of ATCNN2P used a dilation rate of r=1, 3, 5, 7, and the second dilation pyramid used dilation rates of r=2, 4, 6, and 8, respectively. Finally, the ATCNN2P has been modified by introducing two residual connections (ATCNN2PR) in the classification module for better nodule characterization. Figure 5.7 shows the complete architecture of ATCNN2PR. The framework, with its residual connections and dilation pyramids, can preserve different previous layer features and, at the same time, can extract multi-scale features from nodule image patches. In this work, all models have used a standard 3×3 kernel for each layer. The sequential path of the networks is designed by following a VGG-like structure having filters of 16-32-64-128-256-512 in layer-1, 2, 3, 4, 5, and 6, respectively.Table 5.4 also demonstrates the performance of ATCNN and its variants on the LIDC-IDRI dataset. Three different metrics have been used to analyze the performance of three (3) different network configurations. Among other variants of ATCNN, the ATCNN2PR has obtained the highest performance indices on the LIDC-IDRI dataset. Classification accuracies of different configurations have been plotted in Figure 5.10. It is seen from Figure 5.10 that due to the integration of the segmentation module with the classification module, the ATCNN achieved an almost 2% increase in nodule classification accuracy. Thus the integrated framework can classify lung nodules with a maximum accuracy of 95.97%. During the training phase, a learning rate (α) of 0.01 is used for a maximum of 60 epochs for all the models. The maximum number of epoch values is set to 60 for optimal performance of the network as there is no further improvement in validation accuracy after 60 epochs. Figure 5.11 shows the training and validation loss of the ATCNN2PR network. The GPU available in Google Colab Pro has been used to run all three models under consideration. The confusion matrix of the proposed ATCNN2PR is shown in Figure 5.12. It can be seen that a total of 1939 benign and 1993 malignant nodules have been classified successfully by the network with an accuracy of 95.97% on the LIDC-IDRI dataset.

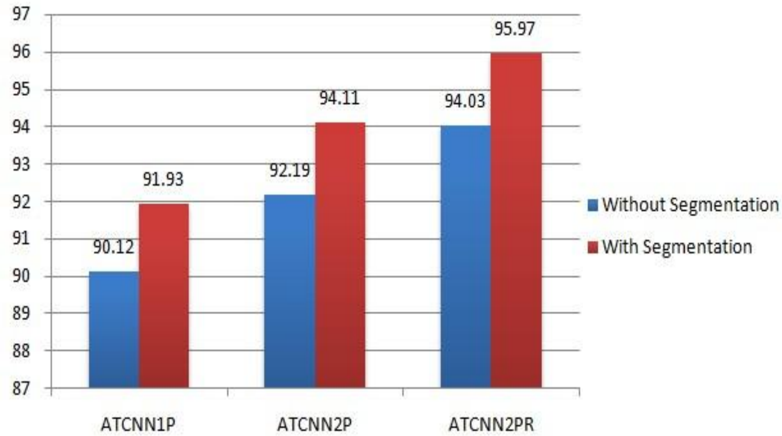

Figure 5.10: Classification accuracy of different networks without and with nodule segmentation.

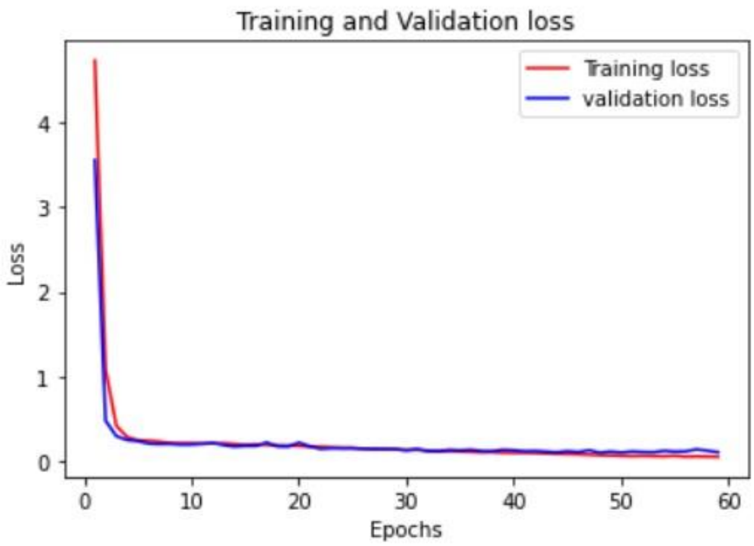

(a)

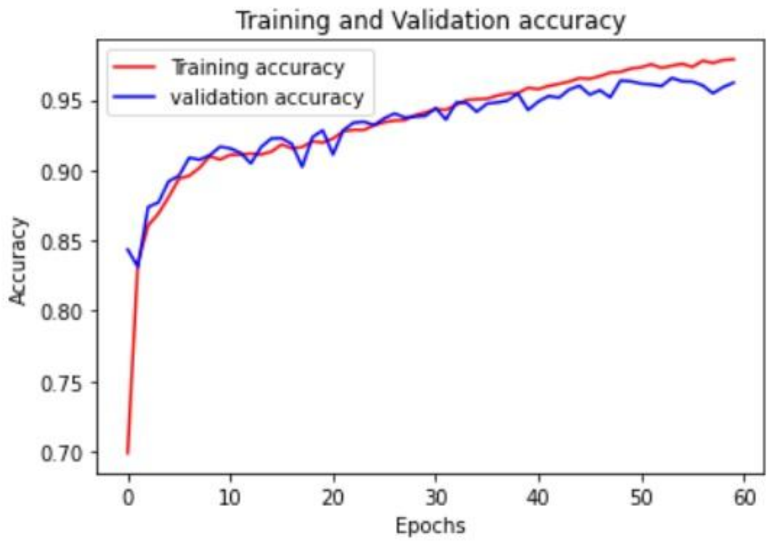

(b)

Figure 5.11: Performance graph plots of ATCNN2PR: a) Loss, b) Accuracy.

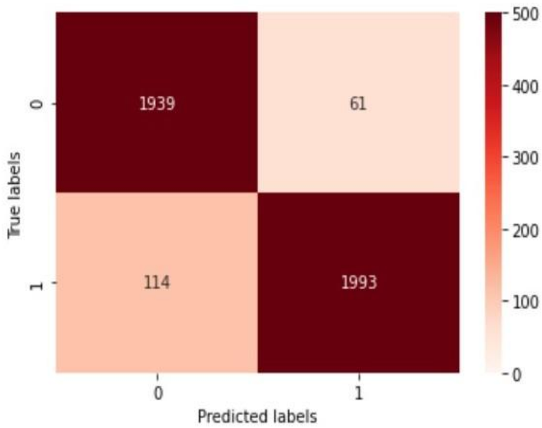

Figure 5.12: Confusion matrix of ATCNN2PR network on the test set.

Finally, the proposed system has been compared with different existing DL-based systems for nodule malignancy characterization. Xie *et al*. [154] developed a nodule classification system based on adversarial autoencoder and semi-supervised learning. Researchers have obtained an accuracy of 92.53% for nodule characterization. Sahu *et al*. [123] introduced a multi-view sampling-based CNN for nodule characterization. The model can encode the nodule's volumetric information with the help of cross-sections obtained using the concept of multiple views. Thus aggregating information obtained from different cross-sections via the multiple views, the pooling layer has been used as a compact feature for nodule classification. The framework obtained a sensitivity of 89.40% on the LIDC-IDRI dataset. In [155] , a novel framework is developed for lung nodule characterization. The multi-view CT images have been prepared from the 3D CT slices by sampled images through three different planes viz., axial, coronal, and sagittal for nodule classification. The ResNet-50 network has been used by the researchers. The proposed system has obtained an accuracy of 83.53% for nodule classification. A 3-D CNN framework combined with ensemble learning has been introduced in [122] and obtained an accuracy of 90.60% for nodule classification. Shaffie *et al*. [156] developed a novel system based on theMarkov Gibbs random field model and obtained an accuracy of 94.95% for lung nodule characterization. In [157], a generative adversarial network (GAN) based CNN has been developed for nodule characterization. The proposed system obtained an average accuracy of 93.9% on the LIDC-IDRI dataset. A new cross-residual-based CNN has been introduced by Lyu *et al*. [158] for nodule characterization. The proposed model achieved a sensitivity of 92.10% for nodule classification. In this work, a novel integrated nodule classification framework has been developed based on the concept of atrous convolution. The proposed system can capture true variations of lung nodules using multi-scale features. Apart from that the integrated framework also contains residual connections that can preserve previous layers' features. Table 5.5 shows different performance metrics of the proposed ATCNN2PR framework along with other DL frameworks applied to the LIDC-IDRI dataset for nodule characterization. From Table 5.5, it is seen that due to the introduction of atrous-based convolution operation, the proposed ATCNN2PR framework has obtained better performance indices for lung nodule classification.

Table 5.5: Performance comparison results of the CADx systems on LIDC-IDRI dataset

CADx Systems	**Sensitivity (%)**	**Specificity (%)**	**Accuracy (%)**
Liu *et al*. [122]	83.70	93.90	90.60
Sahu *et al*. [123]	89.40	95.61	93.18
Xie *et al*. [154]	84.94	96.28	92.53
Zhang *et al*. [155]	80.46	85.99	83.53
Shaffie *et al*. [156]	94.62	95.20	94.95
Suresh and Mohan [157]	93.40	93.00	93.90
Lyu *et al*. [158]	92.10	91.50	92.19
Proposed CADx system	**95.84**	**96.89**	**95.97**

5.7.3 Discussion

The proposed integrated ATCNN framework has been developed for nodule segmentation and characterization. Atrous convolution operation is used to capture multi-scale features from HRCT nodule images. Apart from that attention mechanism has been introduced in the segmentation module of ATCNN for better nodule segmentation. The proposed system is tested and validated through experiments using publicly available LIDC-IDRI dataset. It has been observed that owing to the introduction of attention-mechanism based segmentation module the proposed framework has obtained higher nodule segmentation and classification accuracies as compared to state-of-the-art systems.

5.8 Summary

In this work, we have introduced a deep learning-based integrated framework for lung nodule segmentation and characterization. The proposed ATCNN network has been developed by introducing atrous convolution as its basic operation. The framework can capture multi-scale features from the lung nodule images that have been used both for nodule segmentation and classification tasks. The concept of the Atrous Spatial Pyramid Pooling (ASPP) block combined with residual connection has also been used for better nodule classification. Different variants of the ATCNN network are analyzed on the LIDC-IDRI dataset for lung nodule characterization. Among them, the network with a two-layer atrous pyramid and residual connections (ATCNN2PR) has obtained the highest nodule classification sensitivity, specificity, and accuracy of 95.84%, 96.89%, and 95.97%. Accurate segmentation of lung nodules plays an important role in further classification. Therefore, in this work, a segmentation module based on atrous convolution has been introduced for accurate nodule segmentation. Multi-scale features have been introduced to capture boundary information of lung nodules. A new attention-based mechanism using fully connected neurons has been introduced to concatenate multi-scale features with different attention scales. The proposed system obtains average DSC, JI, and BF scores of 0.9715, 0.9520, and 0.9584 for nodule segmentation on the LIDC-IDRI dataset. It can be observed that owing to the introduction of the nodule segmentation module, the proposed framework obtained almost 2% higher classification accuracy on the LIDC-IDRI dataset. Thus by integrating the segmentation and classification modules under one framework, the proposed ATCNN model has outperformed other deep learning-based systems for nodule characterization.

- ## Publication:

Amitava Halder and Debangshu Dey, "Atrous Convolution Aided Integrated Framework for Lung Nodule Segmentation and Classification," in *Biomedical Signal Processing and Control, Elsevier,* (Impact Factor: 5.10), vol. 82, 104527, Apr. 2023, doi: 10.1016/j.bspc.2022.104527.

Chapter 6

An Adaptive Morphology Aided Deep Learning Framework for Lung Nodule Characterization

6.1 Background and Motivation

Lung cancer has become the major cause of cancer-related deaths all over the world. The presence of a tumor usually refers to a pulmonary nodule characterized by uncontrolled cell growth of lung tissues. WHO [1] through its cancer research agency, the International Agency for Research on Cancer (IARC) [2] reported 2.21 million new lung cancer cases and 1.80 million deaths all over the world in 2020. Thus lung cancer remains the leading cause of cancer death with a contribution of 18.0% of the total cancer deaths. Regions like Eastern and Western Asia, Eastern and Southern Europe, and Micronesia/ Polynesia have shown the highest lung cancer incidence rates for men [159]. In 2021, The ACS [5] estimates about 235,760 new cases of lung cancer cases among which 119,100 are male and 116,660 female in the United States. The society also estimated deaths of about 131,880 people for the year 2021 in the United States. In India, lung cancer has been identified as the most common cancer found in metropolitan cities and southern regions. As per a study by the National Cancer Registry Programme, India [160], 44.0% of males and 47.6% of females were diagnosed with distant metastasis. The nodule present in the lung can be cancerous or benign. A cancerous tumor is also termed a malignant nodule and can spread and grow in other parts of the body if it is not detected early. On the other hand, benign nodules cannot spread but can grow in time and may turn into malignant ones. Accurate follow-up of the disease and proper treatment planning are the primary concerns to defeat lung cancer. In northern India, a hospital-based study has reported 90% of lung cancer patients were diagnosed at an advanced stage [161]. Therefore, accurate detection and characterization of the nodules at an early stage is the utmost requirement and can reduce the lung cancer mortality rate significantly. This can be achieved with the help of different medical imaging devices and techniques that have been invented and are in use for the acquisition of medical images. Among different modalities, HRCT images are highly recommended for nodule detection and characterization owing to their high resolution and non-invasiveness. As per a report of the National Lung Screening Trial (NLST) [19], a 20% reduction in lung cancer mortality is possible with low-dose computed tomography (LDCT) image as compared to chest X-rays. Figure 6.1 (a) and (b) shows some HRCT images of benign and malignant nodules that have been taken from the LIDC-IDRI [20] dataset.

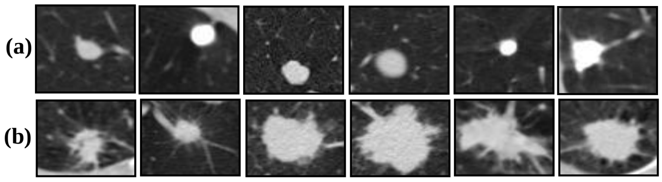

Figure 6.1: Original HRCT lung nodule image: (a) Benign, (b) Malignant. Source: LIDC-IDRI [20].

The HRCT image slices are of huge volume and thus investigation of individual slices is a time-consuming process. Radiologists must examine and analyze each slice for accurate nodule characterization and it is also subjective and heavily relies on the experience of the radiologists. It is also sometimes difficult for the inexperienced radiologist to characterize a nodule as benign and malignant from a visual inspection only. Therefore, to overcome the above-mentioned difficulties different CADx-based systems have been continually developing using pattern recognition and image processing techniques. The CADx system helps the radiologist to take decisions quickly and can act as a second opinion for lung nodule characterization. The CADx-based systems broadly can be designed using (1) hand-craft or feature engineering approach and (2) Deep learning techniques. The steps for hand-craft-based CADx systems include (a) Preprocessing (b) Nodule segmentation (c) Feature extraction (d) Feature selection and (e) classification. Different features e.g. gray level co-occurrence matrix (GLCM)-based features [162, 163, 164], HOG [162], LBP [165], etc. have been used in the feature extraction stage for accurate nodule classification using feature engineering. Recently progress in processor designing techniques and the invention of new generation hardware e.g. graphics processing unit (GPU), different deep learning-based algorithms are in use and can be seen in recent years. The CNN based frameworks are most popular for their simplicity. Different frameworks such as VGG [116], LeeNet [118], AlexNet [117], ResNet [119], GoogleNet [166] etc. have been developed mostly using convolution-operation and obtained significant performance improvement over hand-craft-based systems. Therefore, different CNNs and their variants can be found for lung nodule characterization. Nibali *et al*. [167] developed a CNN based on residual operation for lung nodule classification. Three views (axial, coronal, and sagittal) have been generated from the LIDC-IDRI dataset and used by a 3-pathway-based ResNet architecture. The proposed framework achieved sensitivity, specificity, accuracy, and an Area under the ROC Curve (AUC) score of 91.07%, 88.64%, 89.90%, and 0.9459 on the LIDC-IDRI dataset. Lyu *et al*. [158] designed a multilevel cross residual (ML-xResNet) type architecture for nodule classification. Three parallel paths with kernel sizes 3×3, 7×7, and 11×11 for path-1, 2, and 3 have been designed with cross residual connections for multi-scale feature extraction on the LIDC-IDRI dataset. The proposed ML-xResNet model obtained an accuracy of 85.88% for benign, intermediate, and malignant nodule classification and 92.19% for binary type (benign, malignant) classification. Nasrullah *et al*. [168] designed a deep learning system based on 3D convolution operation. The proposed CMixNet has been used for both nodule detection and characterization. Different features extracted from CMixNet are then fed to the gradient boosting machine (GBM) classifier and obtained a classification accuracy of 91.13% on the LIDC-IDRI dataset. Xie *et al*. [169] introduced a deep learning framework based on a knowledge-based collaborative (KBC) sub-model that contains three pre-trained ResNet-50 networks for benign and malignant nodule classification. The work incorporated a total of nine views to capture 3D nodule characteristics. The proposed multi-view KBC (MV-KBC) framework obtained a classification accuracy of 91.60% with 95.70% AUC on the LIDC-IDRI dataset. Silva *et al*. [170] proposed a CADx system based on a genetic algorithm, named an evolutionary convolutional neural network. The framework has achieved a sensitivity, specificity, and accuracy of 94.66%, 95.14%, and 94.78% with an area under the ROC curve of 0.949 on the LIDC-IDRI dataset. Shabi *et al*. [171] designed a local and non-local block-based framework for nodule characterization. The local features are extracted using residual blocks. On the other hand, non-local blocks are implemented using self-attention layers. An AUC of 95.62% has been obtained by the proposed system. Paul *et al*. [172] developed an ensemble of CNNs for lung nodule malignancy prediction and obtained an accuracy of 90.29% with an AUC value of 0.96. Morphological image processing plays an important role in accurate shape analysis. Therefore, recently deep learning frameworks based on morphological operations are being developed and are in use [173], [174], [175]. Masci *et al*. [173] use the concept of counter-harmonic mean to implement morphological operators. The framework combines morphology-based operations with convolution operations. Basic morphology-based operations along with more complex top-hat transform operations have been thoroughly analyzed in the context of a deep learning framework. Mellouli *et al*. [174] introduced a new framework based on morphological operations. The performance of the system has been evaluated on MNIST and SVHN datasets and obtained recognition rates of 98.87% and 97.13% respectively.

6.2 Research Contributions

In this chapter, a novel deep-learning framework based on morphological operations has been introduced for lung nodule characterization in HRCT images. The new framework with its two parallel trainable paths can capture both texture and morphology-based features from HRCT lung nodule images. To the best of our knowledge, this is the first approach to incorporate adaptive morphology-based operations in the context of deep learning for lung nodule malignancy classification.

The main findings of this research work are summarized as follows:

- **An improvised CNN model combined with morphological operations has been developed for lung nodule classification.**
- **An adaptive morphology-based weight initialization technique is incorporated to obtain the deformable properties of lung nodules.**
- **To capture textural information Gabor filter-based weight initialization technique is developed.**
- **Morphological and textural features are combined using two trainable parallel paths of the CNN model for improved classification of pulmonary nodules.**

6.3 Dataset Details and Pre-processing

The proposed 2PMorphCNN framework has used HRCT images collected from the publicly available LIDC-IDRI dataset. The dataset contains 1018 chest HRCT scans with slice thickness ranging from 0.5 to 5 mm collected from 1010 patients for lung cancer research. The tube current of 40 to 627 mA (mean: 222.1 mA) with a voltage range of 120–140 kVp has been used for data acquisition. All images have a uniform dimension of 512×512 and are stored in DICOM format. Each case has been annotated by up to four expert radiologists as "*d* ≥3mm" and "*d*<3mm", where, *d* is the nodule diameter, in the entire LIDC-IDRI dataset. Apart from that, each CT scan is associated with an XML file that describes nodules using one ordinal attribute (likelihood of malignancy) and eight semantic attributes (sphericity, subtlety, calcification, lobulation, speculation, internal structure, texture, and margin). The nodules are rated and marked with five malignancy levels from 1 to 5. The higher the score is, the more obvious the nodule malignancy case. In this study, each case having an average malignancy score less than 3 has been considered benign whereas an average score greater than 3 has been treated as a malignant case according to the suggestions of four experienced thoracic radiologists. A malignancy score of 3 is treated as an uncertain case and is not included in this study. It is seen that all the slices in LIDC-IDRI dataset have a high dimensionality of 512×512 which can increase the training time of the network unnecessarily. Hence, in this work, all the slices have been cropped and resized to 64×64 image patches that contain the ROI i.e. lung nodule only. The images collected from LIDC-IDRI are small for training the network. Hence, in this work, different augmentation techniques have been applied to increase the size of the dataset. The augmentation techniques also help to reduce the over-fitting problem. Therefore, each extracted candidate nodule patch is then translated along the x and y-axis with ±2 pixels, horizontal and vertical flip operations, and apply rotation operations of 90º, 180º, and 270 º to generate the augmented images.

6.4 Gabor Filter for Textural Feature Extraction

In image processing, the Gabor filter is widely used for texture analysis of the region of interest (ROI). It is a linear filter that finds specific frequency content in a particular direction. The Gabor filter can be defined as the multiplication of a cosine/sine wave with a Gaussian window. The two-dimensional Gabor function [176, 177] can be expressed as:

$$G(x,y)=\exp\left(-\frac{x'^2}{2\sigma_x^2}\right)\exp\left(-\frac{\gamma y'^2}{2\sigma_y^2}\right)\cos\left(\frac{2\pi x'}{\lambda}+\Omega\right), \tag{6.1}$$

with

$$x' = x\cos\theta + y\sin\theta$$

$$y' = -x\sin\theta + y\cos\theta$$

where, *x*, *and y* are the spatial coordinates, σ_x and σ_y are the standard deviation of Gaussian kernel in *x* and *y* directions respectively, Θ determines the orientation of the normal to the parallel stripes of a Gabor function, λ is the wavelength of the cosine factor of the Gabor kernel, γ is the spatial aspect ratio that specifies the ellipticity of the support of the Gabor function, and Ω is the phase offset. By varying Θ one can look for a textured pattern that is oriented in a particular direction. As compared to benign nodules, malignant nodules have different texture patterns and contain rough surfaces. Therefore, in this work, the Gabor filter has been used to capture the texture variations of lung nodules. To achieve this, the weight matrix of the proposed deep network has been initialized with the Gabor filter. The filters/weight matrices are then searched inside the local region of the ROI (nodule) for a matching. Thus, the Gabor-based weight initialization scheme in turn helps to find the discriminating texture pattern of lung nodules.

6.5 Adaptive Morphology: an overview

The concept of adaptive morphology is the generalization of the classical morphology where the structuring elements can change their shape, size, and orientation with the help of local dependency and certain criteria. Different approaches to achieve the adaptation are available in [104-107]. In this work, adaptive structuring elements have been introduced to capture the true shape variation of lung nodules in the context of DL. The details about adaptive morphology can be found in section 4.4 of chapter-4.

6.6 Implementation of Adaptive Morphology Aided Deep Learning System

In this section, the proposed 2-Pathway Morphology-based Convolutional Neural Network (2PMorphCNN) framework has been described elaborately and is developed for lung nodule classification. Figure 6.2 shows the block diagram of the proposed 2PMorphCNN. The network consists of two paths, Path-1 and Path-2. The input to the network is 64×64 nodule patch images. Each patch image is fed to both paths. Convolution operation has been used for Path-1. On the other hand, different image morphology-based operations have been used in Path-2. Both paths of the network have used VGG [14] like layers with 16-32-64-128 as the number of filters for layer-1, 2, 3, and 4 respectively. The texture-based path (Path-1) has used kernels of size 5×5 for layer-1 and layer-2, and 3×3 for layer-3 and layer-4 respectively. The morphology-based path (Path-2) used relatively large size kernels as '7×7' for layer-1 and layer-2 and '5×5' for layer-3 and layer-4. The @ sign has been used to denote the number of filters with its size, e.g., in Figure 6.2 the convolutional and morphological blocks of layer-1 of the network have used 16 filters of size 5×5 (indicated as 16@5×5) and 16 filters of size 7×75 (indicated as 16@7×7) respectively. The paths of the network have been described below in detail.

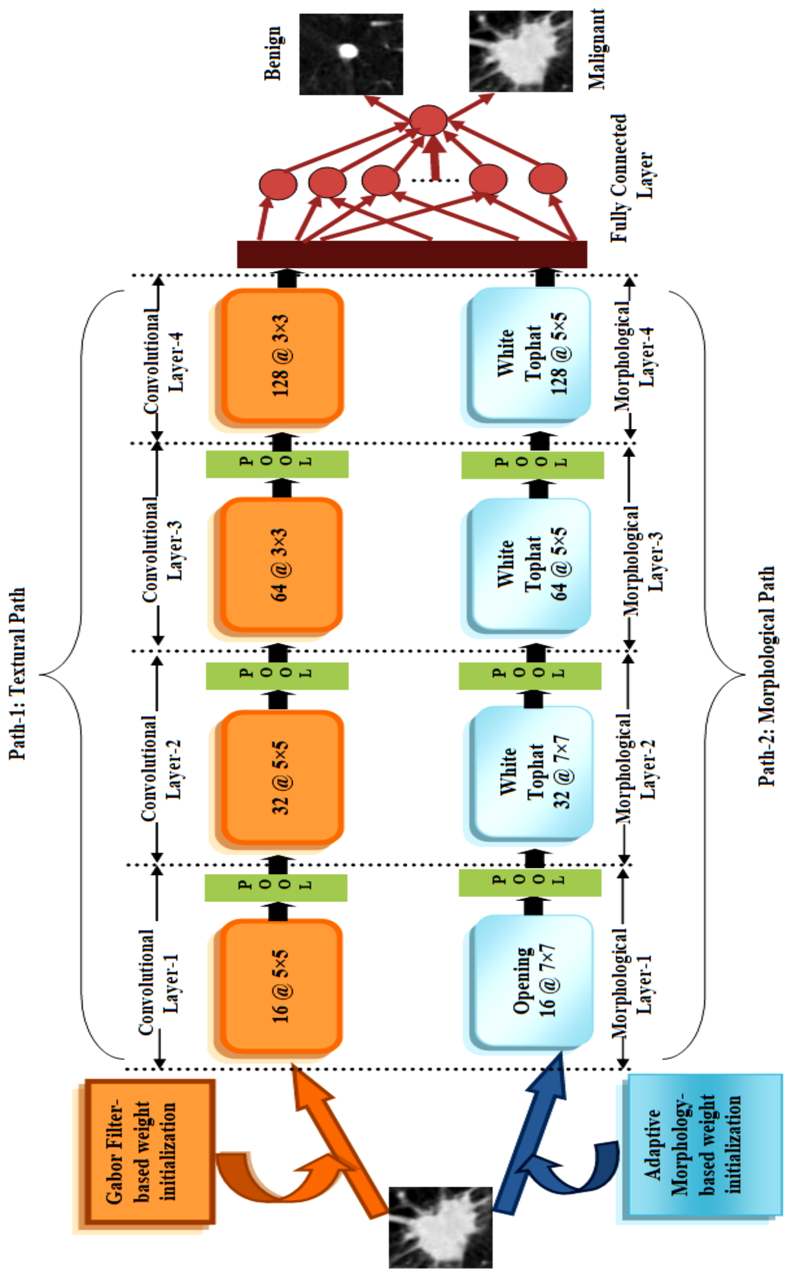

Figure 6.2: Block diagram representation of the proposed framework.

6.6.1 Convolution Neural Network-Based Feature Learning Employing Gabor Filter

This path is based on convolution operations. In this trainable path, convolution operations have been performed with varying sizes of the convolutional kernels. Let *I* be the 2-D image patch and Ker is the kernel then the convolution operation on input image *I* can be defined as:

$$F(i,j) = (Ker * I)(i,j) = \sum_{m}\sum_{n} Ker(m,n) * I(i-m, j-n) \tag{6.2}$$

where, *F* is the output image or feature map produced by applying the convolution kernel or filter. The objective of the CNN-based path (Path-1) is to extract different texture-based features from the patch image with the help of its trainable filters. Therefore, to achieve the desired goal, Path-1 has been initialized with the Gabor filter in different orientations. Hence, all the Gabor filter-based textural features are then searched inside the local image patch for appropriate matching. The trainable filters then learned the true texture pattern from the target nodule patch image by changing its weight values inside the filter. Different filters are capable to extract different texture-based features present in the lung nodule. Let there be *L* layers in Path-1 with weight matrices $W^{[1]}, W^{[2]}, W^{[3]}, \ldots, W^{[L-1]}, W^{L}$ and bias vectors $b^{[1]}, b^{[2]}, b^{[3]}, \ldots, b^{[L-1]}, b^{[L]}$. The input to the path is the patch image *X* having shape $S_{ip} = (no.of\ images, width, height, channels)$ and *Y* is the true label vector of shape $S_{op} = (1, no.of\ images)$. Also, let $\boldsymbol{F_i}$ be a vector that contains the total number of filters at the i^{th} layer of thenetwork each of size $n \times n$. The shape of the $\boldsymbol{F_i}$ vector is

$$S_{\boldsymbol{F_i}} = (number\ of\ input\ channel,\ filter\ width,\ filter\ height, number\ of\ filters\ at\ layer\ L_i)$$

Algorithm 6.1 describes the weight initialization scheme based on the Gabor filter. The orientations of the filters $O_i^1, O_i^2, \ldots, O_i^K \in \boldsymbol{F_i}$ have been obtained by varying Θ in the range [0, π] with an interval of $\left\lfloor \pi/K \right\rfloor$. Here *K* is the number of filters specified in layer L_i.

Algorithm 6.1 Gabor filter-based weight initialization

L: Set of Layers
F: Vector Contains Set of Output Filters for Layer Set L
procedure Gabor_ Initialization $(L_i, \boldsymbol{F}_i)$
    $w \leftarrow \boldsymbol{F}_i(2)$ $//\ 'w'\ \textit{is the kernel width}$
    $h \leftarrow \boldsymbol{F}_i(3)$ $//\ 'h'\ \textit{is the kernel height}$
    $k \leftarrow \boldsymbol{F}_i(4)$ $//\ 'k'\ \textit{is the number of kernels}$
    $Filters \leftarrow \phi$
    $\Omega \leftarrow c_1$ $//\ 'c_1'\ \textit{is a constant value}$
    for θ *in range* $(0, \pi, \lfloor \pi/n \rfloor)$ **do**
        $\lambda \leftarrow$ random_int (min, max)
        $\sigma_x \leftarrow c_2 \lambda$ $//\ 'c_2'\ \textit{is a constant value}$
        $\sigma_y \leftarrow 2\sigma_x$
        $\gamma \leftarrow$ random_ real(min, max)
        $Ker \leftarrow$ get_Gaborker$(w, h, \sigma_x, \sigma_y, \theta, \lambda, \gamma, \Omega)$
        $Filters \leftarrow Filters \cup Ker$
    end for
    $W^{[i]} \leftarrow 0$ $//\ W^{[i]}\ \textit{is the set of weight matrices for}\ L_i$
    for $j = 1\ to\ k$ **do**
        $W_j^{[i]} \leftarrow Filters[j]$
    end for
    return $W_1^{[i]}, W_2^{[i]}, \ldots, W_k^{[i]}$
end procedure

The parameter wavelength (λ) is initialized with random integer numbers using the 'random_int' function, whereas, the parameter aspect ratio (γ) is initialized with real-valued numbers using the 'random_real' function. The values of different parameters (σ_x,σ_y, Θ, λ, γ, Ω) and two constants (C_1 and C_2) used in Algorithm 6.1, have been given in the 'Results and Discussion' section. Finally, the 'get_GaborKer' function returns the desired Gabor kernels using equation (6.1) that have been used as the initial weight matrix for the proposed framework.

6.6.2 Morphology-Based Feature Extraction Employing Adaptive Morphology

In this path, image morphology-based operations have been used. The path can capture different morphology-based features from the nodule patch image. The convolution operation * has been replaced by – for morphological erosion and + for dilation operation respectively. Let I_m be the grayscale nodule image patch of size m×m then erosion and dilation operations using learnable weight matrix on I_m can be defined as follows:

$$E_w = (I_m \ominus W_\varepsilon)(p,q) = \min_{i\in M_1, j\in M_2} (I_m(p-i, q-j) - W_\varepsilon(i,j)) \tag{6.3}$$

$$D_w = (I_m \oplus W_\delta)(p,q) = \max_{i\in M_1, j\in M_2} (I_m(p-i, q-j) + W_\delta(i,j)) \tag{6.4}$$

where, $W_\varepsilon \in R^{a\times b}$ and $W_\delta \in R^{a\times b}$ are the trainable weight matrices for erosion and dilation operations having shape$M_1 \times M_2$, $M_1 = \{1, 2, \dots, a\}$and $M_2 = \{1, 2, \dots, b\}$. The operations defined in (13) and (14) are performed in a windowed fashion using W_ε and W_δ applied on the input image patch. Initially, the weights of the kernels are initialized with He normal distribution. It is a weight initialization technique that uses normal distribution with a mean (μ) of zero and a standard deviation (σ) of $\sqrt{2/F_{in}}$, where F_{in} is the number of inputs to the node. The flat shapes of the kernels are then modified using the concept of adaptive morphology as discussed in section-2. The morphology-based path is initialized with ellipse shape structuring elements having different sizes and orientations. Thus the modified structuring elements are named adaptive structuring element (ASE) denoted as W_{Adpt_ε} and W_{Adpt_δ} have been used in this work. The modified erosion and dilation operations using adaptive structuring element on input image I_m can be defined as follows:

$$E_{Adpt\_w} = \left(I_m \ominus W_{Adpt\_\varepsilon}\right)(p,q) = \min_{i\in n, j\in n}\left(I_m(p-i,q-j) - W_{Adpt\_\varepsilon}(i,j)\right) \tag{6.5}$$

$$D_{Adpt\_w} = (I_m \oplus W_{Adpt\_\delta})(p,q) = \max_{i\in n, j\in n}\left(I_m(p-i,q-j) + W_{Adpt\_\delta}(i,j)\right) \tag{6.6}$$

where, $\ominus$ and $\oplus$ are the erosion and dilation operations and W_{Adpt_ε}, W_{Adpt_δ} are the adaptive weight matrices/structuring elements of erosion and dilation operations formed inside *the* $n \times n$ weight filter. The weight initialization scheme is written elaborately in Algorithm 6.2. The proposed algorithm is taking similar arguments L and vector $\boldsymbol{F}$ as its formal arguments as of Algorithm 6.1. However, an additional parameter flag has also been used to indicate the current morphological operation. Basic erosion and dilation operations are executed by the network based on flag values supplied to the procedure. The flag is set to '*E*' for erosion and '*D*' for dilation operation respectively. The elliptical regions have been formed with the help of Ellip_Reg function that takes the weight matrix, semi-major and minor axis as its formal arguments. It can be observed in Algorithm 6.2 that $+\infty$ value is used with the 'erosion' operation for the points that are outside the elliptical region. In a grayscale image, the intensity value is in the range [0,255]. Therefore, in practice, a value that is outside the range of grayscale image and greater than 255 has been chosen for $+\infty$. For example, a value of 256 can be used for those points that are outside the elliptical region. Thus by using a large positive value, the erosion operation is forced to choose the minimum point from the points that are inside the bounded elliptical region. The elliptical region acts as the structuring element for the operation. Similarly, for the 'dilation' operation, a large negative value (denoted as $-\infty$ in Algorithm 6.2) e.g., -1 can be used for the points that are outside the elliptical region. Hence, the dilation operation is bounded to choose the maximum value from the points that are inside the elliptical region only. The morphology-based path initially used morphological opening operation in layer-1. The opening operation with its adaptive structuring elements finds the regions that fit the structuring elements inside the image patch. It also removes objects that are smaller than the weight matrix/structuring element ***W***.

Algorithm 6.2 Adaptive Morphology-based weight initialization

---

L: Set of Layers
F: Vector Contains Set of Output Filters for Layer Set L
Flag: Variable taking value 'E' for erosion
    and 'D' for Dilation
procedure Morph_Initialization $(L_i, \boldsymbol{F_i}, flag)$
    $w \leftarrow \boldsymbol{F_i}(2)$ // 'w' *is the kernel width*
    $h \leftarrow \boldsymbol{F_i}(3)$ // 'h' *is the kernel height*
    $k \leftarrow \boldsymbol{F_i}(4)$ // 'k' *is the number of kernels*
    $W^{[i]} \leftarrow$ He_Normal(size(L_i)) // $W^{[i]}$ *is the set of weight matrices for* L_i
    for $j = 1$ *to* k **do**
        $W_{Adpt\_j}^{[i]} \leftarrow W_j^{[i]}$
        $Y \leftarrow \mathrm{centre}(W_{Adpt\_j}^{[i]})$
        $a \leftarrow \dfrac{\lambda_1(Y)}{\lambda_1(Y)+\lambda_2(Y)} \times w$ // 'a' *is the semi-major axis length*
        $b \leftarrow \dfrac{\lambda_1(Y)}{\lambda_1(Y)+\lambda_2(Y)} \times h$ // 'b' *is the semi-minor axis length*
        $R \leftarrow$ Ellip_Reg($W_{Adpt\_j}^{[i]}$, a, b)
        for *each point* $P(x, y) \in W_{Adpt\_j}^{[i]}$ **do**
            if $(P(x, y) \notin R$ *and* $flag ==$ 'E'$)$ **then**
                $W_{Adpt\_j}^{[i]}(x, y) \leftarrow +\infty$
            else if $(P(x, y) \notin R$ *and* $flag ==$ 'D'$)$ **then**
                $W_{Adpt\_j}^{[i]}(x, y) \leftarrow -\infty$
            end if
        end for
    end for
    return $W_{Adpt\_1}^{[i]}, W_{Adpt\_2}^{[i]}, \ldots, W_{Adpt\_k}^{[i]}$
end procedure

Thus opening, in turn, helps to extract nodules from the background image and it also removes noise if present inside the image patch. The small details of the lung nodules are then explored by applying three consecutive white top-hat operations on the image patches in layer-2, 3, and 4 respectively. The trainable top-hat filters can detect bright spots (nodules) in the image patch. Let I_m be the input image to the network and E_{Adpt_w}, and D_{Adpt_w} are the basic erosion and dilation operations using adaptive structuring element (ASE) then morphological opening operation can be defined as follows:

$$O_{Adpt\_w}(I_m) = (D_{Adpt\_w} \circ E_{Adpt\_w})(I_m) \tag{6.7}$$

The white top-hat image (I_{wt}) can be obtained by subtracting the opening image I_o from the input image I_m as follows:

$$I_{wt} = I_m - I_o \tag{6.8}$$

The extracted textural and morphology-based features are then fused and fed to the fully connected (FC) layer of the network for nodule malignancy classification. The activation function ReLU has been applied for all the layers $L^i : i \in \{1, 2, 3, 4\}$ of Path-1. For a morphology-based path, there is no need for any activation function as morphological operations are inherently non-linear as they use maximum and minimum operators for basic erosion and dilation operations. This is another advantage of the proposed framework. Thus with the help of morphological operations, Path-2 can easily capture non-linearity from the input nodule image patch which is helpful for malignancy classification. After applying ReLU, the convolutional and morphology-based outputs from each layer (except the final layer) are further processed through a max-pooling layer of size 3×3 for feature dimension reduction. The max-pooling layers are indicated by the green rectangle in Figure 6.2. In the final layer, all the extracted features are kept intact for better classification and fed to the fully connected layer. The FC layer is similar to an artificial neural network (ANN) where each node/neuron is connected to the previous layer neurons. Hence, the outputs of layer-4 from Path-1 and Path-2 are concatenated and flattened, and fed to the FC layer for classification. A total of 128 neurons have been used in the hidden layer of the *FC* layer. Let ***w*** be the weight matrixconnected from the FC layer to the output layer *O*. Then the error function $E_{i,n}$ at the output layer has been computed by taking the component-wise difference between the target value *T* and output value O. The n^{th} component of i^{th} feature vector can be expressed as:

$$E_{i,n} = T_{i,n} - O_{i,n} \; \forall n \tag{6.9}$$

In this work, loss function BCE has been used for benign and malignant nodule classification. The expression for BCE has already given in chapter-5. The proposed framework has been trained using classical backpropagation algorithm; optimized with Adaptive Moment Estimation (Adam) for gradient descent. Weights and biases are updated by minimizing L_{bce} using the gradient descent principle as follows:

$$\left.\begin{aligned} w_{qr} &\leftarrow w_{qr} - \eta \frac{\partial L_{bce}}{\partial w_{qr}} \\ b_k &\leftarrow b_k - \eta \frac{\partial L_{bce}}{\partial b_k} \end{aligned}\right\} \tag{6.10}$$

where, w_{qr} is the weight connected from neuron q of $(k\text{-}1)$-th layer to neuron r of k-th layer and η is the learning rate. The parameters i.e. weights and biases of the proposed network updated by the BP algorithm may be stuck in local minima. Therefore, in this work, a momentum value Λ has been added with the weight update rule as given below:

$$w_{qr} \leftarrow w_{qr} + \eta\,(T_r - O_r).O_q + \Lambda \Delta w_{qr} \tag{6.11}$$

Proper weight initialization of deep neural-based networks plays an important role in better learning or training of the network. Hence, better-initialized weights in turn help to reach the optimum value quickly with a lesser number of iterations. Therefore, apart from the momentum value, in this work, two new weight initialization schemes based on the Gabor filter and adaptive morphology have been introduced. The weight matrices of the textural path (Path-1) have been initialized with the Gabor filter by following the equation (6.1) oriented in different directions. Thus path-1 can capture more texture information from the target nodule image that leads to better discrimination of cancerous nodules. Lung nodules resemble elliptical/circular shapes in HRCT slices. Therefore, weight matrices of the morphological path (Path-2) have been initialized with different elliptical-shaped SEs that are oriented in different directions. The parameters i.e. semi-major axis a, semi-minor axis b, and orientation ψ of different structuring elements (SEs) have been optimized using equations (4.7), (4.8), and (4.9) as described in chapter-4.

The equations use two eigen values λ_1 and λ_2 to capture true data variations inside the $n \times n$ grid kernel/weight matrix. The structuring elements take the shape of an ellipse when there are large variations i.e. $\lambda_1 \gg \lambda_2 \approx 0$ and form a circle when $\lambda_1 \approx \lambda_2$. In this work, the morphological Opening and White tophat operations have used these optimized SEs for a perfect match with the target lung nodule. The basic erosion and dilation operations choose pixels that are inside the optimized structuring element masks.Hence, the proposed network with its optimized weight parameters can capture both texture and morphology-based features from the target nodule image with a lesser number of iterations and is more likely to obtain the higher performance indices of sensitivity, specificity, and accuracy values that have been analyzed and discussed in the next section.

6.7 Experimental Validation and Discussion

In this section, the performance of the 2PMorphCNN network has been observed by (1) comparing with different 2-Pathway-based networks and (2) comparing with existing deep learning-based systems. All the necessary results have been analyzed and discussed in the following subsections in detail.

6.7.1 Dataset and Experimental Setup

The proposed 2PMorphCNN has been trained and tested on the publicly available LIDC-IDRI dataset. Initially, 2600 nodule images have been chosen from the dataset. The designed dataset contains 1300 and 1300 slices of benign and malignant nodules in the HRCT modality. It is seen that all the slices in LIDC-IDRI dataset have a high dimensionality of 512×512 which can increase the training time of the network unnecessarily. Hence, in this work, all the slices have been cropped and resized to 64×64 image patches that contain the ROI i.e. lung nodule only. The images collected from LIDC-IDRI are small for training the network. Hence, in this work, different augmentation techniques have been applied to increase the size of the dataset. The augmentation techniques also help to reduce the over-fitting problem. Therefore, each extracted candidate nodule patch is then translated along the x and y-axis with ±2 pixels, horizontal and vertical flip operations, and apply rotation operations of 90º, 180º, and 270 º to generate the augmented images. Finally, after augmentation, a total of 10374 HRCT nodule slices have been produced to train the network. The augmented dataset is then divided into training (80%) and validation (20%) set for training and validating the proposed system.

Table 6.1: Training and validation set used by the 2PMorphCNN framework

Dataset Used	**# Nodules in Training Set**		**# Nodules in Validation Set**		**Total**
	Benign	**Malignant**	**Benign**	**Malignant**	
LIDC-IDRI	4160	4160	1027	1027	10374

Table 6.1 shows the number of nodule slices that have been used in this study. It can be seen that a total of 8320 nodule slices (4160 benign and 4160 malignant) have been used for training the network whereas, 2054 nodule slices (1027 benign and 1027 malignant) used to validate the proposed framework. After training and validation, the system has been tested 4107 nodule images that were not been used in the training and validation sets. In this work, both paths of the network have used 16-32-64-128 as the number of filters (k) for layer-1, 2, 3, and 4 respectively. The kernel size is denoted as $n \times n$ with width w and height h. The texture-based path (Path-1) has used kernels of size 5×5 (w=5, h=5) for layer-1 and layer-2, and 3×3 for layer-3 and layer-4 respectively. The morphology-based path (Path-2) used kernels of size '7×7' for layer-1 and layer-2 and '5×5' for layer-3 and layer-4. The texture-based path has been initialized with the Gabor filter. Different parameters of the filter have been given at the time of weight initialization of the network in run time. The orientation (Θ) of the filter can take values in the range of 0° to 180° with an interval of $\left\lfloor 180^{\circ}/k \right\rfloor$, The wavelength (λ) is set to a minimum value of 5 to the maximum value of 100, the values of σ_x and σ_y have been derived from the equality $\sigma_y = 2\sigma_x = 1.12\,\lambda$ as suggested in [178] , a semi-open interval of (0, 1] has been used for the parameter aspect ratio (γ) that specifies the ellipticity of the support of the Gabor function. The support is circular for $\gamma = 1$ and elongated in the orientation of the parallel stripes of the function for $\gamma < 1$. Finally, in this work, a constant phase offset (Ω) of 90° has been used to detect the edges from the nodule images. The

morphology-based path (Path-2) has been initialized using the concept of adaptive morphology as discussed in subsections 2.2 and 3.2. All models have the same kernel size and the number of filters. During the training phase of the models, a backpropagation algorithm with a learning rate (η) of 0.01 has been used and trained for a maximum of 60 epochs.

6.7.2 Performance Evaluation of the Framework

Pattern recognition, the post-feature extraction process, takes some suitable features and partitions the feature space into classes. In the initial days of vision-based measurement, features were extracted from the high dimensional input images followed by a pattern classification process.

6.7.2.1 Comparison with Different 2-Pathway-Based Network Configurations

The performance of the proposed 2PMorphCNN framework is then compared with different 2-Pathway-based models. In this work, a 2-Pathway model based on convolution operation (2-Pathway CNN) has been used as a baseline model as shown in Figure 6.3.The 2-Pathway CNN model has two paths of varying size filters. Path-1 consists of filters of size 5 and 3, whereas, Path-2 contains filters of size 7 and 5 respectively. Hence, Path-1 is used to classify small nodules and Path-2 has been used to classify relatively large nodules from HRCT images. The 2-Pathway CNN is then modified by introducing a morphology-based path and two initialization schemes based on the Gabor filter and adaptive morphology respectively. The variants of different with and without morphology-based deep learning models are shown in Table 6.2.

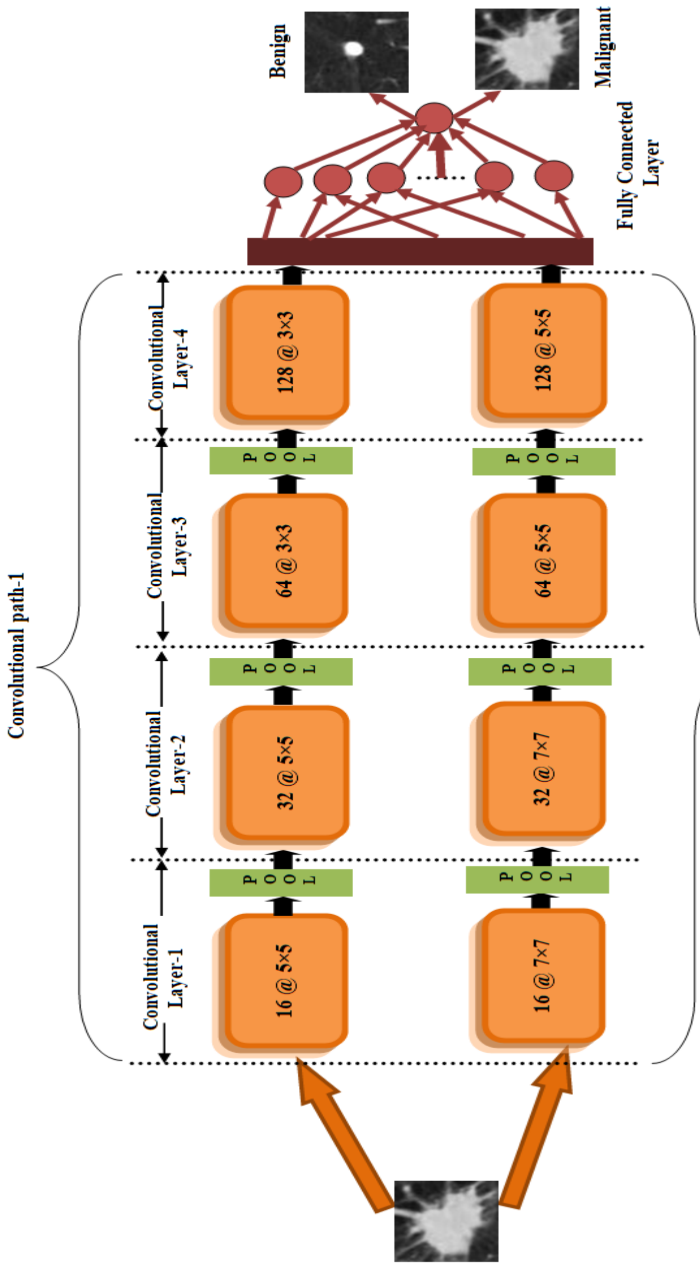

Figure 6.3: Block diagram representation of the 2-Pathway CNN network.

Table 6.2: Different with and without morphology-based deep learning frameworks under consideration

Serial Number	Architecture Used	Used Method	Weight Initialization Scheme
1.	2-Pathway CNN	Paths have been designed using the convolution operation	He normal-based weight initialization for both paths
2.	2-Pathway GFCNN	Paths have been designed using the convolution operation	Gabor filter-based weight initialization for both paths
3.	SMorphCNN	Paths have been designed using convolution operation and morphology-based operation	Gabor filter-based weight initialization for Path-1 and He normal-based weight initialization for Path-2
4.	2PMorphCNN	Paths have been designed using convolution operation and morphology-based operation	Gabor filter-based weight initialization for Path-1 and Adaptive Morphology-based weight initialization for Path-2

The 2-Pathway Gabor Filter-based Convolutional Neural Network (GFCNN) resembles the same architecture as of 2-Pathway CNN but both paths are initialized with the Gabor filter. Morphology-based features play an important role in accurate object classification. Hence, in this research work, morphological variations of benign and malignant nodules have been taken into account by introducing morphological operations in the context of a deep learning framework. Owing to this, Path-2 of GFCNN has been replaced by morphological operations. Initially, the morphological opening operation is used in layer-1 which is followed by three white top-hat operations in layer-2, 3, and 4 respectively. The architecture is named a 2-Pathway Simple Morphological Convolutional Neural Network (SMorphCNN). Path-1 of SMorphCNN has been initialized with the Gabor filter. The trainable filters are then convolved in a layer-wise fashion. Morphological operations have been implemented in Path-2 using relatively large filters of sizes 7 and 5. Structuring elements can form well in large-sized filters and can capture morphological features from the HRCT nodule slices by using different morphological operations. He normal distribution has been used to initialize filters in Path-2 of SMorphCNN. Finally, in this work, a new architecture named 2-Pathway Morphology-based Convolutional Neural Network (2PMorphCNN) has been introduced by modifying the weight initialization scheme based on the concept of adaptive morphology as already discussed in subsection 3.2. The morphology-based path (Path-2) of the 2PMorphCNN is initialized with circular or elliptical-shaped trainable structuring elements generated on the fly from He normal distribution using the concept of adaptive morphology. The proposed 2PMorphCNN is developed on the Google platform. Owing to this Google Colab Pro has been used in this study. Different Graphical Processing Units (GPUs) available in the run time environment have been used to run the system. Python 3.6.9 is used as the programming language to develop the model. It has been observed that the proposed network has taken approximately four (4) hours for training on the LIDC-IDRI dataset. After completion of training, the system can predict a single nodule slice in 0.43 sec. Therefore, it is seen that the proposed network is taking a small amount of time to predict a single image. Hence, there is no significant processing delay by the proposed network. Table 6.3 demonstrates the performance of all DL-based configurations that run on the LIDC-IDRI dataset using Google Colab Pro.

Table 6.3: Different 2-Pathway-based systems with performance indices on the LIDC-IDRI dataset

Serial Number	**Architecture Under Consideration**	**Sensitivity (%)**	**Specificity (%)**	**Accuracy (%)**
1.	2-Pathway CNN	88.49	86.44	87.12
2.	2-Pathway GFCNN	93.78	92.65	93.11
3.	2-Pathway Simple MorphCNN	95.34	94.14	94.16
4.	2-Pathway MorphCNN	**96.85**	**95.17**	**96.10**

In this study, sensitivity, specificity, and accuracy have been used for the performance analysis of four different network configurations. It can be observed from Table 6.3 that all the models except 2-Pathway CNN have given a considerable accuracy value of above 90% on the LIDC-IDRI dataset. The 2-Pathway CNN that has been initialized with He normal distribution has given an accuracy value of 87.12%. This shows that the convolution operation alone is notsufficient to classify lung nodules accurately with higher sensitivity and specificity. To overcome the limitations of 2-Pathway CNN, the GFCNN has been used. The GFCNN network consists of two paths that are initialized with Gabor filters. It can also be seen from Table 6.3 that as compared to 2-Pathway CNN, the GFCNN has achieved a considerable accuracy of 93.11% by capturing the texture features of lung nodules. The SMorphCNN has achieved a classification accuracy of 94.16% on the LIDC-IDRI dataset, which is an improvement of 1.05% over the GFCNN architecture. This is possible owing to the introduction of the morphological path. The SMorphCNN, with its learnable filters, can compute both texture and morphological features of lung nodules and can classify benign and malignant nodules with higher accuracy values as compared to other networks e.g., 2-Pathway CNN and GFCNN. Structuring elements that are used by SMorphCNN are flat in shape with fixed size but lung nodules resemble circular and elliptical shapes in HRCT slices. It has been observed that benign nodules are mostly circular in shape whereas malignant nodules are deformable. Therefore, an accurate nodule classification system must capture these variations to distinguish lung nodules. Therefore, to overcome the limitations of SMorphCNN, in this work, a new architecture 2PMorphCNN has been introduced based on the concept of adaptive morphology. Accurate shaped SE can match the ROI exactly in the local regions of images. Therefore, the 2PMorphCNN has been initialized with different circular and elliptical shape structuring elements that are generated using the concept of adaptive morphology. These on-the-fly trainable SEs are then applied all over the input HRCT slice and look for a particular pattern inside it locally. Thus in Path-2, all the morphological operations have been computed using these shape-variant SEs. It can be observed from Table 6.3 that owing to the use of an adaptive morphology-based weight initialization scheme, the 2PMorphCNN achieved the highest sensitivity, specificity, and classification accuracy of 96.85%, 95.17%, and 96.10% over all other reference architecture. Apart from sensitivity, specificity, and accuracy, the performance of the proposed 2PMorphCNN along with other reference models has also been investigated using the K-fold cross-validation [179] technique where, K is chosen as 3, 5, and 10. Average accuracy has been computed for each of the four models under consideration and the obtained results have been shown in Table 6.4.

Table 6.4: Results of *K*-fold cross-validation of different 2-Pathway-based networks on the LIDC-IDRI dataset

K-fold Cross Validation	Obtained Mean Accuracy (%) ± σ			
	2-PathwayCNN	GFCNN	SMorphCNN	2PMorphCNN
K=3	87.89±0.1286	92.74±0.1153	93.57±0.1136	**95.91±0.1024**
K=5	88.14±0.1239	93.10±0.1096	94.23±0.1076	**96.02±0.0519**
K=10	90.13±0.1176	93.14±0.1047	94.30±0.0793	**96.06±0.0416**

It can be observed from Table 6.4 that the proposed 2PMorphCNN obtained the highest average classification accuracies for all values of K on LIDC-IDRI dataset. Figure 6.4 shows the loss and accuracy plot of the proposed framework. It can be observed that the training and validation losses are almost the same and close to zero. The training and validation accuracies also have minimal differences. Hence, it can be concluded from Figure 6.4 (a) and (b) that the proposed model doesn't overfit the training dataset. The AUC values of GFCNN, SMorphCNN, and 2PMorphCNN are plotted in Figure 6.5. It can be seen that the proposed 2PMorphCNN obtained a maximum AUC of 0.9936 whereas SMorphCNN and GFCNN obtained AUC values of 0.9825 and 0.9806 respectively.

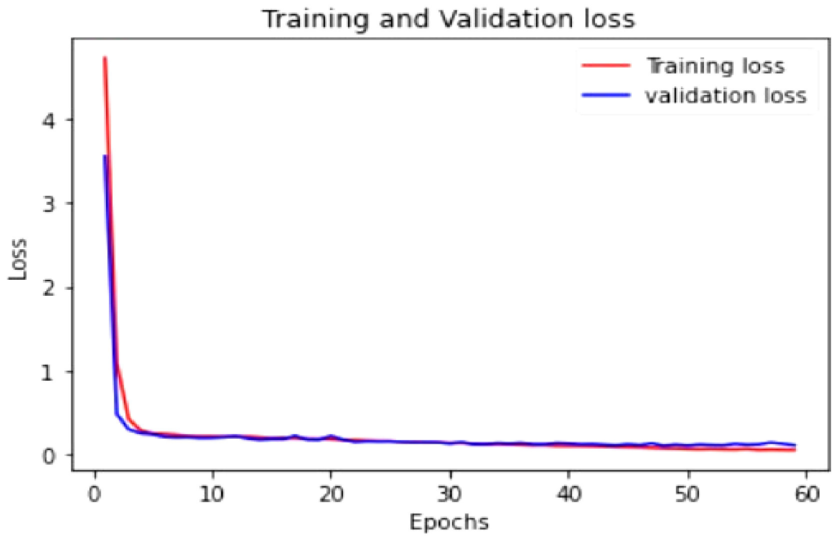

(a)

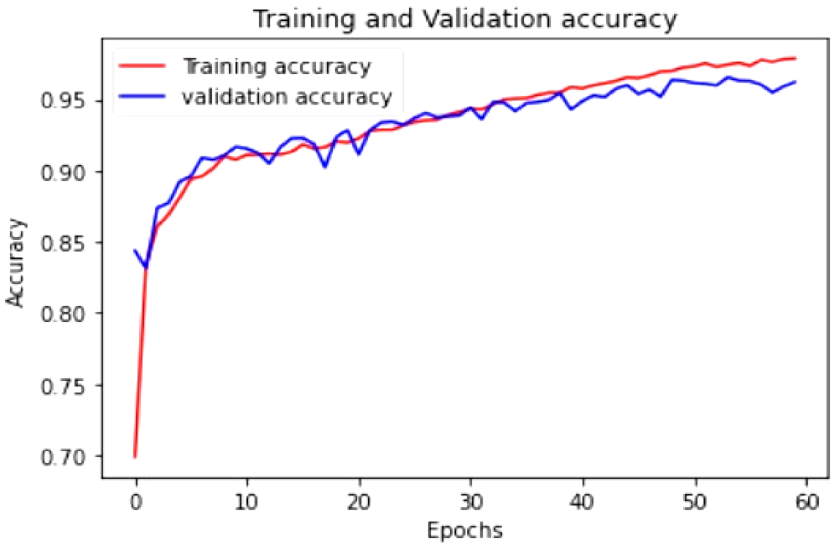

(b)

Figure 6.4: Performance of 2PMorphCNN on training and validation set: a) Loss, b) Accuracy.

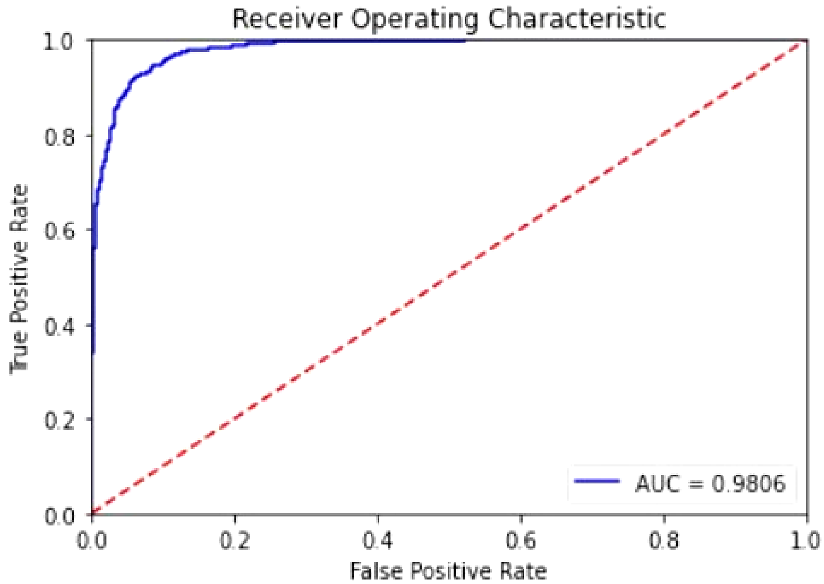
Receiver Operating Characteristic
1.0
0.8
0.6
0.4
0.2
0.0
True Positive Rate
AUC = 0.9806
0.0
0.2
0.4
0.6
0.8
1.0
False Positive Rate

(a)

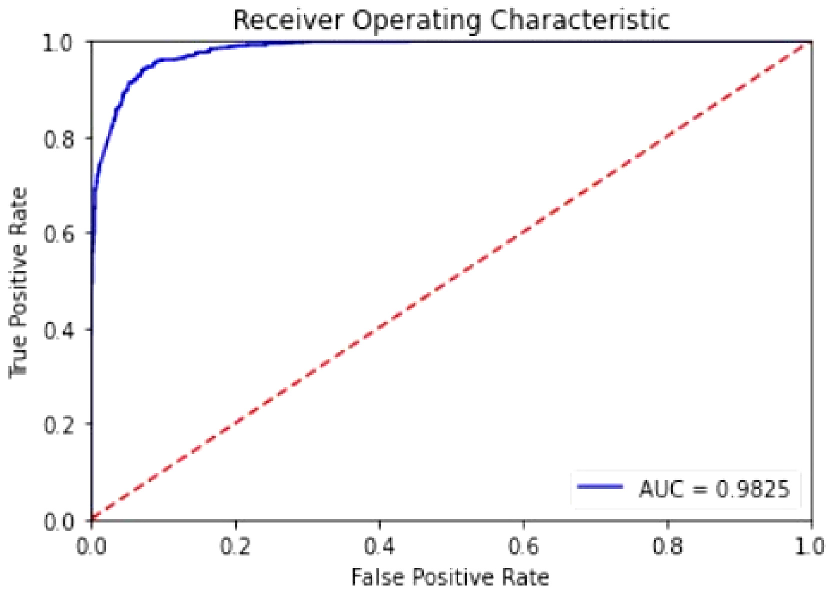
Receiver Operating Characteristic
1.0
0.8
0.6
0.4
0.2
0.0
True Positive Rate
AUC = 0.9825
0.0
0.2
0.4
0.6
0.8
1.0
False Positive Rate

(b)

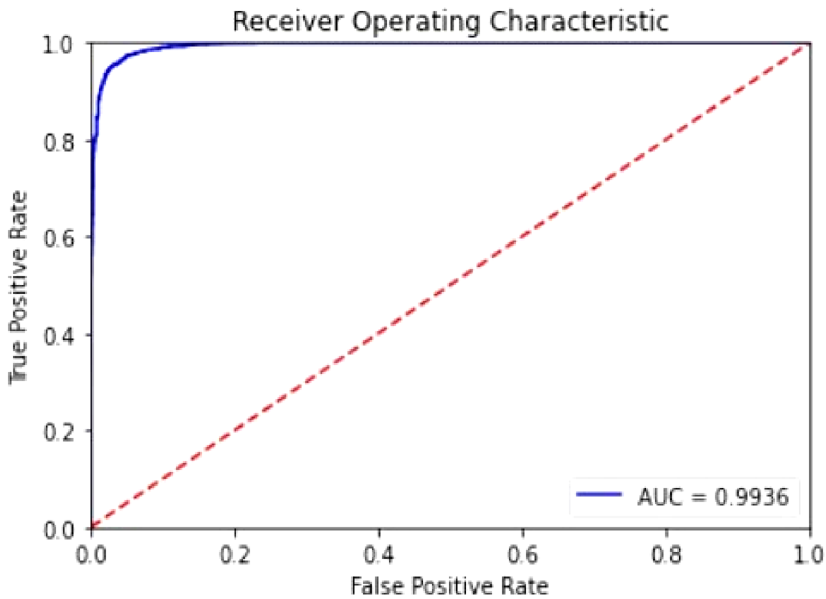

(c)

Figure 6.5: AUC value of a) GFCNN, b) SMorphCNN, and c) 2PMorphCNN.

6.7.2.2 Comparison with Existing Deep Learning-Based Networks

In this subsection, the performance of the framework has been compared with different state-of-the-art deep learning-based systems and validated on the LIDC-IDRI dataset for accurate nodule classification. Shen *et al*. [180] designed a Multi-crop Convolutional Neural Network (MC-CNN) that can extract salient information from the nodule images with the help of a novel multi-crop pooling strategy. The proposed MC-CNN has obtained sensitivity, specificity, and accuracy of 77%, 93%, and 87.14% respectively with an AUC score of 0.93 on the LIDC-IDRI dataset. Filho *et al*. [181] used topology-based phylogenetic diversity index and CNN for lung nodule classification and obtained sensitivity, specificity, accuracy, and AUC of 90.7%, 93.47%, 92.63%, and 0.934 respectively. Jiang *et al*. [182] proposed an attention-based Dual Path Networks (DPNs) based on 3-D convolution operation CNN and achieved a sensitivity, accuracy, and F1 score of 92.04%, 90.24%, and 90.45% on LIDC-IDRI dataset. Shen *et al*. [125] introduced an interpretable semantic convolutional neural network for lung nodule characterization. The proposed HSCNN system has achieved a sensitivity, specificity, accuracy, and AUC of 70.50%, 88.90%, 84.2%, and 0.856 respectively. Xie *et al*. [169] proposed a multi-view knowledge-based collaborative (MV-KBC) based deep learning model. The proposed model obtained sensitivity, specificity, accuracy, and AUC score of 86.52%, 94.00%, 91.60%, and 95.70% on the LIDC-IDRI dataset. Zhao *et al*. [183] introduced a new Agile convolutional neural network (CNN) framework for nodule classification. The proposed framework achieved an accuracy of 82.23% with an AUC value of 0.877. Lyu *et al*. [158] introduced a Multi-level cross-residual-based CNN for lung nodule classification. Researchers have achieved sensitivity, specificity, accuracy, and AUC of 92.10%, 91.50%, 92.19%, and 97.05% on the LIDC-IDRI dataset. Suresh and Mohan [157] have designed a CNN that has been initialized with generative adversarial networks (GANs). The proposed network obtained an average sensitivity, specificity, and classification accuracy of 93.4%, 93%, and 93.9% with an AUC value of 0.934 on the LIDC-IDRI dataset. Table 6.5 shows the sensitivity, specificity, accuracy, and AUC values of the proposed 2PMorphCNN along with other CNN-based CADx systems. Apart from CNN, deep learning networks based on morphology operations also exist in the literature. Mellouli *et al*. [174] introduced a new framework based on morphological operations. The proposed system has been analyzed on MNIST and SVHN digit datasets and achieved recognition rates of 98.87% and 97.13% respectively. Lin *et al*. [184] developed a deep-level cascade CNN based on image morphology. The newly introduced framework obtained classification accuracy and mean average precision (mAP) scores of 85.8% and 0.923 respectively on the wetland vegetation dataset. Therefore, encouraged by the previous works, the network models proposed in [174] and [184] have been implemented and evaluated on the LIDC-IDRI dataset for lung nodule classification. The obtained results are furnished in Table 6.6. It has been observed that the proposed 2PMorphCNN framework can classify lung nodules with better and higher performance indices values. This is possible owing to the introduction of morphology-based operations combined with the texture-based features that have been used in this work.

Table 6.5: Performance comparison of the proposed CADx framework with other deep learning-based models on the LIDC-IDRI dataset

CADx Systems	**Sensitivity (%)**	**Specificity (%)**	**Accuracy (%)**	**AUC Score**
Lyu *et al*. [158]	92.10	91.50	92.19	0.970
Xie *et al*. [169]	86.52	94.00	91.60	0.957
Shen *et al*. [180]	77	93	87.14	0.93
Filho *et al*. [181]	90.7	93.47	92.63	0.934
Jiang *et al*. [182]	92.04	-----	90.24	-----
Shen *et al*. [125]	70.50	88.90	84.2	0.856
Zhao *et al*. [183]	-----	-----	82.23	0.877
Suresh and Mohan [157]	93.4	93	93.9	-----
Proposed CADx system	**96.85**	**95.17**	**96.10**	**0.9936**

Table 6.6: Performance of different morphology-based frameworks on the LIDC-IDRI dataset

Morphology-based Work	**Accuracy**
Mellouli *et al*. [174]	93%
Lin *et al*. [184]	92.14%
2PMorphCNN	**96.10%**

6.7.3 Discussion

In this chapter, a new deep-learning framework has been introduced for lung nodule characterization. The proposed 2-Pathway Morphology-based Convolutional Neural Network (2PMorphCNN) consists of two paths. The weight matrices for Path-1 have been initialized by employing the concept of adaptive morphology. On the other hand, Path-2 has used the Gabor filter for weight matrix initialization. Thus the proposed 2PMorphCNN network can capture both textural and morphological features from the input HRCT lung nodule image. The framework is tested and validated on the LIDC-IDRI dataset and obtained the highest classification accuracy of 96.10% for lung nodule characterization.

6.8 Summary

In this research work, a deep learning framework has been introduced for lung nodule classification from the HRCT images. The proposed 2PMorphCNN network has been designed by introducing a morphological path initialized with adaptive structuring elements. Different morphological features are then learned by employing image morphology-based operations. The extracted features are combined with textural features for accurate nodule classification. The textural path has been initialized with the Gabor filter. The system can recognize benign and malignant nodules as well as lung masses with a sensitivity, specificity, and accuracy of 96.85%, 95.17%, and 96.10% with an AUC score of 0.9936 on the LIDC-IDRI dataset. It has been observed experimentally that 2PMorphCNN can capture the morphological variations of benign and malignant nodules and can compute different morphological features with its trainable filters automatically from the dataset. The framework is also able to learn textural features from the dataset. Thus by combining the morphological and textural features the proposed framework has obtained considerable performance indices and can act as a second opinion for doctors and radiologists for accurate nodule characterization.

- **Publication:**

Amitava Halder, Saptarshi Chatterjee and Debangshu Dey, "Adaptive Morphology Aided 2-Pathway Convolutional Neural Network for Lung Nodule Classification," in *Biomedical Signal Processing and Control, Elsevier*, (Impact Factor: 5.10), vol. 72, 103347, Feb. 2022, doi: 10.1016/ j.bspc.2021.103347.

Chapter 7

An Attention-Based Morphology Aided Deep Learning Framework for Lung Cancer Subtype Classification

7.1 Background and Motivation

Lung cancer is characterized by uncontrolled growth of lung cell tissues and become most frequently diagnosed cancer all over the world. It has been found that lung cancer contributes almost 25% of all cancer related deaths [5]. In 2020, WHO) [1] has reported 1.80 million deaths from lung cancer worldwide. As per report of the ACS [5], in 2022, about 236,740 new cases of lung cancer with 130,180 estimated deaths have been projected in US. In Southeast Asia, the estimated age-standardized incidence rate is 26.4 per 100000 in males and 9.6 per 100000 in females [185]. Histopathologically, there are 2 main types of lung cancers 1) Non-small cell lung cancer (NSCLC) and 2) Small cell lung cancer (SCLC). It has been found that about 80% to 85% lung cancers belong to the NSCLC category, whereas 10% to 15% are SCLC. The NSCLC is most common lung cancer and can be treated surgery, chemotherapy, and radiation therapy, chemotherapy, and in some cases, targeted therapy. The adenocarcinoma (ADC), squamous cell carcinoma (SCC), and large cell lung carcinoma (LCLC) are the subtypes exist for NSCLC. Figure 7.1 (a), (b), and (c) shows the benign and two subtypes of lung cancer viz., ADC and SCC respectively. From Figure 7.1 it can be observed that owing to the structural similarity of ADC and SCC, pathological evaluation of cancer subtypes is difficult task and cancer grading require highly trained and experienced pathologists.

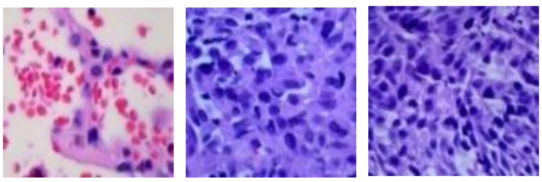

(a) **(b)** **(c)**

Figure7.1: Lung cancer histopathology images of (a) benign, (b) adenocarcinoma, and (c) squamous cell carcinoma. Source: LC25000 [21].

It has been found that an early stage, surgical resection of NSCLC offers 5-year survival rates up to 70% for stage-I tumors [186]. Therefore, early recognition and proper treatment of carcinoma can increase the five year survival rate. In clinical practice, Biopsy is considered as gold standard diagnostic technique that removes the tissue sample from the lesion. Histopathology refers to the scientific analysis of the tissue samples under a microscope. However, owing to the structural similarity, pathological evaluation of cancer subtypes and grading require highly trained and experienced pathologists. Apart from that, histopathology images are very large in size and have high dimensions. The images must be broken down into multiple small patches before analysis. The images may be also taken at multiple magnifications to obtain the coarse and details view of the lesion. Therefore, manual evaluation of cancer subtypes and cell morphology from histopathological images is subjective, error prone, and time-consuming process. In recent years, researchers have developed different CAD systems to overcome the limitations and challenges faced by pathologists. The CAD systems are able to classify lesions accurately from digital histology images. The applications include cell/nuclei detection and segmentation [187-189], cancer subtype classification [190-204], and automatic grading [205-208] to quantify cancer malignancy levels. Traditionally researchers have developed ML-based CAD systems using different classifiers. Veta *et al.* [187] proposed a marker-controlled watershed algorithm for nuclei segmentation and achieved an accuracy of 81.2%. Kumar *et al.* [188] developed a nuclei detection system using texture, shape, wavelet, colour, and HOG features. Authors have used K-means algorithm for nuclei segmentation. The proposed system obtained an accuracy of 92.19% using KNN classifier. Albayrak *et al.* [189] introduced a cell segmentation scheme based on SLIC superpixel algorithm and achieved F-measure value between 63.7% and 65%. Li *et al.* [190] introduced a ML-based framework for lung cancer subtype classification. Authors have used LBP, GLCM, GLGCM texture and moment features in their study. The proposed system obtained a classification accuracy of 73.91%, 83.91%, and 73.67%, respectively on LUSC-ASC, LUSC-SCLC, and ASC-SCLC datasets using support vector machine (SVM) classifier. Wang *et al.* [191] classified ADC and SCC using ML approach and obtained highest classification accuracy of 95.42% on full tissue sections of histopathology images. Yu *et al.* [192] used 9,879 quantitative image features to distinguish ADC and SCC. Authors have achieved an average AUC value of 0.81 using random forest classifier. Nishio *et al.* [193] proposed a CADx system using Homology-based image processing (HI) technique. Authors have obtained 99.43% classification accuracy for lung cancer subtype classification. Pourakpour and Ghassemian [194] proposed a mitosis cell detection system using Gamma-Gaussian Mixture Model (GGMM). Authors have used GLCM, LBP, and shape-based features in their studyand obtained F-measure of 92.30% using SVM classifier. Zhang *et al*. [195] classified breast cancer using texture-based features. Authors have used Curvelet Transform, GLCM and Completed Local Binary Pattern (CLBP) features in their study. The proposed system obtained classification accuracy of 95.22%. Loukas *et al*. [196] introduced an ML-based system to access the degree of malignancy for breast cancer. Three classifiers viz., KNN, SVM, and PNN have been used in the study. Researchers have achieved highest average classification accuracy of 90% using PNN classifier. Anuranjeeta *et al*. [197] introduced an automated system for breast cancer classification. The proposed system obtained highest classification accuracy of 85.70% using Rotation Forest (RF) classifier. Albashish *et al*. [198] developed a multi-level learning architecture (MLA) for prostate cancer classification. The proposed system obtained an overall sensitivity of 90.22% on a private dataset. Recently, with the advancement of technology and availability of Graphical Processing Units (GPUs), deep learning based systems are widely used for the development of CAD frameworks. Among different techniques, CNN is most popular owing to its simplicity and automatic feature extraction capability. Therefore, different CAD-based frameworks using CNN have been developed for medical image analysis and classification. Wang *et al*. [199] introduced a new system for multiclass classification of breast histopathology image. The proposed DBLCNN framework obtained an accuracy of 96.58% on BreaKHis dataset. Zou *et al*. [200] introduced a dual stream high-order framework for breast cancer classification. The network is named as DsHoNet and obtained patient-level classification accuracy of 97.15% on BreaKHis dataset. Roy *et al*. [201] introduced a patch-based classifier (PBC) using convolution operation for histopathological breast image classification. Authors have achieved classification accuracy of 90% and 92.5% for 4-class and 2-class classification of breast cancer respectively on ICIAR-2018 dataset. Qaiser *et al*. [202] introduced a novel DL framework for tumor segmentation of colorectal cancer. Authors have used two private dataset contain colorectal adenocarcinoma histopathology images. Wei *et al*. [203] introduced a DL framework for predominant histologic pattern classification in lung adenocarcinoma. Researchers achieved a kappa score of 0.525 on a private dataset. Tokunaga *et al*. [204] developed an Adaptive-Weighting-Multi-Field-of-View CNN for lung cancer subtype segmentation in histopathology image. Authors have used multiple views of Whole Slide Imaging (WSI) images for better segmentation result. It has been observed by the work of Cong *at el*. [205] that different models using conventional convolution operation have been developed for lung cancer subtype classification. Mathematical morphology plays a vital role for accurate segmentation and object recognition. The preliminary morphological operations are able to extract and analyze the topological structure of the region of interest (ROI). Therefore, morphology-based image processing techniques are widely used in medical domain for lesion segmentation and classification. Nayak *et al*. [209] introduced a cell segmentation scheme based on modified fuzzy divergence and morphological transform. Mardani *et al*. [210] developed a new system using morphological reconstruction (MR) algorithm for retinal blood vessel segmentation. Touil *et al*. [211] introduced an automatic microcalcification detection system using mathematical morphology and structural similarity indices from digitized mammograms. Chatterjee *et al*. [212] proposed a system using morphological preprocessing technique and fractal dimension for skin cancer subtype classification. Hasson *et al*. [213] used morphological operations for COVID-19 detection in chest X-ray. Halder *et al*. [214] introduced a new CADe system using the concept of adaptive morphology for lung nodule segmentation and detection. Therefore, inspiring by the previous works, in this research work, a new automated CNN framework combined with morphological operations has been developed for lung cancer subtype classification. The proposed system has used morphology-based operations to classify lung cancer subtypes from histopathology images. The morphological aspects of benign, adenocarcinoma, and squamous cell carcinoma are analyzed with the help of mathematical morphology in the context of deep learning framework. The proposed DL framework has achieved considerable classification accuracy by incorporating image morphology-based operations. In addition, attention mechanism is also incorporated for both convolution and morphology-based operations for better lung cancer subtype classification.

7.2 Research Contributions

It has been observed from literature survey that a limited number of works are performed on the LC25000 histopathology dataset for lung cancer subtype classification. Therefore, in this chapter, we have developed an automated deep-learning morphology-based framework for lung cancer subtype classification. The proposed framework with its trainable filters can learn morphological features from lung cancer histopathology images automatically. In addition, the attention mechanism is also incorporated for both convolution and morphology-based operations for better lung cancer subtype classification.

The major contributions of this research work are summarized below:

- **A morphology-based deep learning framework is introduced for lung cancer subtype classification.**
- **A novel attention-based morphological path has been designed for better classification results.**
- **Effect of attention-based morphological operations has been analyzed for lung cancer subtype classification.**
- **Proposed MorphAttnNet framework has obtained higher classification indices owing to the introduction of attention-based morphological and convolution operations.**

7.3 Dataset Details and Pre-processing

In this research work, we have validated and tested our proposed framework on publicly available LC25000 dataset [21]. The dataset contains histopathological images of lung and colon tissues. All images are taken from pathology glass slides using the procedure as described in [215] and in jpeg format. Initially, a total of 750 lung and 500 colon tissue images of dimension 1024 × 768 have been prepared for study. The lung tissue images contain 3 subclasses viz., benign, adenocarcinoma, and squamous cell carcinoma for interpretation and analysis of lung cancer. On the other hand, colon benign and adenocarcinoma are also available for cell structure analysis and subtype classification. Due to high dimension, analyses of these histopathological images are time consuming. Therefore, these images are cropped to square image of size 768 × 768 for fast processing. Next, the size of the dataset is increased by applying image augmentation techniques. Finally, the dataset contains a total of 25000 images of lung and colon cancer with 5000 images for each class. In this study, three classes of lung tissue histopathology images viz., benign, adenocarcinoma, and squamous cell carcinoma have been selected and used by the proposed framework for automatic lung cancer subtype classification.

7.4 Implementation of Attention-Based Morphology Aided Deep Learning Architecture

This section describes details of the proposed MorphAttnCNN architecture for nodule subtype classification. Figure 7.2 shows the block diagram of the proposed system. The shape and texture variations of lung subtypes have been taken into account by designing two learnable paths. It can be seen that path-1 is involved to explore features using convolution operation. On the other hand, path-2 can capture morphological variations of lung cancer subtypes by introducing morphology-based operations. Form the block diagram it can be seen that the path-1 and path-2 of the network consist of 4 layers. Let L_{1p1}, L_{2p1}, L_{3p1}, and L_{4p1} denote the layers for path-1 and L_{1p2}, L_{2p2}, L_{3p2}, and L_{4p2} denote the layers for path-2 of the network. Then merging operation on both the paths will be as follows:

$$L_m = {}_{i=1}^{4}(L_{i\,P1}) + {}_{i=1}^{4}(L_{i\,P2}) \tag{7.1}$$

where, + represent the concatenation operation and L_m is the layer obtained by concatenation operation. It can be seen that both the paths represent linear sequence; therefore, merging operation is also taking linear time. In terms of Big O notation, equation (7.1) can be written as:

$$L_m = O(M) + O(N)$$

$$L_m \simeq O(K) \tag{7.2}$$

Therefore, the proposed MorphAttnNet will run in linear time. n this work, channel wise attention mechanism has been introduced to develop attention-based blocks for both paths. Figure 7.3 shows the attention process in detail. The attention mechanism is able to find the relevant features from the histopathology lung cancer images. Therefore, in this work, relevant features are captured with the help of global contextual information obtained from extracted feature maps. In this study, two operations viz., Global Average Pooling (GAP) and Global Maximum Pooling (GMP) have been used for this purpose. The introduced GAP and GMP operations find the average and maximum values from each feature map and produce the desired feature vector. Let $\mathbf{F} \in \mathbb{R}^{w \times h \times c}$ is the output set of feature map obtained from a convolution layer. Here w, h being the width and height of individual feature map $f_i \in \mathbf{F}$ and c being the number of feature maps obtained from the

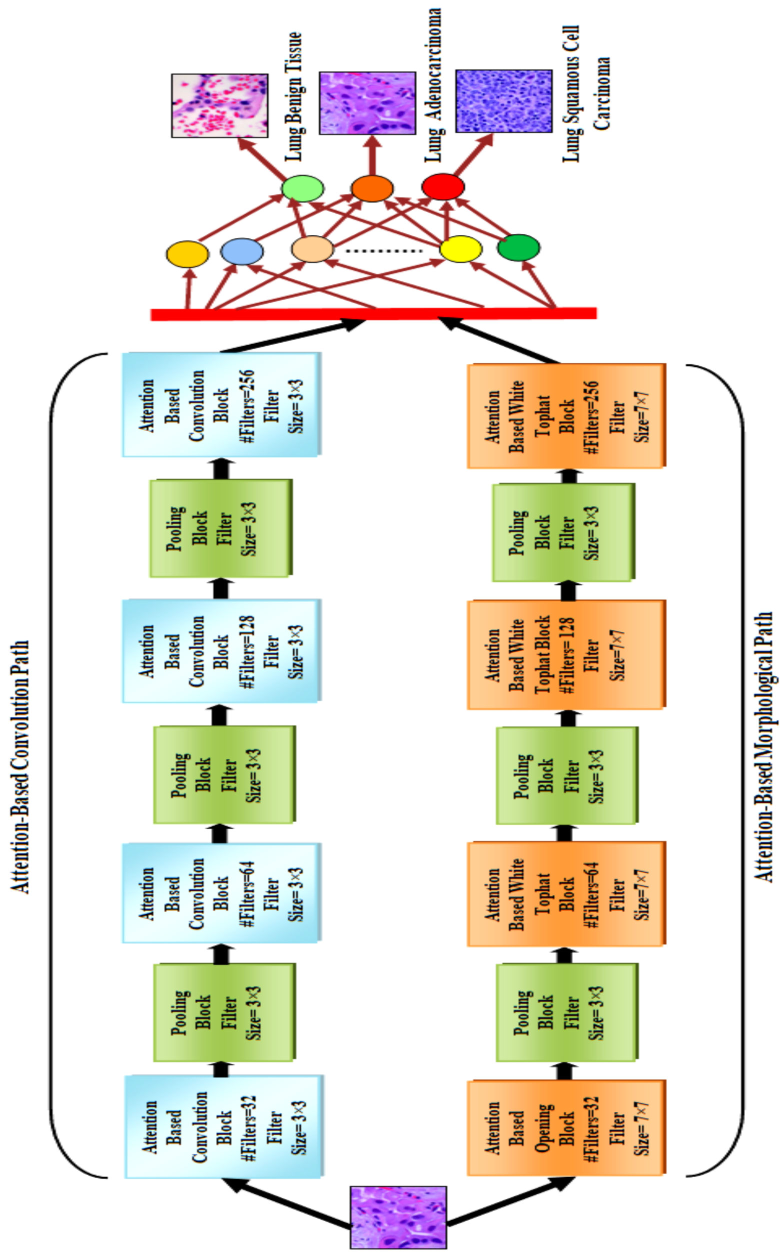

Figure7.2: Block diagram representation of the proposed MorphAttnNet.

corresponding convolution layer. Now, for every feature map f_i of $\mathbf{F} = \{f_1, f_2, ..., f_c\}$ the global average pooling operation can be defined as:

$$O_{GAP_i} = \frac{1}{N} \sum_{k=1}^{N} x_k^{f_i} \tag{7.3}$$

where, O_{GAP_i} is the scalar output of GAP operation for i^{th} feature map f_i, $x_k^{f_i}$ is the individual pixel element of f_i, and N is the dimension of the feature map set to N=w× h. Similarly, the global maximum pooling operation finds the maximum intensity pixel for feature map f_i and can be written as:

$$O_{GMP_i} = x_i \,, i = \arg\max(\vec{x}) \tag{7.4}$$

where, $\vec{x}$ is the flattened vector form of feature map f_i.Thus, in this work, GAP operation has been used to select important features and suppress less ones by employing channel-wise attention mechanism. The obtained feature vector encodes global contextual information from each channel and thus able to establish explicit relationships among channels. Similarly, in this work, GMP operation is used to extract fine grain features from the lung cancer histopathology images. The feature vector obtained by applying either GAP or GMP operation is then passed through two fully connected (FC) layers as shown in Figure 7.3.

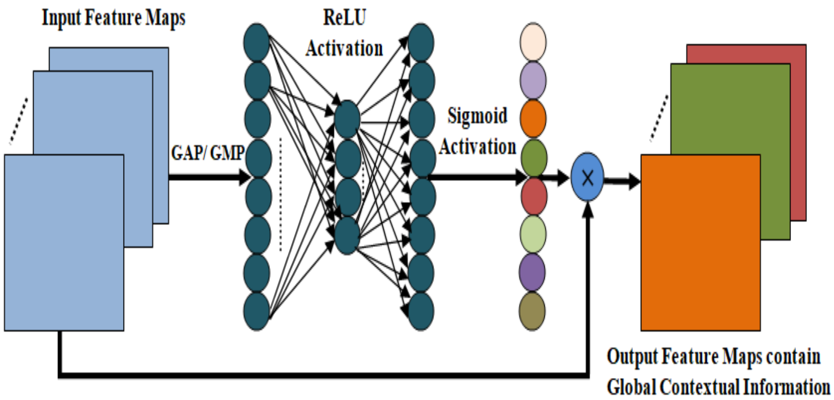

Figure7.3: Depth-wise attention mechanism using GAP/ GMP operation.

The trainable fully connected neurons of FC layers can introduce nonlinearity among the channel information. Thus with the help of the attention mechanism, the best set of features is selected that leading to the higher classification accuracy of the proposed system. The newly introduced morphology-based attention blocks are shown in Figure 7.4 (a) and (b) respectively. Figure 7.4 (a) shows the attention-based opening block that has been used in the initial layer of MorphAttnNet. The proposed attention-based opening block consists of Squeeze, Excitation, Concatenation, and Scaling modules and can extract the ROI from the background images. Initially, the extracted feature maps obtained from the opening layer are passed through the GMP and GAP blocks of the squeeze module.The output of the squeeze

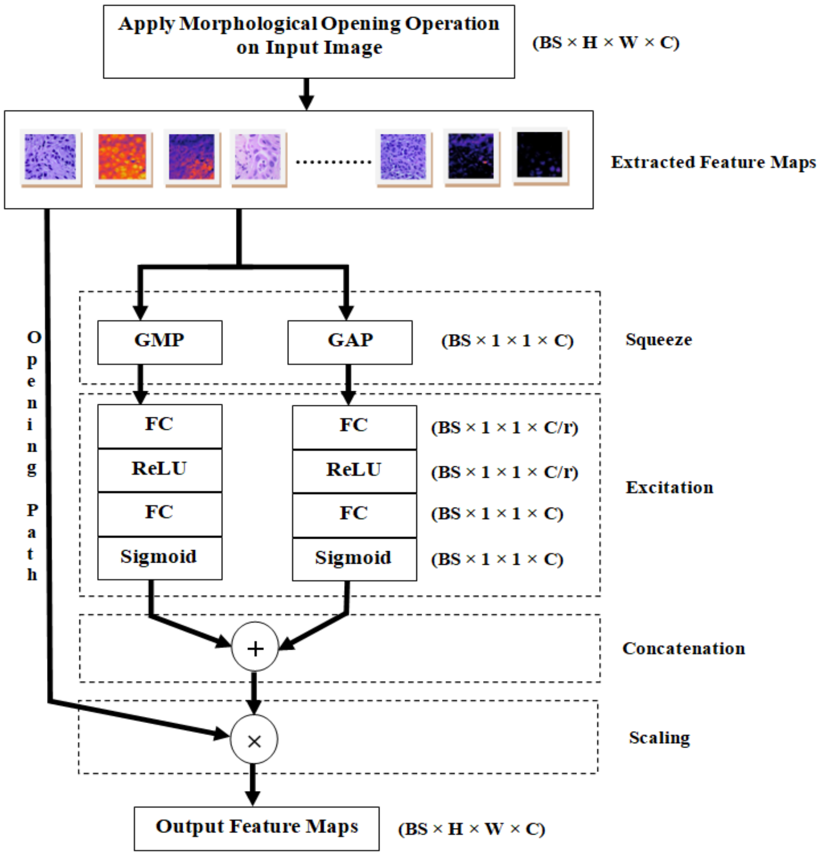

(a)

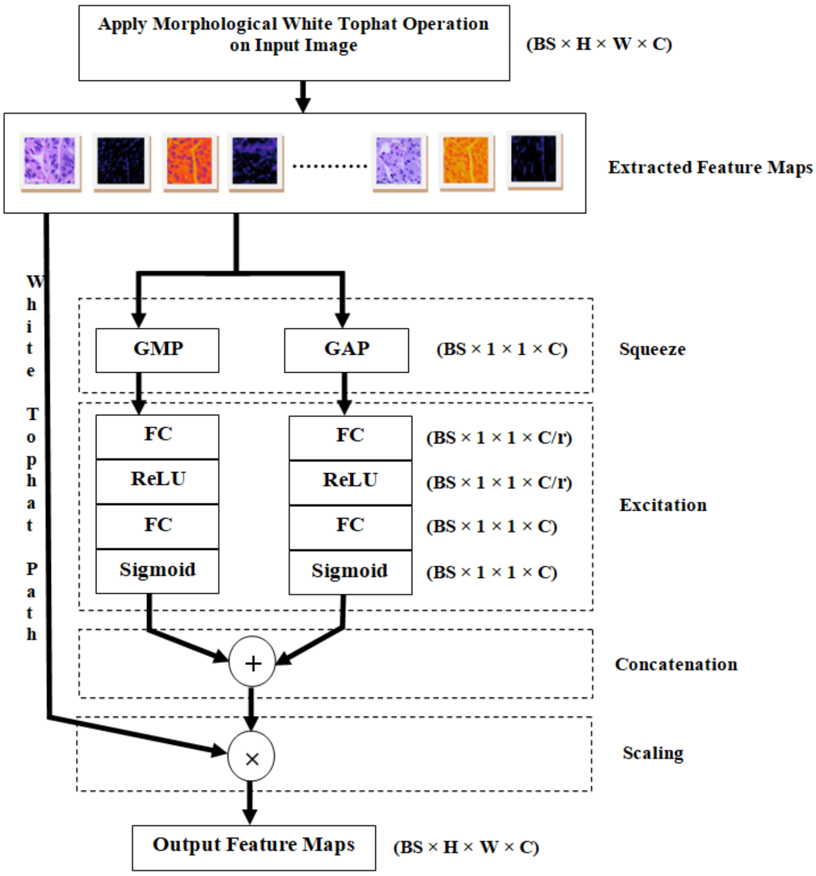

(b)

Figure7.4: Attention-based morphological blocks: (a) opening, (b) white tophat.

module is two feature vectors that are obtained by applying GMP and GAP operations on each feature map.Then the individual feature map is passed through two FC layers. The activation function ReLU has been used for the first hidden layer. Finally, a relevant feature vector is formed by applying the sigmoid activation function in the final layer. The outputs from the excitation block are then concatenated in the concatenation module. Finally, the learned weights are multiplied with the original feature maps with the help of the scaling module. The output of the attention-based opening block is the set of feature maps that contain relevant and important features of the attention-based opening operation. Similarly, in this work, attention-based white tophat operation is developed and has been used to extract fine-grain features from the lung cancer histopathology images. Figure 7.4 (b) shows the block diagram of the attention-based white tophat block. The block is the same as in Figure 7.4 (a) but instead of opening operation; morphological tophat operation has been used. Figure 7.2 shows the proposed MorphAttnNet architecture that has been developed to classify lung cancer subtypes on LC25000 dataset. The framework consists of two paths viz., path-1 and path-2 and each path consist of 4 layers. Path-1 has used attention based convolutional operation whereas blocks in path-2 have been implemented by designing attention based morphological operations. Morphological opening and white tophat operations have been used for this purpose. The feature vectors obtained from path-1 and path-2 have been concatenated by using equation (7.1). After that a two layer neural network (NN) has been implemented on the top of MorphAttnNet architecture for final classification task. The proposed MorphAttnNet can classify lung benign, adenocarcinoma, and squamous cell carcinoma, therefore, it's a multiclass classification problem. Hence, in this work, *softmax* activation function has been used to classify lung cancer subtypes. Let z_i represents the output of i^{th} neuron in the output layer of the NN. Then the expression for *softmax* activation function can be written as:

$$softmax\left(z_i\right)=\frac{exp\left(z_i\right)}{\sum_{j=1}^{3}exp\left(z_j\right)} \tag{7.5}$$

It can be observed from equation (7.5) that *softmax* function gives the probability of a data point belonging to each individual class. In this work, *softmax* activation calculates probability for three (3) classes' viz., lung benign, adenocarcinoma, and squamous cell carcinoma. Finally the MorphAttnNet predicts the final output as one of the classes that has the maximum probability. Figure 7.2 shows the proposed MorphAttnNet architecture that has used attention-based convolutional and morphological operations as its basic building block. The details of hyperparameters and the experimental set up of the network have been described in the results and analysis section. It has been observed that owing to the introduction of attention mechanisms and morphological operations, the framework can classify lung cancer subtypes with higher performance indices.

7.5 Experimental Validation and Discussion

In this section, the proposed MorphAttnNet framework is evaluated on the publicly available LC25000 histopathological dataset for lung cancer subtype classification. The system is analyzed and compared with different architectural configurations and also with a few state-of-the-art DL-based systems on the LC25000 dataset.

7.5.1 Dataset and Experimental Setup

Initially, a total of 15000 histopathology images have been taken from the LC25000 dataset. In this study, a training and validation ratio of 80:20 has been used to train the network. Apart from that another 1500 histopathology lung cancer images have been used to test the proposed system. The images are of dimension 768×768 and in jpeg format. The high dimension images will significantly affect the network training time. Therefore, in this study, all images are resized to 256×256 and have been used to train the network.

7.5.2 Performance Evaluation of the framework

In this work, four (4) different networks viz., Baseline CNN, AttnCNN, MorphCNN, MorphAttnNet have been designed and analyzed for performance comparison of lung cancer subtype classification on LC25000 dataset. Table 7.1 shows different architectures that have been designed and considered for performance comparison. Table 7.2 shows different hyper parameter values used by the frameworks. All the models have used two trainable paths viz., path-1 and path-2 that follow VGG [116]-like structure for lung cancer subtype classification. Graphical Processing Units (GPUs) available in Google Colab Pro cloud platform have been used to train and validate the networks. The frameworks have been trained for 60 epochs with a learning rate of 0.001 on publicly available LC25000 dataset.

Table 7.1: Different deep learning frameworks under analysis

Serial Number	**Architecture Used**	**Path Design Approach**
1.	Baseline CNN	Convolution operation has been used as a basic design block
2.	AttnCNN	Attention-based convolution operation has been used as a basic design block
3.	MorphCNN	Convolution and morphology-based operations have been used as basic design block
4.	MorphAttnNet	Attention-based convolution and morphological operations have been used as basic design block

Table 7.2: Different hyper parameter values used by the frameworks

Serial Number	**Model Name**	**Filter Size**	**# Trainable Filters**	**Learning Rate**	**Epochs**
1.	Baseline CNN	3×3 for Path-1 and 5×5 for Path-2	32-64-128-256 for both paths	0.001	60
2.	AttnCNN	3×3 for Path-1 and 5×5 for Path-2			
3.	MorphCNN	3×3 for Path-1 and 7×7 for Path-2			
4.	MorphAttnNet	3×3 for Path-1 and 7×7 for Path-2			

Initially, a baseline CNN is developed using only convolution operation as shown in Figure 7.5. The baseline network consists of two learnable paths. Path-1 has been used kernels of size 3×3 to learn local features. On the other hand, path-2 uses a relatively large kernel of size 5×5 to extract large features from lung cancer histopathology images. Table 7.3 shows the sensitivity, specificity, and accuracy of Baseline CNN, AttnCNN, MorphCNN, and MorphAttnNet for lung cancer subtype classification. It can be seen from Table 7.3 that the baseline CNN has achieved accuracy, sensitivity, and specificity of 89.74%, 90.85%, and 88.16% on LC25000 dataset. Next, the baseline CNN has been modified by introducing depth wise attention blocks with the help of fully connected neurons. The modified system is named as Attention-based Convolutional Neural Network (AttnCNN). Owing to the introduction of attention blocks for both paths, the framework has obtained higher accuracy, sensitivity, and specificity values of 94.12%, 94.90%, and 93.73%.

Table 7.3: Obtained performance indices of different networks on the LC25000 histopathological dataset

Sl. No.	**Architecture Under Evaluation**	**Sensitivity/ Recall (%)**	**Specificity (%)**	**Accuracy (%)**	**Precision (%)**	**F1-Score (%)**
1.	Baseline CNN	90.85	88.16	89.74	89.99	90.42
2.	AttnCNN	94.90	93.73	94.12	95.57	95.23
3.	MorphCNN	96.19	95.51	95.97	97.88	97.03
4.	MorphAttnNet	**98.33**	**97.76**	**98.04**	**99.12**	**98.72**

It can be observed from Table 7.3 that owing to the attention blocks, the AttnCNN framework has achieved 4.38% increase in accuracy over baseline CNN for lung subtype classification.

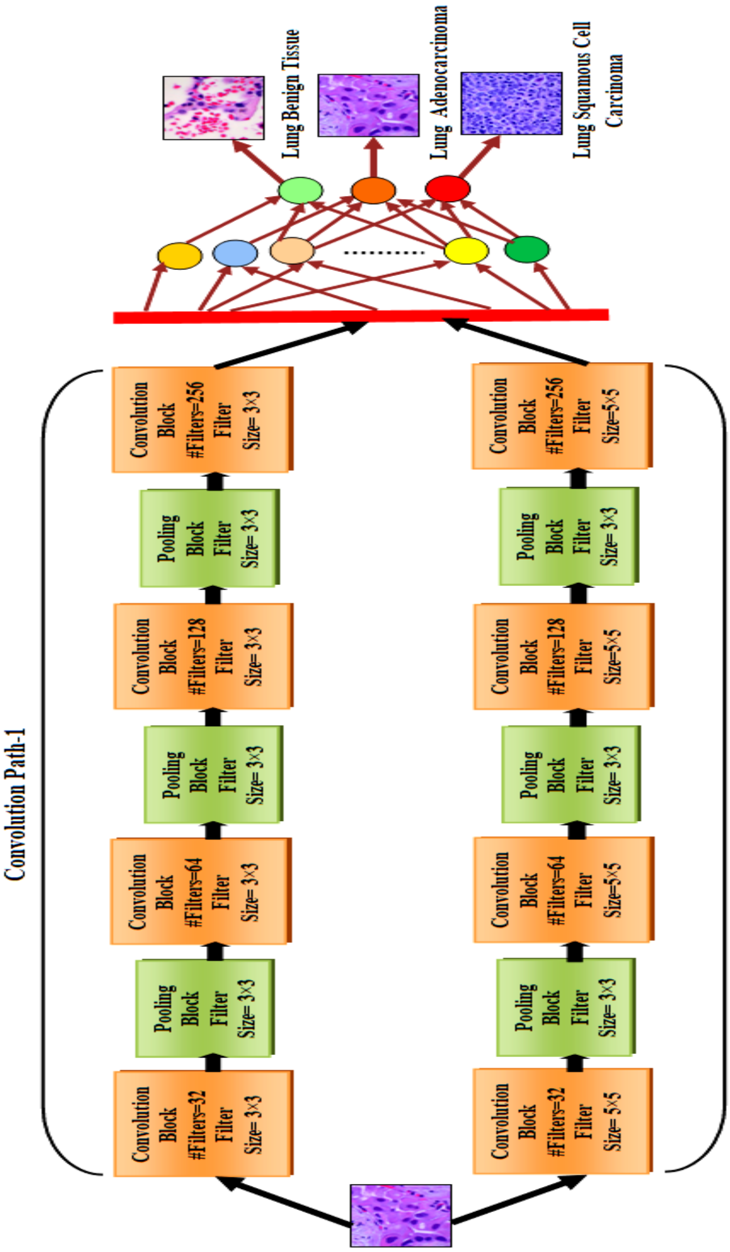

Figure7.5: Baseline CNN framework using only convolution operation.

Image morphology plays an important role for accurate ROI segmentation and recognition. Lung cancer tissue images have shown structural similarity for three (3) subclasses viz., benign, adenocarcinoma, and squamous cell carcinoma. Therefore, sometimes it is difficult to classify them to their true class. In this work, morphology-based operations have been introduced to capture true structural variations of lung cancer subtypes. The morphological filters have been learned automatically from the given target histopathology lung cancer images. In this new context, convolution operation of path-2 of the AttnCNN network is replaced by morphology-based operations. The modified architecture is named as Morphology-based Convolutional Neural Network (MorphCNN) and evaluated on LC25000 dataset for lung cancer subtype classification. The paths of the framework are designed in such a way that it can capture morphological properties of lung cancer tissues. Morphological opening operation has been used in the initial layer to detach the lung cancer cells from the background. The opening layer is followed by white tophat layers that are able to extract fine grain features from the histopathology images for better subtype classification. The MorphCNN framework has used kernels of size 3×3 and 7×7 for convolutional and morphology-based paths respectively. The MorphCNN framework achieved sensitivity, accuracy, and specificity of 96.19%, 95.97%, and 95.51%, respectively on LC25000 dataset. Finally, the proposed Morphology-based Attention Network (MorphAttnNet) has been developed by incorporating attention-based blocks for morphological operations. The attention mechanism selects the most relevant morphological features using layer wise fully connected neurons. Thus the proposed MorphAttnNet with its attention blocks is able to capture true shape variations of lung benign, adenocarcinoma, and squamous cell carcinoma from histopathological images. Both the MorphCNN and proposed MorphAttnNet are initialized with circular like 7×7 filters that act as structuring elements for subsequent morphological operations. A total of 3,092,887 parameters are learned by the proposed MorphAttnNet framework. From Table 7.3, it is seen that the proposed MorphAttnNet framework achieved sensitivity, specificity, and accuracy of 98.33%, 97.76%, and 98.04% on LC25000 dataset. It has also been observed that due to the introduction of attention-based morphology blocks, the framework has obtained highest classification accuracy of 98.04%. Figure 7.6 (a), (b), and (c) show the training and validation loss, accuracy and ROC curve of the proposed MorphAttnNet on LC25000 lung cancer subtype dataset. The model has run for 60 epochs.

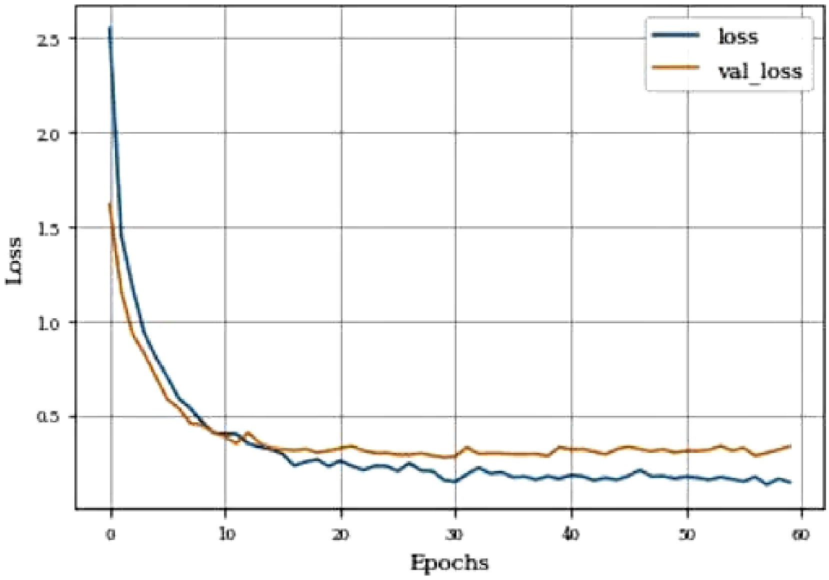
loss
val_loss
Loss
2.5
2.0
1.5
1.0
0.5
0
10
20
30
40
50
60
Epochs

(a)

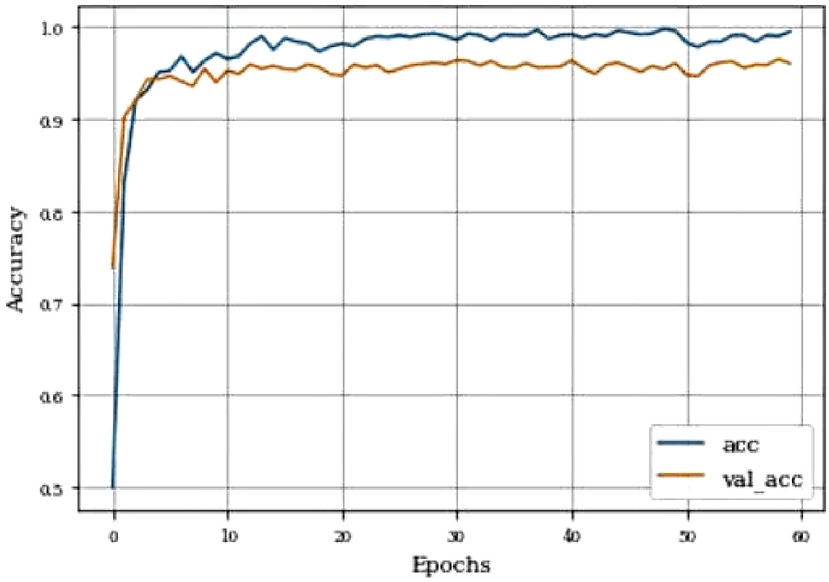
acc
val_acc
Accuracy
1.0
0.9
0.8
0.7
0.6
0.5
0
10
20
30
40
50
60
Epochs

(b)

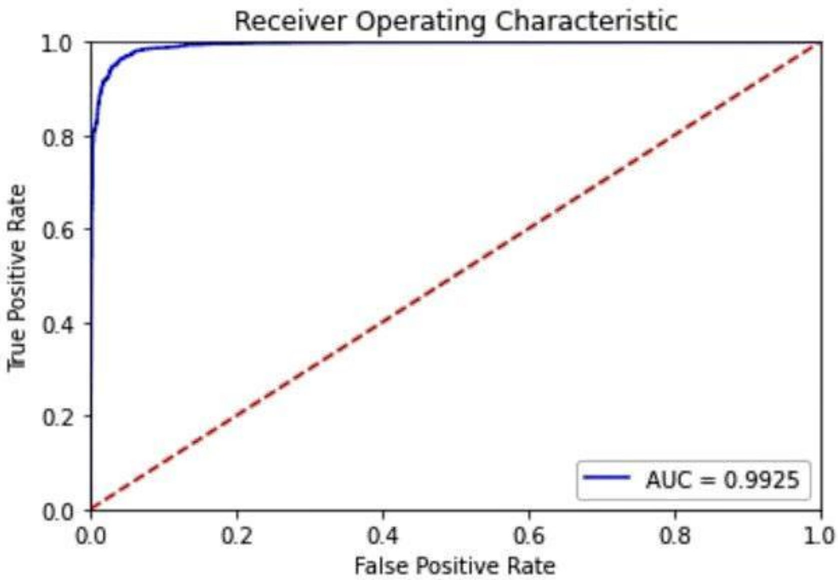

(c)

Figure7.6: Different performance metrics of MorphAttnNet on training set and validation set in LC25000 dataset a) Loss b) Accuracy and c) ROC Curve.

Figure 7.7 shows the accuracy comparison graph of four (4) models viz., Baseline CNN, AttnCNN, MorphCNN, and MorphAttnNet obtained with a training and validation ratio of 80:20 on LC25000 dataset. It is seen that the proposed MorphAttnNet framework has outperformed other models under consideration and achieved classification accuracy of above 98%. The precision and f1-score also have been computed for all the models under consideration. It has been observed from Table 7.3 that the proposed MorphAttnNet framework has obtained highest precision and f1-score of 99.12% and 98.72% respectively for lung cancer subtype classification. Apart from sensitivity, specificity, accuracy, precision, and f1-score, the performance of the proposed MorphAttnNet has also been analyzed using K-fold cross validation technique where, K is chosen as 3, 5, and 10. Average accuracy of the proposed model has been computed on LC25000 lung cancer subtype dataset. The obtained results have been shown in Table 7.4. It can be observed from Table 7.4 that the proposed MorphAttnNet obtained highest average classification accuracy of 98.96% for K value 10.

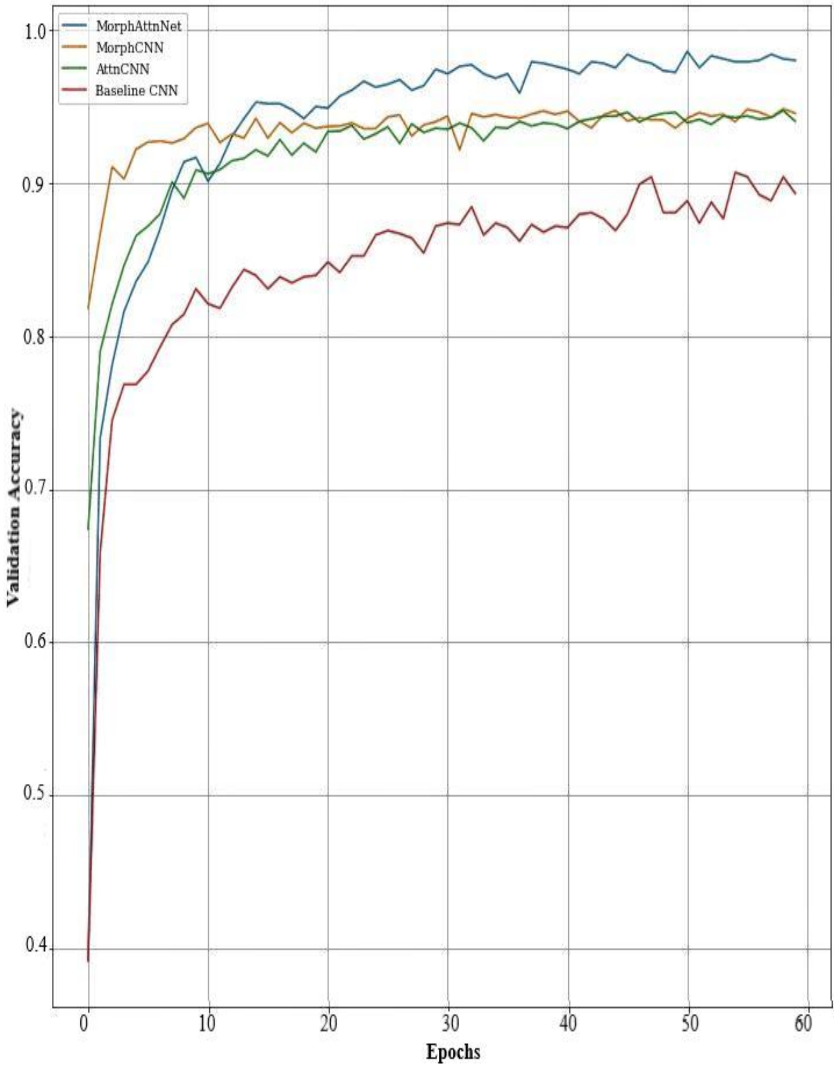

Figure 7.7: Accuracy comparison graph of Baseline CNN, AttnCNN, MorphCNN, and MorphAttnNet on LC25000 dataset.

Table 7.4: Mean accuracy obtained by MorphAttnNet using K-fold cross validation technique

K-fold Cross Validation	Obtained Mean Accuracy (%)±σ
K=3	97.21±0.013
K=5	98.02±0.017
K=10	**98.96±0.010**

Next, the performance of the proposed MorphAttnNet is compared with existing DL-based frameworks for lung cancer subtype classification. Table 7.5 shows the obtained accuracies by different networks. It can be seen that the existing VGG-16 [116], VGG-19 [216], and ResNet-50 [119] models have obtained classification accuracies of 83.64%, 87.20%, and 90.72%, respectively on the LC25000 lung cancer subtype dataset. The MorphAttnNet framework outperforms existing state-of-the-art deep learning models and obtained highest classification accuracy of 98.04% for lung cancer subtype classification. Figure 7.8 shows the validation accuracy of different models on LC25000 dataset partitioned into 80:20 ratios for training and validation set. It has been observed that the proposed MorphAttnNet has obtained highest classification accuracy as compared to other state-of-the-art frameworks.

Table 7.5: Obtained accuracy by different state-of-the-art deep learning frameworks on LC25000 dataset

DL Framework	Obtained Accuracy
VGG-16 [116]	83.64%
VGG-19 [216]	87.20%
ResNet-50[119]	90.72%
Proposed MorphAttnNet	**98.04%**

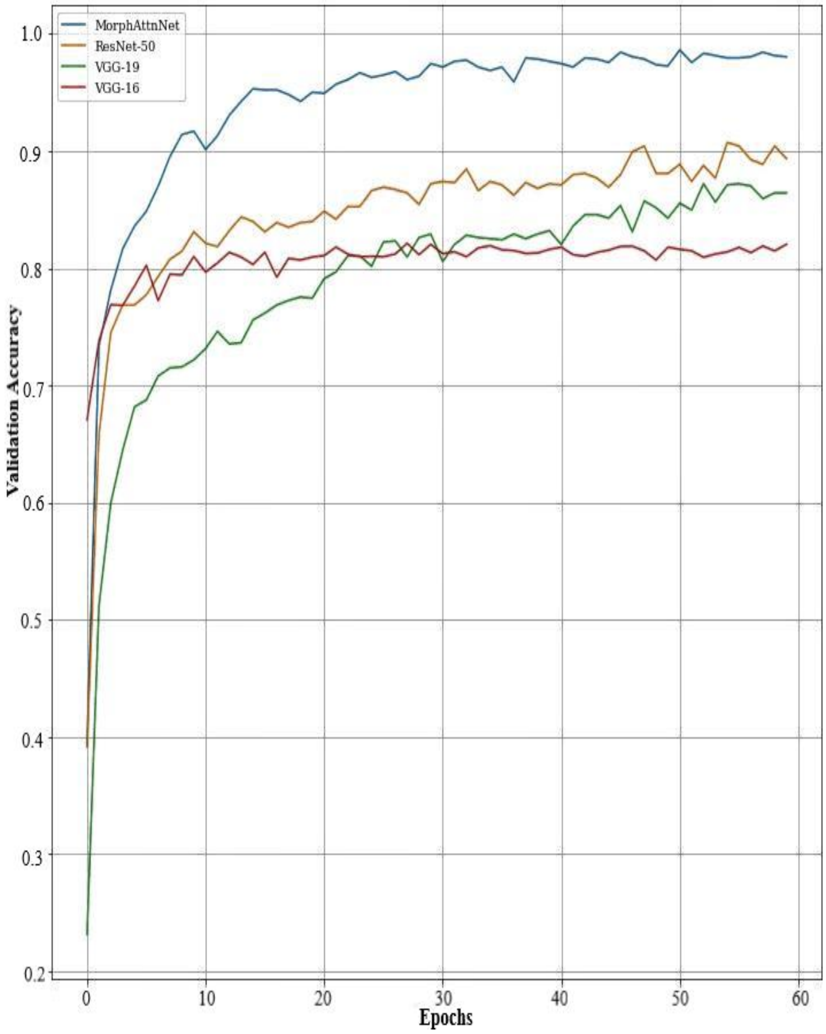

Figure 7.8: Accuracy comparison graph of VGG-16, VGG-19, ResNet-50, and MorphAttnNet on LC25000 dataset.

After that, the performance of the framework also has been compared with different state-of-the-art works for lung cancer subtype classification. It has been observed that different Machine Learning (ML)-based methods exist in literature for object segmentation [217, 218, 219, 220, 221] and detection [202, 203, 204, 212, 213, 214]. Dakua *et al*. [217] introduced a new methodology for left ventricle (LV) segmentation in cardiac magnetic resonance (CMR) image using cantilever beam deflection and random walk approach. In [219] authors have developed a ML-based system by combining random walk and active contour model for detection of myocardial walls of LV in ischemic CMR images. A new technique based on principal component analysis (PCA) has been developed in [220] for brain aneurysm segmentation. Authors have achieved a dice score of 94.1±1.2 for aneurysm segmentation. In [221] a liver segmentation method has been introduced using stochastic resonance and cellular automata. It has been observed that various ML-based techniques have produced impressive segmentation and classification accuracy for pathology detection and medical image segmentation. But finding appropriate methods and relevant features is a challenging task. Recently with the availability of modern systems and advanced hardware, deep learning (DL)-based frameworks are in widely used for object segmentation and detection [25, 222]. DL-based frameworks can automatically extract relevant features with the help of trainable filters. Therefore, in this work; a new deep learning framework has been developed for lung cancer subtype classification. The performance of the framework (MorphAttnNet) is compared with existing state-of-the-art DL-based works. Hatuwal*et al*. [223] proposed a CNN-based DL model for lung cancer subtype classification. The model has used kernels and max pooling layers of size 3×3 and 2×2 respectively. Finally, in the output layer authors have used categorical cross-entropy (CE) function to classify three lung cancer subtypes viz., lung benign, adenocarcinoma, and squamous cell carcinoma. The developed system has achieved an accuracy of 97.20% on LC25000 dataset. Mangal *et al*. [224] developed a new CNN architecture for lung cancer subtype classification. The five (5)-layered CNN has used kernels of size 3×3 for automatic feature extraction. The model was trained for 100 iterations and obtained an accuracy of 97.89% on LC25000 dataset. Rahman *et al*. [225] developed a new cloud-based smart detection framework for COVID-19 detection. The developed system has obtained a detection accuracy of 98.4% with 15-fold cross-validation strategy. In this work, the proposed cloud-based framework by Rahman *et al*. [225] has been incorporated and applied for lung cancer subtype classification on LC25000 dataset. Table 7.6 shows the accuracies obtained by different state-of-the-art works along with the proposed MorphAttnNet model.

Table 7.6: Performance comparison of different deep learning-based systems on LC25000 dataset

Deep Learning-based Works	**Accuracy**
Hatuwal *et al*. [223]	97.20%
Mangal *et al*. [224]	97.89%
Rahman *et al*. [225]	98.03%
Proposed MorphAttnNet	**98.96%**

It can be observed that owing to the introduction of attention-based blocks and morphological operations inside the framework, the proposed model obtained highest classification accuracy of 98.96% for lung cancer subtype classification.

7.5.3 Discussion

In this chapter, a new automated deep learning-based system has been developed employing the concept of image morphology.The proposed *Morph*ology-based *Atten*tion *Net*work, (MorphAttnNet) can classify benign, ADC, and SCC from histopathology images. The framework is designed based on convolution and morphological operations. An attention-based mechanism is incorporated to select important features from histopathology images. The framework with its morphology-based path combined with attention blocks can capture morphological variations of lung cancer subtypes accurately and effectively. Finally, the extracted deep features from convolution and morphological paths are combined and used for lung cancer subtype classification. The performance of the proposed framework is analyzed on the publicly available LC25000 dataset and achieved an accuracy of 98.96%.

7.6 Summary

In this reported work, we have developed a new deep learning framework for lung cancer subtype classification. The proposed MorphAttnNet with its two trainable paths is able to classify lung cancer subtypes from histopathological images effectively. Attention-based mechanism has been introduced for this purpose. The proposed attention block finds global features from the feature maps and combines them with the locally extracted convolution features with the help of Squeeze, Excitation, Concatenation, Scaling modules. This strategy helps the MorphAttnNet to select the relevant features from the feature maps by utilizing channel wise global information. Thus the shape and texture variations of lung subtypes have been taken into account by designing two learnable paths. The path-1 of the network is involved to extract features using convolution operation. On the other hand, path-2 can capture morphological variations of lung cancer subtypes by introducing morphology-based operations. The introduced attention-based block has been used for both paths. The proposed MorphAttnNet has obtained sensitivity, specificity, and average accuracy of 98.33%, 97.76%, and 98.96%, respectively on LC25000 dataset for lung cancer subtype classification. It has been observed experimentally that as compared to other systems, the proposed MorphAttnNet can classify lung cancer subtypes with higher accuracy value. This is achieved by introducing morphological operations and attention-based blocks inside the network. Thus by combining the morphological features and global contextual information the MorphAttnNet has outperformed other DL-based systems. Therefore, the proposed framework may act as a second opinion for doctors and pathologists to take their valuable decisions for lung cancer subtype classification.

- **Publication:**

Amitava Halder and Debangshu Dey, “MorphAttnnet: An Attention -based Morphology Framework for Lung Cancer Subtype Classification,” in *Biomedical Signal Processing and Control, Elsevier,* (Impact Factor: 5.10), vol. 86, 105149, June 2023, doi: 10.1016/j.bspc.2023.105149.

Chapter 8

Conclusions and Future Scopes

8.1 Conclusions

Lung cancer is one of the leading causes of death and the fastest growing cancer all over the world. In this dissertation, attempts have been made to design and development of CAD-based frameworks for lung nodule detection, characterization, and lung cancer subtype classification using machine learning and deep learning techniques. In this research work, morphology-based image processing techniques have been applied extensively for accurate segmentation, detection, and characterization of lung nodules in HRCT images. The developed systems can assist the radiologists and doctors for early detection and characterization of lung cancer. Apart from that a new framework also has been developed for lung cancer subtype classification in histopathology images to assist the pathologists. The contributions of this thesis work are enumerated as follows:

- Chapter 2 introduces a new CADe framework for lung nodule detection using clustering approach. The concept of superpixel has been used for lung internal structure segmentation. Then the segmented regions are refined using proposed Superpixel and Density Based Region (SPDBR) segmentation algorithm. Finally, different morphology-based features have been used for nodule detection. The major findings are listed as follows:
    - i. A new nodule detection system has been introduced based on the concept of superpixel.
    - ii. A new superpixel-based segmentation algorithm has been developed for accurate nodule segmentation.
    - iii. Morphological features have been used by the framework for nodule detection.

- Chapter 3 introduces a new CADe system for lung nodule detection with the help of morphological operations. GMM based segmentation technique has been used for internal lung region segmentation. Nodule candidates are detected with the help of proposed morphological filter. The major outcomes are listed below:

i. In this chapter a new nodule detection framework has been developed using image morphology.
ii. Gaussian Mixture Model (GMM) has been introduced for finer structure extraction inside the lung regions.
structure extraction inside the lung regions.
iii. A new morphology-based filter has been introduced for false positive reduction and accurate nodule detection.
iv. Different shape and intensity-based features have been used by the system for better nodule detection.

- Chapter 4 illustrates the concept of adaptive morphology for lung nodule detection. In this work adaptive morphology-based operations have been introduced for lung and nodule segmentation. The candidate nodules have been detected with the help of proposed adaptive bottom-hat (ABHT) filter. The major contributions are listed below:
  i. An improved lung segmentation algorithm is presented employing image morphology-based operations.
  ii. Considering the morphological and deformable properties of the lung nodules, adaptive structuring elements have been introduced for the development of morphological filters.
  iii. Grayscale adaptive morphological filters are developed for the segmentation and detection of large varieties of candidate nodules.
  iv. Different shape, intensity, and texture-based features have been used by the framework for lung nodule detection using HRCT lung images.

- Chapter 5 discusses an automated integrated deep learning framework for lung nodule characterization. Concept of multi-scale feature combined with attention mechanism has been used for accurate nodule segmentation and characterization. The primary findings of this work are written below:
  i. An integrated DL framework has been developed for lung nodule segmentation and characterization.
  ii. A new framework based on atrous convolution has been introduced.

iii. A novel attention-based mechanism has been incorporated for better nodule segmentation.
iv. Multi-scale features have been captured to classify lung nodule.
v. Residual connections have been introduced for better feature preservation.
vi. The proposed segmentation framework has been compared with existing state-of-the-art segmentation frameworks.

- Chapter 6 discusses an end-to-end deep learning framework employing morphological operations for lung nodule characterization. The basic building blocks of the framework have used convolution and image morphology-based operations. Apart from that two new weight initialization algorithms have been proposed for better results of the system. The main contributions are as follows:
  i. An improvised CNN model combined with morphological operations has been developed for lung nodule characterization.
  ii. An Adaptive morphology-based weight initialization scheme has been introduced to capture deformable properties of lung nodule.
  iii. A Gabor filter-based weight initialization scheme has been developed to capture textural information from nodule region.
  iv. Morphological and textural features are combined using two trainable parallel paths of the CNN model for improved classification of pulmonary nodules.

- Chapter 7 introduces a deep learning framework using morphological operations and attention mechanism for lung cancer subtype classification. The primary outcomes are listed as follows:
  i. A new deep learning framework has been developed using image morphology for lung cancer subtype classification.
  ii. Attention mechanism has been incorporated for accurate lung cancer subtype classification.
  iii. The effect of attention-based morphological operations has been analysed for lung cancer subtype classification.
  iv. The proposed framework has been compared with state-of-the-art frameworks for lung cancer subtype classification.

8.2 Future Scopes

The results presented in this dissertation can provide a basis for further research in early detection of lung cancer. Despite several published research works are available, there is no single strategy that is perfect for most of the CAD-based systems. There is always a scope for further improvement in the early detection and diagnosis of lung cancer by considering some challenging cases in the future study. Although in this thesis work, different image processing and deep learning-based algorithms have been developed with the help of morphological operations for the development of automated lung cancer diagnose system; research can be conducted for further improvement of early detection of lung cancer with the help of new technologies. Therefore, cconsidering the advancement in medical image processing techniques, some of the future scopes of research have been mentioned below:

- In this thesis work focuses have been given to detection, characterization, and classification of lung cancer. Automatic gradation and staging of lung cancer can help doctors to make proper treatment planning and may improve the overall treatment process; which in turn can increase the five year survival rate of lung cancer patients. Therefore, in future, works will be conducted to determine the cancer grade using machine learning and deep learning techniques.

- Medical image processing techniques play a vital role for different disease detection and characterization. In this thesis work, focuses have been given to capture morphological properties of lung cancer. Different machine learning and deep learning based systems have been developed that can extract morphological features from the HRCT images for detection and characterization of lung nodules. In the near future systems will be developed to detect and characterize different cancers e.g., breast, prostate, colon cancer etc. with the help of recently developed deep learning frameworks. The effect of different morphological operations will also be analyzed for the early detection and diagnosis of different cancers for the benefit of society.

References

[1] World Health Organization. [Online] http://www.who.int/en/. Accessed 05 Jan. 2023.

[2] Global Cancer Observatory. [Online] http://gco.iarc.fr/. Accessed 10 Jan. 2023.

[3] C.S. Dela Cruz, L.T. Tanoue and R.A. Matthay, “Lung cancer: epidemiology, etiology, and prevention,” *Clin. Chest Med*., vol. 32, no. 4, pp. 605–644, Dec. 2011.

[4] L. Abid, “Lung cancer around the world and Arab countries,” AMAAC Workshop, Algiers 2011.

[5] American Cancer Society (ACS). [Online] https://www.cancer.org/. Accessed10 Jan. 2023.

[6] National Cancer Centre Singapore. [Online] https://www.nccs.com.sg/Pages/Home.aspx/. Accessed 12 Jan. 2023.

[7] National Cancer Institute (INCA). [Online] https://www.inca.gov.br/. Accessed 14 Jan. 2023.

[8] Fleischner Society. [Online] https://fleischner.memberclicks.net/. Accessed 20 Jan. 2023.

[9] W.J. Kostis, A.P. Reeves, D.F. Yankelevitz and C.I. Henschke, “Three dimensional segmentation and growth-rate estimation of small pulmonary nodules in helical CT images,” *IEEE Trans. Med. Imaging*, vol. 22, no. 10, pp.1259–1274, Oct. 2003.

[10] H. MacMahon *et al*., “Guidelines for management of small pulmonary nodules detected on CT scans: a statement from the Fleischner Society,” *Radiology*, vol. 237, no. 2, pp. 395–400, Nov. 2005.

[11] M. Lederlin, M-P. Revel, A. Khalil, G. Ferretti, B. Milleron and F. Laurent, “Management strategy of pulmonary nodule in 2013,” Diagn. Interv. Imaging, vol. 94, no. 11, pp. 1081–1094, Nov. 2013.

[12] O. Rena, F. Davoli, R. Boldorini, A. Roncon, G. Baietto, E. Papalia, D. Turello, F. Massera and C. Casadio, “The solitary pulmonary nodule in patients with previous cancer history: results of surgical treatment,” *Eur. J. Surg. Oncol*., vol. 39, no., pp. 1248–1253, Nov. 2013.

[13] A.K. Attili and E.A. Kazerooni, “Imaging of the solitary pulmonary nodule,” in *Evidence-Based Imaging*, New York, USA: Springer, 2006.

[14] S. Brandman and J.P. Ko, “Pulmonary nodule detection, characterization, and management with multi detector computed tomography,” *J. Thorac. Imaging*, vol. 26, no. 2, pp. 90–105, 2011.

[15] B. de Hoop, H. Gietema, S. V. de Vorst, K. Murphy, R. J. van Klaveren and M. Prokop, “Pulmonary ground-glass nodules: increase in mass as an early indicator of growth,” *Radiology*, vol. 255, no. 1, pp. 199–206, Apr. 2010.

[16] A. K. Dhara, S. Mukhopadhyay and N. Khandelwal, “Computer-aided detection and analysis of pulmonary nodule from CT images: a survey,” *Technical Review IETE,* vol. 29, no. 4, pp. 265-275, Sept. 2012.

[17] Z. Smith *et al*., “Strategies for the Management of Solitary Pulmonary Nodules: A Survey of Patient Preferences,” *Ann. Thorac. Surg*., vol. 113, no. 5, pp. 1670–1675, May 2021.

[18] http://www.wikipedia.org/.Accessed 14Feb. 2023.

[19] National Lung Screening Trial (NLST). [Online] https://www.cancer.gov/types/lung/research/nlst/. Accessed 14Feb. 2023.

[20] Dataset] LIDC-IDRI. https://wiki.cancerimagingarchive.net/display/

/Public/LIDC-IDRI.Accessed 14Feb. 2023.

[21] [Dataset] LC25000. https://www.kaggle.com/datasets/andrewmvd/lung-and-colon-cancer-histopathological-images. Accessed 14Feb. 2023.

[22] I. Sluimer, A. Schilham, M. Prokop and B. van Ginneken, “Computer analysis of computer tomography scan of the lung: a survey,” *IEEE Trans. Med. Imaging*, vol. 25, no. 4, pp. 385–405, Apr. 2006.

[23] S.L.A. Lee, A. Z. Kouzani and E. J. Hu, "Automated detection of lung nodules in computed tomography images: a review," *Mach. Vision Appl*., vol. 23, no. 1, pp. 151–163, May 2010.

[24] N. Lee, A. F. Laine, G. Mrquez, J. M. Levsky and J. K. Gohagan, "Potential of computer-aided diagnosis to improve CT lung cancer screening," *IEEE Rev. Biomed. Eng.*, vol. 2, pp. 136–146, 2009.

[25] A. Halder, D. Dey and A.K. Sadhu, Lung Nodule Detection from Feature Engineering to Deep Learning in Thoracic CT Images: a Comprehensive Review, *J. Digit. Imaging*, vol. 33, no. 3, pp. 655–677, Jan. 2020.

[26] J.R.F. de Silve Sousa, A.C. Silva, A.C. de Paiva and R.A. Nunes, " Methodology for automatic detection of lung nodules in computerized tomography images," *Comput. Methods Programs Biomed.*, vol. 98, no. 1, pp. 1–14, Aug. 2009.

[27] T. Messay, R.C. Hardie and S.K. Rogers, "A new computationally efficient CAD system for pulmonary nodule detection in CT imagery," *Med. Image Anal*., vol. 14, no. 3, pp. 390-406, Feb. 2010.

[28] W.J. Choi and T.S. Choi, "False positive reduction for pulmonary nodule detection using two- dimensional principal component analysis," in *Proc. SPIE App. Digit. Imaging Processing*, Sept. 2009, 12.827252.

[29] G. Aresta, A. Cunha and A. Campilho, "Detection of juxta-pleural lung nodules in computed tomography images," in *Proc. SPIE Med. Imaging,* Mar. 2017, 12.2252022.

[30] S.A. Mehre *et al*., "An automated lung nodule detection system for CT images using synthetic minority oversampling," in *Proc. SPIE Med. Imaging*, Mar. 2016, 12.2216357.

[31] W-J. Choi and T-S Choi, "Genetic programming-based feature transformand classification for the automatic detection of pulmonary noduleson computed tomography images," *Inf. Sci*., vol. 212, pp. 57–78, May 2012.

[32] J.J. Suárez-Cuenca, W. Guo and Q. Li, “Automated detection of pulmonary nodules In CT: false positive reduction by combining multiple classifiers,” in *Proc. SPIE Med. Imaging*, Mar. 2011, 12.878793.

[33] A.O. de Carvalho Filho *et al.*, “Automatic detection of Solitary lung nodules using quality threshold clustering, genetic algorithm and diversity index,” *Artif. Intell. Med.*, vol. 60, no. 3, pp. 165–177, Nov. 2013.

[34] M. Javaid, M. Javid, M.Z. Ur Rehman and S.I.A. Shah, “A novel approach to CAD system for the detection of lung nodules in CT images,” *Comput. Methods Programs Biomed.*, vol. 135, pp. 125–139, July 2016.

[35] E.E. Nithila and S.S. Kumar, “Automatic detection of solitary pulmonary nodules using swarm intelligence optimized neural networks on CT images,” *Eng. Sci. Technol. Int. J.*, vol. 20, no. 3, pp. 1192–1202, Dec. 2016.

[36] F.V. Farahani, A. Ahmadi and M.H.F. Zarandi, “Hybrid intelligent approach for diagnosis of the lung nodule from CT images using spatial kernelized fuzzy c-means and ensemble learning,” *Math. Comput. Simul*., vol. 149, pp. 48–68, Feb. 2018.

[37] S.M.B. Netto, A.C. Silva, R.A. Nunes and M. Gattass, “Automatic segmentation of lung nodules with growing neural gas and support vector machine,” *Comput. Biol. Med*., vol. 42, no. 11, pp. 1110–1121, Sept. 2012.

[38] R. Hosseini, S.D. Qanadli, S. Barman, M. Mazinani, T. Ellis and J. Dehmeshki, “An automatic approach for learning and tuning Gaussian interval type-2 fuzzy membership functions applied to lung CAD classification system, ” *IEEE Trans. Fuzzy Syst*., vol. 20, no. 2, pp. 224–234, Oct. 2011.

[39] M. Keshani, Z. Azimifar, F. Tajeripour and R. Boostani, "Lung nodule segmentation and recognition using SVM classifier and active contour modeling: a complete intelligent system," *Comput. Biol. Med.*, vol. 43, no. 4, pp. 287–300, Jan. 2013.

[40] J. Gong, J-Y. Liu, L-J.Wang, X-W. Sun, B. Zheng and S-D. Nie, "Automatic detection of pulmonary nodules in CT images by incorporating 3D tensor filtering with local image feature analysis," *Physica Med*., vol. 46, pp. 124–133, Feb. 2018.

[41] T. McInerney and D. Terzopoulos, "Deformable models in medical image analysis: a survey," *Med. Image Anal*., vol. 1, no. 2, pp. 91–108, Apr. 2002.

[42] D. Cascio, R. Magro, F. Fauci, M. Iacomi and G. Raso, "Automatic detection of lung nodules in CT datasets based on stable 3D mass spring models," *Comput. Biol. Med*., vol. 42, no. 11, pp. 1098–1109, Sept. 2012.

[43] M. Alam, G. Sankaranarayanan and V. Devarajan, "Lung nodule detection and segmentation using a patch-based multi-atlas method," in *IEEE Int. Conf. Comput. Sci. Comput. Intell. (CSCI)*, Dec. 2016, pp 23–28.

[44] J. Gong, J-Y. Liu, L-J. Wang, B. Zheng and S-D. Nie, "Computer-aided detection of pulmonary nodules using dynamic self-adaptive template matching and a FLDA classifier," *Physica Med.*, vol. 32, no. 12, pp. 1502–1509, Nov. 2016.

[45] A. Farag, A. Ali, J. Graham, A. Farag, S. Elshazly and R. Falk, "Evaluation of geometric feature descriptors for detection and classification of lung nodules in low dose CT scans of the chest," in *IEEE Int. Symp. Biomed. Imaging: From Nano to Macro*, Mar.-Apr. 2011, pp 169–172.

[46] M. Assefa, I. Faye, A.S. Malik and M. Shoaib, "Lung nodule detectionusing multi- resolution analysis," in *IEEE Int. Conf. Complex Med. Eng. (ICME)*, May 2013, pp 457–461.

[47] W-J. Choi and T-S. Choi, “Automated pulmonary nodule detection based on three-dimensional shape- based feature descriptor,” *Comput. Methods Programs Biomed*., vol. 113, no. 1, pp. 37–54, Sept. 2013.

[48] M.A. Jaffar, A.B. Siddiqui and M. Mushtaq, “Ensemble classification of pulmonary nodules using gradient intensity feature descriptor and differential evolution,” *Cluster Comput*., vol. 21, no. 1, pp. 393–407, Apr. 2017.

[49] A. Retico *et al*., “A voxel-based neural approach (VBNA) to identify lung nodules in the ANODE09 study,” in *Proc. SPIE Med. Imaging*, Mar. 2009, 12.811721.

[50] G. Litjens *et al*., “A survey on deep learning in medical image analysis,” *Med. Image Anal*., vol. 42, pp. 60–88, July 2017.

[51] A.A.A. Setio *et al.*, “Pulmonary nodule detection in CT images: false positive reduction using multi-view convolutional networks,” *IEEE Trans. Med. Imaging*., vol. 35, no. 5, pp. 1160–1169, May 2016.

[52] F. Ciompi *et al*., “Automatic classification of pulmonary peri-fissural nodules in computed tomography using an ensemble of 2D views and a convolutional neural network out-of-the-box,” *Med. Image Anal*., vol. 26, no. 1, pp. 195–202, Sept. 2015.

[53] W. Shen *et al*., “Multi- crop convolutional neural networks for lung nodule malignancy suspiciousness classification,” *Pattern Recognit*., vol. 61, pp. 663–673, May 2016.

[54] Q. Dou, H. Chen, L. Yu, J. Qin and P.-A. Heng, “Multilevel contextual 3-DCNNs for false positive reduction in pulmonary nodule detection,” *IEEE Trans. Biomed. Eng*., vol. 64, no. 7, pp. 1558–1567, Sept. 2016.

[55] S. Wang *et al*., “Central focused convolutional neural networks: developing a data-driven model for lung nodule segmentation,” *Med. Image Anal*., vol. 40, pp. 172–183, June 2017.

[56] J. Yuan, X. Liu, F. Hou, H. Qin and A. Hao, “Hybrid-feature-guided lung nodule type classification on CT images,” *Comput. Graphics*, vol. 70, pp. 288–299, July 2017.

[57] X. Yutong , Z. Jianpeng , X. Yong, M. Fulham and Z. Yanning, "Fusing texture, shape and deep model-learned information at decision level for automated classification of lung nodules on chest CT," *Inf. Fusion*, vol. 42, pp. 102–110, Oct. 2017.

[58] R. Paul *et al.*, "Predicting malignant nodules by fusing deep features with classical radiomics features," *SPIE J. Med. Imaging*, vol. 5, no. 1, pp. 011021-1-011021-11, Mar. 2018.

[59] I. Yoshino, M. Yamaguchi, T. Tagawa, S. Fukuyama, T.Kameyama, A. Osoegawa, and Y. Maehara, "Operative resultsof clinical stage I non-small cell lung cancer," *Lung Cancer*, vol.42, no. 2, pp. 221-225, Sep. 2003.

[60] W. Suiyuan and W. Junfeng, "Pulmonary Nodules 3D Detection on Serial CT Scans," in *IEEE 3rd Global Congr. Intell. Syst*., Nov. 2012, pp. 257-260.

[61] S. Ozekes, O. Osman and O.N. Ucan, "Nodule detection in a lung region that's segmented with using genetic cellular neural networks and 3D template matching with fuzzy rule-based thresholding," *Korean J. Radiol.*, vol. 9, no. 1, pp. 1–9, Feb. 2008.

[62] A.M. Santos, A.O.de.C. Filho, A.C. Silva, A.C.de. Paiva, R.A.Nunes and M. Gattass, "Automatic detection of small lung nodules in 3D CT data using Gaussian mixture models, Tsallis entropy and SVM," *Eng. Appl. Artif. Intel.*, vol. 36, pp. 27-39, Aug. 2014.

[63] J.J. S-Cuenca, P.G.Tahoces, M. Souto, M.J..Lado, M. R-Jardin, J. Remy and J.J.Vidal, "Application of the iris filter for automatic detection of pulmonary nodules on computed tomography images," *Comput. Biol. Med.*, vol. 39, no. 10, pp. 921-933, Aug.2009.

[64] A. Riccardi, T.S. Petkov, G. Ferri, M. Masotti and R.Campanini, "Computer-aided detection of lung nodules via 3D fast radial transform, scale-space representation, and Zernike MIP classification," *Med. Phys*., vol. 38, no. 4, pp. 1962–1971, Apr. 2011.

[65] A. Teramoto and H. Fujita, “Fast lung nodule detection in chest CT images using cylindrical nodule-enhancement filter,” *Int. J.CARS.*, vol. 8, no. 2, pp. 193–205, Jun. 2012.

[66] A. Tartar, N. Kilic and A. Akan, “Classification of pulmonary nodules by using hybrid features,” *Comput. Math. Method. M.*, pp. 1-11, Jun. 2013.

[67] S. Ozekes, and O. Osman, “Computerized lung nodule detection using 3D feature extraction and learning based algorithms,” *J.Med. Syst.*, vol. 34, pp. 185-194, Nov. 2008.

[68] S. Soltaninejad, M. Keshani and F. Tajeripour, “Lung nodule detection by KNN classifier and active contour modelling and3D visualization,” in *IEEE 16th CSI Int. Symp. Artif. Intell. Signal Process. (AISP)*, May 2012, pp. 440-445.

[69] H. M. Orozco, O. O. V. Villegas, H. d. J. O. Domínguez and V.G. C. Sánchez, “Lung Nodule Classification in CT Thorax Images Using Support Vector Machines,” in *IEEE 12th Mexican Int. Conf. Artif. Intell.*, Nov. 2013, pp. 277-283.

[70] R. Achanta, A. Shaji, K. Smith, A. Lucchi, P. Fua, and S. Susstrunk, “SLIC Superpixels Compared to State-of-the-ArtSuperpixel Methods,” *IEEE Trans. Pattern Anal. Mach. Intell.*, vol. 34, no. 11, pp. 2274-2282, Nov. 2012.

[71] V. Vapnik, “Statistical Learning Theory,” New York, USA: Wiley, 1998.

[72] E.L. Torres *et al.*, “Large scale validation of the M5L lung CAD on heterogeneous CT datasets,” *Med. Phys.*, vol. 42, no. 4, pp.1477-1489, Apr. 2015.

[73] Armato *et al.*, “Computerized Detection of Pulmonary Nodules on CT Scans,” *RadioGraphics*, vol. 19, no. 5, pp. 1303–1311, Sept.-Oct. 1999.

[74] J. Dehmeshki, H. Amin, M. Valdivieso and X. Ye, "Segmentation of Pulmonary Nodules in Thoracic CT Scans: A Region Growing Approach," *IEEE Trans. Medical Imaging*, vol. 27, no. 4, pp. 467-480, Apr. 2008.

[75] Ge *et al*., "Computer-aided detection of lung nodules: False positive reduction using a 3D gradient field method and 3Dellipsoid fitting," *Med. Phys*., vol. 32, no. 8, pp. 1477-1489, Aug. 2005.

[76] M. Gomathi and P. Thangaraj, "A Computer Aided Diagnosis System for Detection of Lung Cancer Nodules using Extreme Learning Machine," *IJEST*, vol. 2, no. 10, pp. 5770-5779, 2010.

[77] Y. Lee, T. Hara, H. Fujita, S. Itoh and T. Ishigaki, "Automated Detection of Pulmonary Nodules in Helical CT Images Based on an Improved Template-Matching Technique," *IEEE Trans. Medical Imaging*, vol. 20, no. 7, pp.595-604, July 2001.

[78] I.R.S. Valente *et al*., "Automatic 3D pulmonary nodule detection in CT images: A survey," *Comput. Methods Programs Biomed*., vol. 124, pp. 91-107, Dec. 2015.

[79] G. Litjens *et al*., "A survey on deep learning in medical image analysis," *Comput. Med. Image Anal*., vol. 42, pp. 60-88, July 2017.

[80] M. Alilou, V. Kovalev, E. Snezhko and V. Taimouri, "A Comprehensive Framework for Automatic Detection of Pulmonary Nodules in Lung CT Images," *Image Anal. Stereol*., vol. 33, no. 1, pp. 13-27 , Feb. 2014.

[81] L. Lu, Y. Tan, L. H. Schwartz and B. Zhao, "Hybrid detection of lung nodules on CT scan images," *Med. Phys*., vol. 42, no. 9, pp. 5042-5054 , Sept. 2015.

[82] B. Wang, X. Tian, Q. Wang, Y. Yang, H. Xie, S. Zhang and L. Gu, "Pulmonary nodule detection in CT images based on shape constraint CV model," *Med. Phys*., vol. 42, no. 3, pp. 1241-1254 , Mar. 2015.

[83] WHO report on cancer: setting priorities, investing wisely and providing care for all. World Health Organization. (2020). License: CC BY-NC-SA 3.0 IGO. https://apps.who.int/iris/handle/10665/330745.

[84] F. Bray *et al*., "Global Cancer Statistics 2018: GLOBOCAN Estimates of Incidence and Mortality Worldwide for 36 Cancers in 185, vol. 68, no. 6, pp. 394-424, Sept. 2018.

[85] International Agency for Research on Cancer. [Online] https://www.who.int/cancer/PRGlobocanFinal.pdf.

[86] C. Zappa and A.A. Mousa, "Non-small cell lung cancer: current treatment and future advances," *Transl. Lung Cancer Res*., vol. 5, no. 3, pp. 288-300, June 2016.

[87] B. J. McKee *et al*., "Performance of ACR Lung-RADS in a Clinical CT Lung Screening Program," *J. Am. Coll. Radiol*., vol. 12, no. 3, pp. 273-276, Feb. 2016.

[88] T. Messay, R. C. Hardie and T. R. Tuinstra, "Segmentation of pulmonary nodules in computed tomography using a regression neural network approach and its application to the Lung Image Database Consortium and Image Database Resource Initiative dataset," *Med. Image Anal*., vol. 22, pp. 48-62, Feb. 2015.

[89] V. Vasconcelos, J. Barroso, L. Marques and J. S. Silva, "Enhanced Classification of Interstitial Lung Disease Patterns in HRCT Images Using Differential Lacunarity," *BioMed Res. Int*., pp. 672520-1-9, 2015.

[90] Q. Shi, W. Desheng, C. Ying and F. Jun, "Lung Nodules Detection in CT Images Using Gestalt-Based Algorithm," *Chin. J. Electron*., vol. 25, no. 4, pp. 711–718, 2016.

[91] J. John and M. G. Mini, "Multilevel Thresholding Based Segmentation and Feature Extraction for Pulmonary Nodule Detection," *Procedia Technol*., vol. 24, pp. 957-963, July 2016.

[92] R. Manickavasagam and S. Selvan, "Automatic Detection and Classification of Lung Nodules in CT Image Using Optimized Neuro Fuzzy Classifier with Cuckoo Search Algorithm," *J. Med. Syst*., vol. 43, no. 77, Feb. 2019.

[93] J. Novo, L. Gonalves, A.M. Mendona and A. Campilho, “3D lung nodule candidate detection in multiple scales,” in *IEEE 14th Int. Conf. Mach. Vision Appl. (MVA)*, May 2015, pp. 61-64.

[94] P. B. Sangamithraa and S. Govindaraju, “Lung tumour detection and classification using EK-Mean clustering,” in *IEEE Int. Conf. Wireless Commun., Signal Process. Networking (WiSPNET)*, Mar. 2016, pp. 2201-2206.

[95] A. El Hassani, B. A. Skourt and A. Majda, “Efficient Lung CT Image Segmentation using Mathematical Morphology and the Region Growing algorithm,” in *IEEE Int. Conf. Intell. Syst. Adv. Comput. Sci. (ISACS)*, Dec. 2019, pp. 1-6.

[96] H. Chung, H. Ko, S. J. Jeon, K.-H. Yoon and J. Lee, “Automatic Lung Segmentation With Juxta-Pleural Nodule Identification Using Active Contour Model and Bayesian Approach,” *IEEE J. Transl. Eng. Health Med*., vol. 6, pp. 1-13, May 2018.

[97] M. Tan, R. Deklerck, B. Jansen, M. Bister and J. Cornelis, “A novel computer-aided lung nodule detection system for CT images,” *Med. Phys*., vol. 38, no. 10, pp. 5630-5645, Oct. 2011.

[98] A. El-Baz, A. Elnakib, M. A. El-Ghar, G. Gimel'farb, R. Falk and A. Farag, “Automatic Detection of 2D and 3D Lung Nodules in Chest Spiral CT Scans,” *Int. J. Biomed. Imaging*, pp. 517632-1-11, Feb. 2013.

[99] D. Cascio, R. Magro, F. Fauci, M. Iacomi and G. Raso, “Automatic detection of lung nodules in CT datasets based on stable 3D mass–spring models,” *Comput. Biol. Med*., vol. 42, no. 11, pp. 1098-1109, Sept. 2012.

[100] J. Ma, Z. Zhou, Y. Ren, J. Xiong, L. Fu, Q. Wang and J. Zhao, “Computerized detection of lung nodules through radiomics,” *Med. Phys*., vol. 44, no. 8, pp. 4148–4158, Aug. 2017.

[101] V. F. Kravchenko, V. I. Ponomaryov, V. I. Pustovoit and E. Rendon-Gonzalez, “Classification of Lung Nodules Using CT Images Based on Texture Features and Fractal Dimension Transformation,” Dokl. Math., vol. 99, pp. 235-239, June 2019.

[102] E. Rendon-Gonzalez and V. Ponomaryov, "Automatic Lung nodule segmentation and classification in CT images based on SVM," in *IEEE 9th Int. Kharkiv Symp. Phys. Eng. Microwaves, Millimeter and Submillimeter Waves (MSMW)*, June 2016, pp. 1-4.

[103] B. K. J. Veronica, "An effective neural network model for lung nodule detection in CT images with optimal fuzzy model," *Multimedia Tools and Applications*, vol. 79, pp. 14291–14311, Feb. 2020.

[104] S. Beucher, J. M. Blosseville and F. Lenoir, "Traffic Spatial Measurements Using Video Image Processing," in *Proc. SPIE Intell. Rob. Comput. Vision VI*, Feb. 1988, pp. 648–655.

[105] R. Lerallut, E. Decenciere and F. Meyer, "Image filtering using morphological amoebas," *Image and Vision Computing*, vol. 25, no. 4, pp. 395–404, 2006.

[106] V. Morard, E. Decenciere and P. Dokladal, "Region growing structuring elements and new operators based on their shape," in *Proc. Int. Conf. Signal Image Process.*, Dec. 2011, pp. 78–85.

[107] A. Landstrom and M. J. Thurley, "Adaptive morphology using tensor-based elliptical structuring elements," *Pattern Recognit. Lett.*, vol. 34, no. 12, pp. 1416–1422, May 2013.

[108] R. M. Haralick, K. Shanmugam and I. Dinstein, "Textural features for image classification," *IEEE Trans. Syst. Man Cybern*., vol. 3, no. 6, pp. 610–621, 1973.

[109] M. Dolejsi, J. Kybic, M. Polovincak and S. Tuma, "The lung TIME: annotated lung nodule dataset and nodule detection framework," in *Proc. SPIE Med. Imaging*, Mar. 2009, 12.811645.

[110] S. Saien, A. H. Pilevar and H. A. Moghaddam, "Refinement of lung nodule candidates based on local geometric shape analysis and Laplacian of Gaussian Kernels," *Comput. Biol. Med*., vol. 54, pp. 188–198, Sept. 2014.

[111] B. Wang, X. Tian, Q. Wang, Y. Yang, H. Xie, S. Zhang and L. Gu, “Pulmonary nodule detection in CT images based on shape constraint CV model,” *Med. Phys*., vol. 42, no. 3, pp. 1241–1254, Mar. 2015.

[112] W. Zhang, X. Wang, X. Li and J. Chen, “3D skeletonization feature based computer-aided detection system for pulmonary nodules in CT datasets,” *Comput. Biol. Med*., vol. 92, pp. 64–72, Nov. 2017.

[113] Y. Chen, E. Zitello, R. Guo and Y. Deng, “The function of LncRNAs and their role in the prediction, diagnosis, and prognosis of lung cancer,” *Clin. Transl. Med*., vol. 11, no. 4, (2021) pp. 1–21, Apr. 2021.

[114] W. D. Travis, E. Brambilla, A. Burke and A. G. Nicholson, “WHO Classification of Tumours of the Lung, Pleura,” in *Thymus and Heart*, Lyon, France: IARC Press, 2015.

[115] W. D. Travis, E. Brambilla and G. J. Riely, “New pathology classification of lung cancer: Relevance for clinical practice and clinical trials,” *J. Clin. Oncol*., vol. 31, no. 8, pp. 992–1001, Mar. 2013.

[116] K. Simonyan and A. Zisserman, “Very deep convolutional networks for large-scale image recognition,” 2014, arXiv:1409.1556v6.

[117] A. Krizhevsky, I. Sutskever and G. E. Hinton, “ImageNet classification with deep convolutional neural networks,” *Commun. ACM*, vol. 60, no. 6, pp. 84–90, June 2017.

[118] Y. Lecun, L. Bottou, Y. Bengio and P. Haffner, “Gradient-based learning applied to document recognition,” *Proc. IEEE*, vol. 86, no.11, pp. 2278–2324, Nov. 1998.

[119] K. He, X. Zhang, S. Ren and J. Sun, “Deep residual learning for image recognition,” in *IEEE/CVF Conf. Comput. Vision Pattern Recognit. (CVPR)*, 2016, pp. 770–778.

[120] X. Huang, Q. Lei, T. Xie, Y. Zhang, Z. Hu and Q. Zhou, “Deep Transfer Convolutional Neural Network and Extreme Learning Machine for lung nodule diagnosis on CT images,” *Knowl.-Based Syst*., vol. 204 ,106230, July 2020.

[121] Y. Liu, P. Hao, P. Zhang, X. Xu, J. Wu and W. Chen, “Dense Convolutional Binary-Tree Networks for Lung Nodule Classification,” *IEEE Access*, vol. 6, pp. 49080–49088, 2018.

[122] H. Liu, H. Cao, E. Song, G. Ma, X. Xu, R. Jin, C. Liu and C-C Hung, “Multi-model Ensemble Learning Architecture Based on 3D CNN for Lung Nodule Malignancy Suspiciousness Classification,” *J. Digit. Imaging*, vol. 33, pp. 1242–1256, June 2020.

[123] P. Sahu, D. Yu, M. Dasari, F. Hou and H. Qin, “A Lightweight Multi-section CNN for Lung Nodule Classification and Malignancy Estimation,” *IEEE J. Biomed. Health. Inf.*, vol. 23, no. 3, pp. 960–968, Nov. 2019.

[124] Y. Xie, J. Zhang and Y. Xia, “Semi-supervised adversarial model for benign–malignant lung nodule classification on chest CT,” *Med. Image Anal*., vol. 57, pp. 237–248, July 2019.

[125] S. Shen, S. X. Han, D. R. Aberle, A. A. Bui and W. Hsu, “An interpretable deep hierarchical semantic convolutional neural network for lung nodule malignancy classification,” *Expert Syst. Appl*., vol. 128, pp. 84–95, Jan. 2019.

[126] F. Yu and V. Koltun, “Multi-scale context aggregation by dilated convolutions,” 2015, arXiv:1511.07122.

[127] S. Mehta M. Rastegari, A. Caspi, L. Shapiro and H. Hajishirzi, “ESPNet: Efficient Spatial Pyramid of Dilated Convolutions for Semantic Segmentation,” 2018, arXiv: 1803.06815.

[128] R. Hamaguchi, A. Fujita, K. Nemoto, T. Imaizumi and S. Hikosaka, “Effective Use of Dilated Convolutions for Segmenting Small Object Instances in Remote Sensing Imagery,” 2017, arXiv:1709.00179.

[129] X. Lei, H. Pan and X. Huang, “A dilated CNN model for image classification,” *IEEE Access*, vol. 7, pp. 124087–124095, July 2019.

[130] A. B. Abdul Qayyum, T. Islam and M. A. Haque, "Malaria Diagnosis with Dilated Convolutional Neural Network Based Image Analysis," in *IEEE Int. Conf. Biomed. Eng., Comput. Inf. Technol. Health (BECITHCON)*, Nov. 2019, pp. 68–72.

[131] M. Ward, C.-H. Min, H. Salamy and K. Nepal, "Dilated Temporal Convolutional Neural Network Architecture with Independent Component Layer for Human Activity Recognition," in *IEEE 26th Int. Conf. Electronics, Circuits Syst. (ICECS)*, Nov. 2019, pp. 49–52.

[132] L. Zhang and W. Zuo, "Image Restoration: From Sparse and Low-Rank Priors to Deep Priors," *IEEE Signal Process Mag*., vol. 34, no. 5, pp. 172–179, Sept. 2017.

[133] A. Bozorgpour, R. Azad, E. Showkatian and A. Sulaiman, "Multi-scale Regional Attention Deeplab3+: Multiple Myeloma Plasma Cells Segmentation in Microscopic Images," 2021, arXiv:2105.06238.

[134] Q. Zhang, Q. Yuan, J. Li, Z. Yang and X. Ma, "Learning a Dilated Residual Network for SAR Image Despeckling," *Remote Sens*., vol. 10, no. 2, 196, Jan. 2018.

[135] A. Hasegawa, S.-C.Benedict Lo, M.T. Freedman and S.K. Mun, "Convolution neural-network-based detection of lung structures," in *Proc. SPIE Med. Imaging*, May 1994, pp 654–662.

[136] J.S. Lin *et al*., "An application of convolution neural networks: reducing false-positives in lung nodule detection," in *Proc. IEEE 1994 Nucl. Sci. Symp.- NSS'94*, Oct.-Nov. 1994, vol. 4, pp 1842–1846.

[137] S.-C.B. Lo, S-L..A. Lou, J.S. Lin, M.T. Freedman, M.V. Chien and S.K. Mun, "Artificial convolution neural network techniques and applications for lung nodule detection," *IEEE Trans. Med. Imaging*, vol. 14, no. 4, pp. 711–718, Dec. 1995.

[138] Y. Li, X. Zhang and D. Chen, "CSRNet: Dilated convolutional neural networks for understanding the highly congested scenes," 2018, arXiv:1802.10062.

[139] L.C. Chen, Y. Zhu, G. Papandreou, F. Schroff and H. Adam, "Encoder-Decoder with Atrous Separable Convolution for Semantic Image Segmentation," in *Springer Eur. Conf. Comput. Vision (ECCV)*, Oct. 2018, pp. 833–851.

[140] J. Long, E. Shelhamer and T. Darrell, "Fully convolutional networks for semantic segmentation," 2015, arXiv:1411.4038.

[141] O. Ronneberger, P. Fischer and T. Brox, "U-Net: Convolutional Networks for Biomedical Image Segmentation," in *Int. Conf. Med. Image Comput. Comput. Assisted Intervention (MICCAI)*, 2015, pp. 234–241. arXiv.1505.04597.

[142] V. Badrinarayanan, A. Kendall and R. Cipolla, "Segnet: A deep convolutional encoder-decoder architecture for image segmentation," *IEEE Trans. Pattern Anal. Mach. Intell*, vol. 39, no. 12, pp. 2481–2495, Jan. 2017.

[143] G. Lin, A. Milan, C. Shen and I. Reid, "Refinenet: Multi-path refinement networks for high-resolution semantic Segmentation," in *IEEE/CVF Conf. Comput. Vision Pattern Recognit. (CVPR)*, 2017, pp. 1925–1934. arXiv.1611.06612.

[144] L.-C. Chen, G. Papandreou, I. Kokkinos, K. Murphy and A L. Yuille, "Semantic Image Segmentation with Deep Convolutional nets and Fully Connected CRFs," in *Int Conf. Learn. Representations (ICLR)*, 2015, arXiv.1412.7062.

[145] L.-C. Chen, G. Papandreou, I. Kokkinos, K. Murphy and A L. Yuille, "DeepLab: Semantic Image Segmentation with Deep Convolutional Nets, Atrous Convolution, and Fully Connected CRFs," *IEEE Trans. Pattern Anal. Mach. Intell*, vol. 40, no. 4, pp. 834–848, Apr. 2018.

[146] L.-C Chen, G. Papandreou, F. Schroff and H. Adam, "Rethinking Atrous Convolution for Semantic Image Segmentation," 2017, arXiv.1706.05587.

[147] R. Roy, T. Chakraborti and A.S. Chowdhury, "A deep learning-shape driven level set synergism for pulmonary nodule segmentation," *Pattern Recognit. Lett.*, vol. 123, pp. 31–38, Mar. 2019.

[148] M. Usman *et al*., "Volumetric lung nodule segmentation using adaptive ROI with multi-view residual learning," *Sci. Rep*., vol. 10, 12839, July 2020.

[149] Z. Shi *et al*., "Automatic Nodule Segmentation Method for CT Images Using Aggregation-U-Net Generative Adversarial Networks," *Sens. Imaging*, vol. 21, no. 39, pp. 1–16, July 2020.

[150] Z. Xiao, B. Liu, L. Geng, F. Zhang and Y. Liu, "Segmentation of Lung Nodules Using Improved 3D-UNet Neural Network," *Symmetry*, vol. 12, no. 11, 1787, Oct. 2020.

[151] S. Jain, S. Indora and D. K. Atal, "Lung nodule segmentation using Salp Shuffled Shepherd Optimization Algorithm-based Generative Adversarial Network," *Comput. Biol. Med*., vol. 137, 104811, Aug. 2021.

[152] S. Tyagi and S N. Talbar, "CSE-GAN: A 3D conditional generative adversarial network with concurrent squeeze-and-excitation blocks for lung nodule segmentation," *Comput. Biol. Med*., vol. 147, 105781, June 2022.

[153] D. Lu, J. Chu, R. Zhao, Y. Zhang and G. Tian, "A Novel Deep Learning Network and Its Application for Pulmonary Nodule Segmentation," *Comput. Intell. Neurosci*., vol. 20, no. 10, 7124902, May 2022.

[154] Y. Xie, J. Zhang and Y. Xia, "Semi-supervised adversarial model for benign–malignant lung nodule classification on chest CT," *Med. Image Anal*., vol. 57, pp. 237–248, July 2019.

[155] Y. Zhang, J. Zhang, L. Zhao, X. Wei and Q. Zhang, "Classification of Benign and Malignant Pulmonary Nodules Based on Deep Learning," in *IEEE 5th Int. Conf. Inf. Sci. Control Eng. (ICISCE)*, Jul 2018, pp. 156–160.

[156] Shaffie *et al*., "A Generalized Deep Learning-Based Diagnostic System for Early Diagnosis of Various Types of Pulmonary Nodules," *Technol. Cancer Res*. *Treat*., vol. 17 Sept. 2018.

[157] Suresh and Mohan, "ROI-based feature learning for efficient true positive prediction using convolutional neural network for lung cancer diagnosis," *Neural Comput. & Applic*., vol. 32, pp. 15989–16009, Mar. 2020.

[158] J. Lyu, X. Bi and S. H. Ling, "Multi-Level Cross Residual Network for Lung Nodule Classification," *Sensors*, vol. 20, no. 10, 2837, May 2020.

[159] H. Sung *et al*., "Global Cancer Statistics 2020: GLOBOCAN Estimates of Incidence and Mortality Worldwide for 36 Cancers in 185 Countries, " *CA: A Cancer J. Clinicians*, vol. 71, no. 3, pp. 209–249, Feb. 2021.

[160] National Cancer Registry Programme. https://www.ncdirindia.org/ncrp /ca/index.aspx, Accessed 05 Mar. 2023.

[161] P. Mathur *et al*., "ICMR-NCDIR-NCRP Investigator Group. Cancer Statistics, 2020: Report From National Cancer Registry Programme," *JCO Glob Oncol.,* India, pp. 1063-1075, July 2020.

[162] S. Chen, J. Qin, X. Ji, B. Lei, T. Wang, D. Ni and J. Z. Cheng, "Automatic Scoring of Multiple Semantic Attributes with Multi-task Feature Leverage: A Study on Pulmonary Nodules in CT Images," *IEEE Trans. Med. Imaging*, vol. 36, no. 3, pp. 802–814, Nov. 2016.

[163] F. Han *et al*., "Texture Feature Analysis for Computer-Aided Diagnosis on Pulmonary Nodules," *J. Digit Imaging*, vol. 28, no. 1, pp. 99–115, Feb. 2015.

[164] A. K. Dhara, S. Mukhopadhyay, A. Dutta, M. Garg and N. Khandelwal, "A Combination of Shape and Texture Features for Classification of Pulmonary Nodules in Lung CT Images," *J. Digit. Imaging*, vol. 29, no. 4, pp. 466–475, Aug. 2016.

[165] L. Sorensen, S. B. Shaker and M. D. Bruijne, "Quantitative Analysis of Pulmonary Emphysema Using Local Binary Patterns," *IEEE Trans. Med. Imaging*, vol. 29, no. 2, pp. 559–569, Feb. 2010.

[166] C. Szegedy *et al*., "Going deeper with convolutions," in Proc. CVPR, 2015, pp. 1–9.

[167] A. Nibali, Z. He and D. Wollersheim, "Pulmonary nodule classification with deep residual networks," *Int. J. CARS*., vol. 12, no. 10, pp. 1799–1808, Oct. 2017.

[168] N. Nasrullah *et al*., "Automated Lung Nodule Detection and Classification Using Deep Learning Combined with Multiple Strategies," *Sensors*, vol. 19, no. 17, 3722, Aug. 2019.

[169] Y. Xie, Y. Xia, J. Zhang, Y. Song, D. Feng, M. Fulham and W. Cai, "Knowledge-based Collaborative Deep Learning for Benign-Malignant Lung Nodule Classification on Chest CT," *IEEE Trans. Med. Imaging*, vol. 38, no. 4, pp. 991–1004, Oct. 2018.

[170] G.L. F. da Silva *et al*., "Lung nodules diagnosis based on evolutionary convolutional neural network," *Multimed. Tools Appl*., vol. 76, pp. 19039–19055, Mar. 2017.

[171] M. A. Shabi, B. L. Lan, W. Y. Chan, K. H. Ng and M. Tan, "Lung nodule classification using deep Local-Global networks," *Int. J. CARS*., vol. 14, no. 10, pp. 1815–1819, Apr. 2019.

[172] R. Paul, M. Schabath, R. Gillies, L. Hall and D. Goldgof, "Convolutional Neural Network ensembles for accurate lung nodule malignancy prediction 2 years in the future," *Comput. Biol. Med*., vol. 122, 103882, June 2020.

[173] J. Masci, J. Angulo and J. Schmidhuber, "A Learning Framework for Morphological Operators using Counter-Harmonic Mean," in *Springer Int. Symp. Math. Morphol. Appl. Signal Image Process. (ISMM)*, 2013, pp. 329–340.

[174] D. Mellouli, T. M. Hamdani, J. J. Sanchez-Medina, M. B. Ayed and A. M. Alimi, "Morphological Convolutional Neural Network Architecture for Digit Recognition," *IEEE Trans. Neural Networks Learn. Syst*., vol. 30, no.9, pp. 2876–2885, Jan. 2019.

[175] K. Nogueira *et al*., "An Introduction to Deep Morphological Networks, 2019, arXiv: 1906.01751.

[176] J. Xie, Y. Jiang and H. Tsui, "Segmentation of kidney from ultrasound images based on texture and shape priors," *IEEE Trans. Med. Imaging*, vol. 24, no. 1, pp. 45–57, Jan. 2005.

[177] A. K. Jain and F. Farrokhnia, "Unsupervised texture segmentation using Gabor filters," *Pattern Recognit*., vol. 24, no. 12, pp. 1167–1186, May 2003.

[178] R. L. de Valois, D. G. Albrecht and L.G. Thorell, "Spatial frequency selectivity of cells in macaque visual cortex," *Vision Res*., vol. 22, no. 5, pp. 545–559, Mar. 2003.

[179] M. Stone, "Cross-Validatory Choice and Assessment of Statistical Predictions," *J. Royal Stat. Soc*., vol. 36, no. 2, pp. 111–147, 1974.

[180] W. Shen *et al*., "Multi-crop Convolutional Neural Networks for lung nodule malignancy suspiciousness classification," *Pattern Recognit*., vol. 61, pp. 663–673, May 2016.

[181] A. O. de Carvalho Filho, A. C. Silva, A. C. de Paiva, R. A. Nunes and M. Gattass, "Classification of patterns of benignity and malignancy based on CT using topology-based phylogenetic diversity index and convolutional neural network," *Pattern Recognit*., vol. 81, pp. 200–212, Apr. 2018.

[182] H. Jiang, F. Gao, X. Xu, F. Huang and S. Zhu, "Attentive and ensemble 3D dual path networks for pulmonary nodules classification," *Neurocomputing*, vol. 398, pp. 422–430, July 2019.

[183] X. Zhao, L. Liu, S. Qi, Y. Teng, J. Li and W. Qian, "Agile convolutional neural network for pulmonary nodule classification using CT images," *Int. J. CARS*., vol. 13, no. 4, pp. 585–595, Feb. 2018.

[184] P. Lin, Q. Lu, D. Li, Y. Chen, Z. Zou and S. Jiang, "Artificial intelligence classification of wetland vegetation morphology based on deep convolutional neural network," *Nat. Resour. Model*., vol. 33, no. 1, pp. 1–17, Feb. 2020.

[185] J. Ferlay *et al*. Global Cancer Observatory: Cancer Today. Lyon, France: International Agency for Research on Cancer. [Online] https://gco.iarc.fr/today. Accessed Mar. 11, 2023.

[186] S. B. Knight, P. A. Crosbie, H. Balata, J. Chudziak, T. Hussell and C. Dive, " Progress and prospects of early detection in lung cancer," *Open Biol.*, vol. 7, no. 9, 170070, Sept. 2017.

[187] M. Veta, A. Huisman, M. A. Viergever, P. J. van Diest and J. P. W. Pluim, "Marker-controlled watershed segmentation of nuclei in H&E stained breast cancer biopsy images," in *IEEE Int. Symp. Biomed. Imaging: From Nano to Macro*, Mar.-Apr. 2011, pp. 618–621.

[188] R. Kumar, R. Srivastava and S. Srivastava, "Detection and Classification of Cancer from Microscopic Biopsy Images Using Clinically Significant and Biologically Interpretable Features," *J. Med. Eng*., 457906, Aug. 2015.

[189] A. Albayrak and G. Bilgin, "Automatic cell segmentation in histopathological images via two-staged superpixel-based algorithms," *Med. Biol. Eng. Comput*., vol. 57, pp. 653–665, Oct. 2018.

[190] M. Li *et al*., "Research on the Auxiliary Classification and Diagnosis of Lung Cancer Subtypes Based on Histopathological Images," *IEEE Access*, vol. 9, pp. 53687–53707, Apr. 2021.

[191] C.-W. Wang and C.-P. Yu, "Automated morphological classification of lung cancer subtypes using H&E tissue images," *Mach. Vision Appl*., vol. 24, pp. 1383–1391, Oct. 2012.

[192] K-H. Yu *et al*., "Predicting non-small cell lung cancer prognosis by fully automated microscopic pathology image features," *Nat. Commun*., vol. 7, 12474, Aug. 2016.

[193] M. Nishio, M. Nishio, N. Jimbo and K. Nakane, "Homology-Based Image Processing for Automatic Classification of Histopathological Images of Lung Tissue," *Cancers*, vol. 13, no. 6, 1192, Mar. 2021.

[194] F. Pourakpour and H. Ghassemian, "Automated mitosis detection based on combination of effective textural and morphological features from breast cancer histology slide images," in *IEEE 22nd Iran. Conf. Biomed. Eng. (ICBME)*, Nov. 2015, pp. 269–274.

[195] Y. Zhang, B. Zhang and W. Lu, "Breast Cancer Histological Image Classification with Multiple Features and Random Subspace Classifier Ensemble," in *Knowledge-Based Systems in Biomedicine and Computational Life Science*, Berlin, Heidelberg: Springer, vol. 450, pp. 27–42.

[196] C. Loukas, S. Kostopoulos, A. Tanoglidi, D. Glotsos, C. Sfikas and D. Cavouras, "Breast Cancer Characterization Based on Image Classification of Tissue Sections Visualized under Low Magnification," *Comput. Math. Methods Med.*, 829461, Aug. 2013.

[197] Anuranjeeta, K. K. Shukla, A.Tiwari and S. Sharma, "Classification of Histopathological Images of Breast Cancerous and Non Cancerous Cells based on Morphological Features," *Biomed. Pharmacol. J.*, vol. 10, no.1, pp. 353–366, Jan. 2017.

[198] D. Albashish, S. Sahran, A. Abdullah, A. Adam and M. Alweshah, "A Hierarchical Classifier for Multiclass Prostate Histopathology Image Gleason Grading," *J. Inf. Commun. Technol.*, vol. 17, no. 2, pp. 323–346, Apr. 2018.

[199] C. Wang, W. Gong, J. Cheng and Y. Qian, "DBLCNN: Dependency-based lightweight convolutional neural network for multi-classification of breast histopathology images," *Biomed. Signal Process. Control*, vol. 73, 103451, Dec. 2021.

[200] Y. Zou, S. Chen, C. Che, J. Zhang and Q. Zhang, "Breast cancer histopathology image classification based on dual-streamhigh-order network," *Biomed. Signal Process. Control*, vol. 78, 104007, July 2022.

[201] K. Roy, D. Banik, D. Bhattacharjee and M. Nasipuri, "Patch-based system for Classification of Breast Histology Images using deep learning," *Comput. Med. Imaging Graphics. Control*, vol. 71, pp. 90–103, Dec. 2018.

[202] Qaiser *et al*., “Fast and accurate tumor segmentation of histology images using persistent homology and deep convolutional features,” *Med. Image Anal*., vol. 55, pp. 1–14, Apr. 2019.

[203] J.W. Wei *et al*., “Pathologist-level classification of histologic patterns on resected lung adenocarcinoma slides with deep neural networks,” *Sci. Rep*., vol. 9, 3358, Mar. 2019.

[204] H. Tokunaga, Y. Teramoto, A. Yoshizawa and R. Bise, “Adaptive Weighting Multi-Field-of-View CNN for Semantic Segmentation in Pathology,” in *IEEE/CVF Conf. Comput. Vision Pattern Recognit. (CVPR)*, 2019, pp. 12589–12598.

[205] L. Cong, W. Feng, Z. Yao, X. Zhou and W. Xiao, “Deep Learning Model as a New Trend in Computer-aided Diagnosis of Tumor Pathology for Lung Cancer,” *J. Cancer*, vol. 11, no. 12, pp. 3615–33622, Mar. 2020.

[206] S. K. Jafarbiglo, H. Danyali and M. S. Helfroush, “Nuclear Atypia Grading in Histopathological Images of Breast Cancer Using Convolutional Neural Networks,” in *IEEE 4th Iran. Conf. Signal Process. Intell. Syst. (ICSPIS)*, Dec. 2018, pp. 89–93.

[207] N. Sengar, N. Mishra, M. K. Dutta, J. Prinosil and R. Burget, “Grading of colorectal cancer using histology images,” in *IEEE 39th Int. Conf. Telecommun. Signal Process. (TSP)*, June 2016, pp. 529–532.

[208] M. K. K. Niazi *et al*., “Visually Meaningful Histopathological Features for Automatic Grading of Prostate Cancer,” *J. Biomed. Health. Inf*., vol. 21, no. 4, pp. 1027–1038, May 2016.

[209] D. R. Nayak, N. Padhy and B. K. Swain, “Blood cell image segmentation using modified fuzzy divergence with morphological transforms,” *Mater. Today: Proc*., vol. 37, pp. 2708–2718, Sept. 2020.

[210] K. Mardani and K. Maghooli, “Enhancing retinal blood vessel segmentation in medical images using combined segmentation modes extracted by DBSCAN and morphological reconstruction,” *Biomed. Signal Process. Control*, vol. 69, 102837, June 2021.

[211] A. Touil, K. Kalti, P.-H.Conze, B. Solaiman and M.A. Mahjoub, “Automatic detection of micro calcification based on morphological operations and structural similarity indices,” *Biocybern. Biomed. Eng*., vol. 40, no. 3, pp. 1155–1173, June 2020.

[212] S. Chatterjee, D. Dey and S. Munshi, “Integration of morphological preprocessing and fractal based feature extraction with recursive feature elimination for skin lesion types classification,” *Comput. Methods Programs Biomed*., vol. 178, pp. 201–218, June 2019.

[213] J. N. Hasoon *et al*., “COVID-19 anomaly detection and classification method based on supervised machine learning of chest X-ray images,” *Results Phys*., vol. 31, 105045, Nov. 2021.

[214] A. Halder, S. Chatterjee, D. Dey, S. Kole and S. Munshi, “An adaptive morphology based segmentation technique for lung nodule detection in thoracic CT image,” *Comput. Methods Programs Biomed*., vol. 197 105720, Aug. 2020.

[215] A.A. Borkowski, M.M. Bui, L.B. Thomas, C.P. Wilson, L.A. DeL and, S.M. Mastorides, “Lung and Colon Cancer Histopathological Image Dataset (LC25000),” pp. 1–2, 2019, arXiv:1912.12142.

[216] K. Simonyan and A. Zisserman, “Very deep convolutional networks for large-scale image recognition,” 2014. arXiv.1409.1556.

[217] S. P. Dakua and J. S. Sahambi, “Automatic Left Ventricular Contour Extraction from Cardiac Magnetic Resonance Images Using Cantilever Beam and Random Walk Approach,” *Cardiovasc. Eng*., vol. 10, no. 1, pp. 30–43, Jan. 2010.

[218] S. P. Dakua and J. S. Sahambi, “LV Contour Extraction from Cardiac MR Images Using Random Walks Approach,” in *IEEE Int. Adv. Comput. Conf*., Mar. 2009, pp. 228–233.

[219] S. P. Dakua and J. S. Sahambi, “Modified active contour model and Random Walk approach for left ventricular cardiac MR image segmentation,” *Int. J. Numer. Meth. Biomed. Engng*., vol. 27, pp. 1350–1361, Feb. 2011.

[220] S. P. Dakua, J. Abinahed and A. Al.-Ansari, "A PCA-based approach for brain aneurysm segmentation," *Multidimension. Syst. Signal Process.*, vol. 29, pp. 257–277, Nov. 2016.

[221] S. P. Dakua, J. Abinahed and A.A.Al.-Ansari, "Pathological liver segmentation using stochastic resonance and cellular automata," *J. Visual Commun. Image Represent.*, vol. 34, pp. 89–102, Jan. 2016.

[222] N. Lee, A.F. Laine, G. Mrquez, J.M. Levsky and J.K. Gohagan, "Potential of computer-aided diagnosis to improve CT lung cancer screening," *IEEE Rev. Biomed. Eng.*, vol. 2, pp. 136–146, Oct. 2009.

[223] B. K. Hatuwal and H. C. Thapa, "Lung Cancer Detection Using Convolutional Neural Network on Histopathological Images," *IJCTT*, vol. 68, no. 10, pp. 21–24, Jan. 2020.

[224] S. Mangal, A. Chaurasia and A. Khajanchi, "Convolution Neural Networks for diagnosing colon and lung cancer histopathological images," 2020, arXiv:2009.03878.

[225] A.-ur.-Rahman, K. Sultan, I. Naseer, R. Majeed, D. Musleh, M. A. Gollapalli, S. Chabani, N. Ibrahim, S. Y. Siddiqui and M. A. Khan, "Supervised Machine Learning-based Prediction of COVID-19," *Comput. Materials & Continua.*, vol. 69, no. 1, pp. 21–34, June 2021.

Never stop learning!